High-Resolution Reflection Microscopy via Absorbance Modulation

Dissertation

for the award of the degree

„Doctor rerum naturalium“(Dr.rer.nat)

of the Georg-August-Universität Göttingen

within the doctoral program physics

of the Georg-August University School of Science (GAUSS)

submitted by

Parul Jain

from Ajmer, Rajasthan, India

Göttingen, September 2022

Thesis Committee

apl. Prof. Dr. Alexander Egner
Optische Nanoskopie
Institut für Nanophotonik Göttingen e.V.

Prof. Dr. Claus Ropers
Max-Planck-Institut für Multidisziplinäre Naturwissenschaften
& Georg-August-Universität Göttingen

Prof. Dr.-Ing. Christian Rembe
Institut für Elektrische Informationstechnik
TU Clausthal

Members of the Examination Board:

First Reviewer:	**apl. Prof. Dr. Alexander Egner**
Second Reviewer:	**Prof. Dr. Jörg Enderlein**
	III. Physikalisches Institut
	Georg-August-Universität Göttingen

Further Members of the Examination Board:

Prof. Dr. Claus Ropers
Max-Planck-Institut für Multidisziplinäre Naturwissenschaften
& Georg-August-Universität Göttingen

Prof. Dr.-Ing. Christian Rembe
Institut für Elektrische Informationstechnik
TU Clausthal

Prof. Dr. Sarah Köster
Institut für Röntgenphysik
Georg-August-Universität Göttingen

apl. Prof. Dr. Michael Seibt
IV. Physikalisches Institut
Georg-August-Universität Göttingen

Date of the oral examination: 8 November 2022

Abstract

The properties of composite materials are primarily governed by their microstructural features, which can vary in size from a few nanometres to several micrometres. Optical microscopy is one of the primary tools for morphological characterisation in material science. However, due to the wave nature of light, the resolution of optical microscopes is limited by the diffraction limit [1], thereby limiting its capability to analyse these materials. Stimulated emission depletion (STED) microscopy, which is so far mostly used in life science imaging, circumvents the diffraction limit by exploiting the optical transitions of the fluorescent markers [2]. The concept of STED has been successfully applied in optical lithography (AMOL) and transmission microscopy as a technique called absorbance modulation imaging (AMI) [3, 4], where, instead of utilising the optical transitions of fluorophores, a layer of photochromic molecules, so called the absorbance modulation layer (AML), is used to achieve high resolution. The transparency of the AML, coated on the measurement surface, is rendered opaque and transparent when illuminated with light of different wavelengths. Using this wavelength-selective switching, a near-field aperture is generated in the AML to confine the light to the nanoscale dimension, resulting in sub-diffraction resolution. Despite the potential of reflection microscopy to analyse a much wider range of materials, AMI in reflection microscopy has not yet been demonstrated. Recently, Kowarsch *et al.* published a theoretical model on AMI in confocal reflection microscopy, predicting imaging beyond the diffraction limit is indeed possible [5].

In this thesis, for the first time, we experimentally validate this prediction by demonstrating one-dimensional AMI in reflection microscopy. A 2.4-fold resolution enhancement is achieved by this technique. The resolution is measured by imaging AML-coated gold nanoparticles. We further show the applicability of this technique on extended objects, an edge and a one-dimensional grating structure. The one-dimensional AMI that we demonstrate here can be extended to two dimensions which would facilitate high resolution optical imaging of microstructural features, in reflection.

Abbreviations

1D	one-dimensional
2D	two-dimensional
1D-PP	$0 - \pi$ Phase Plate
AML	Absorbance Modulation Layer
AMI	Absorbance Modulation Imaging
AMOL	Absorbance Modulation Optical Lithography
Amp-PD	Amplified Photo Diode
APSF	Amplitude Point Spread Function
BF	Bright-Field
BTE-1	1,2-bis(5,5'-dimethyl-2,2'-bithiophenyl) perfluorocyclopent-1-ene
EM	Electromagnetic
FOV	Field-of-View
FWHM	Full Width at Half Maximum
He-Ne	Helium-Neon
HWP	Half Wave Plate
IPSF	Intensity Point Spread Function
LSI	Linear Shift Invariant
NIDAQ	National Instrument Data Acquisition
PLL	Poly-L-Lysine
PMMA	Polymethylmethacrylate
PMT	Photomultiplier Tube
PSF	Point Spread Function
QWP	Quarter Wave Plate
RESOLFT	Reversible Saturable Optical Fluorescence
SO	Schwarzschild Objective
SPM	Scanning Probe Microscopy
STED	Stimulated Emission Depletion
TiSa	Titanium- Sapphire
THG	Third Harmonic Generator
UV	Ultraviolet
VDT	Vectorial Diffraction Theory
VIS	Visible
VPP	Vortex Phase Plate
WF	Wide-Field

Contents

List of Figures

Chapter 1
Introduction

Motivation

It is undeniable that the modern world is empowered by the use of materials in its technology. We are surrounded by engineered materials, from bulk materials like window glass to surface bound composite materials like semiconductor chips in our mobiles and computers. With the advancement in science and (nano)technology, demand for materials such as nanomaterials for the development of powerful computers, and composite materials to achieve high strength but light weighted, have escalated. The properties of these materials are governed by their microstructural features including the chemical composition, crystallographic arrangement and morphology of the features. Therefore, for the development of new materials or improvement of the existing materials, understanding and gaining insight into microstructural features is crucial.

Microscopy tools are central to material characterisation, especially for morphological and structural analysis. Historically, reflected light microscope was used for examining the microstructural features of materials, such as grain size, precipitate size and defects. However, the resolution of an optical microscope is fundamentally limited by diffraction, which limits its resolution and capability to image in the nanoscale regime. Therefore, more complex methods like scanning electron microscopy, and transmission electron microscopy, have to be utilised. Although these techniques provide resolution down to a nanometer, they are quite expensive and require special sample preparations and expertise in using these imaging systems. Additionally, the high magnification and small field-of-view (FOV) provided by these imaging modalities, increase the image acquisition time significantly.

The motivation behind the work presented in this thesis is to enable a far-field optical microscope for investigations on surfaces of composite materials with high-resolution.

Optical Microscopy: Beyond the Diffraction Limit

The wave nature of light fundamentally limits the ability of a lens to focus a light beam down to an infinitesimally small point. This means that if we use the best

available lens to focus the light beam, the focus will be a finite intensity distribution, the so-called PSF. In simple terms, one can think of the PSF as analogous to a "paintbrush". As the size of a paintbrush limits the fineness of the structure in a painting, imaging with a finite-sized PSF limits the resolving power of an imaging system. Therefore, to improve the resolution, the size of the PSF must be reduced as much as possible.

In 1873, Ernst Karl Abbe, the famous German microscopist and optics theoretician of the 19^{th} century, published his wave theory of microscopic imaging and defined the resolution limit of an optical microscope as [1]:

$$d_{min} = \frac{\lambda_0}{2nsin(\theta)}$$

where, d_{min} is the minimum resolvable distance between structures, λ_0 is the wavelength in vacuum and $nsin(\theta)$ defines the numerical aperture (NA) of the objective lens, where θ is the half angle of the light cone accepted by the objective and n is the refractive index of the medium in which the sample is placed. A conventional wide-field (WF) microscope typically has a lateral resolution of 250 nm (λ_0 = 500 nm and NA = 1). A straightforward way to surpass this resolution limit is to reduce the illumination wavelength or introduce an immersion medium to increase the refractive index and thus, the NA.

In deep ultraviolet microscopy [6], an illumination wavelength of 193 nm is typically used, which significantly improves the resolution. In addition to the wavelength reduction, solid immersion lenses (SIL) are also employed in these imaging systems to achieve high NA by increasing the refractive index in front of the sample. Thus, a resolution down to 100 nm can be obtained.

Another way, perhaps the oldest way to overcome the diffraction limit in optical microscopy is the near field scanning optical microscopy. It belongs to a much broader instrumental classification referred to as Scanning Probe Microscopes (SPM). In general, these techniques access the evanescent waves that are present in the so called near field zone, to achieve high-resolution. However, due to the exponentially decaying nature of the near fields, a near-field probe (an optical fiber with a sub-wavelength aperture or a cantilever with a sharp metal tip) has to be used in close proximity to the specimen. Therefore, SPMs require a feedback system to precisely control the physical separation of the probe and specimen. A resolution down to 25 nm is achievable using SPMs, however, the requirement to work in close proximity introduces various challenges in the technique [7, 8].

Over the past few decades, there has been a significant amount of improvement in the image quality and the achievable resolution of far-field optical microscopes. However, the first method that fundamentally superseded the resolution limit is

STimulated Emission Depletion (STED) microscopy [2]. STED microscopy exploits the molecular transitions of the fluorescent markers, that are generally employed as contrast agents in fluorescence microscopy, to reversibly switch them between a bright (ON) and dark state (OFF) in a controlled manner. This technique was proposed by Hell and Wichmann in 1994 and was experimentally demonstrated by Klar and Hell in 1999. In a STED microscope, two lasers, an excitation laser, to excite the fluorescent markers, and a depletion laser to switch these markers to a dark state, are employed. The depletion beam is phase modulated such that a doughnut-shaped PSF, featuring a zero-intensity centre, is generated in the focus of the objective lens. This doughnut-shaped PSF is superimposed with a Gaussian excitation PSF. When focused onto the sample, the excited fluorophores are switched to a dark state everywhere except in the zero-intensity centre of the doughnut. Therefore, fluorescence can only be emitted from a small region of the sample which effectively reduces the size of the excitation PSF (fine paintbrush!), consequently, improving the resolution. Since, the zero-intensity centre of the doughnut PSF is not diffraction-limited, this technique can theoretically achieve infinite resolution.

Considering the material structures, where the fluorescent markers cannot be used, the STED concept cannot be directly applied in material characterisation. However, the principle governing high resolution in STED microscopy is not limited to fluorescent markers. In 2006, Menon and Smith published a new concept, referred to as absorbance modulation, in which they utilised the optically reversible switchable transitions of photochromic molecules to achieve high resolution. Photochromic molecules have the ability to switch between two isomeric states with distinct absorption spectra, when exposed to the light of a suitable wavelength. In absorbance modulation, the sample under investigation is coated with a thin layer of photochromic molecules (AML). Using the STED concept, a doughnut-shaped PSF and a Gaussian PSF are focused on the sample, such that the layer is rendered opaque around the zero-intensity centre of the doughnut, thereby generating a narrow sub-wavelength aperture in the AML. This channel effectively compresses the illumination PSF down to nanometric size and thus, sub-diffraction resolution can be achieved. Absorbance modulation was successfully implemented in the field of lithography as Absorption Modulation Optical Lithography (AMOL) [3, 10] and structures with a linewidth of 36 nm were generated [11]. Imaging of structures spaced by distances as small as $\approx$ 40 nm has also been presented by using Absorbance Modulation Imaging (AMI) in transmission microscopy [4, 12].

In material characterisation, mostly reflection mode of imaging is used because of its potential to analyse a much wider range of materials including opaque, transparent, and even metallic samples. However, AMI in reflection microscopy has not yet been demonstrated despite its advantages. In 2018, Kowarsch *et al.* published a

theoretical investigation of the basic photo-physical relationships of AMI in reflection microscopy. The results of the theoretical study show that it is possible to create an optically induced near-field aperture in the AML with a diameter far below the optical resolution limit. They also predicted a 5-fold improvement in resolution via AMI in confocal reflection microscope.
In this thesis, we will experimentally explore the theoretical predictions presented by Kowarsch *et al.* For this purpose, a confocal reflection microscope with an additional depletion laser (similar to STED microscope) will be developed. The photochromic molecules (BTE-1) that will be used in the experiments, are identical to that used for theoretical modelling and previously used by Andrew *et al.* for AMOL. These molecules are synthesised and coated on the samples (AML) at the *Institute of Physical Chemistry (IPC)* and *Institut für Organische Chemie (IOC), TU-Clausthal.*
The foundation of the resolution enhancement via absorbance modulation is the photo-physics of BTE-1 molecules in the AML. Therefore, the first set of experiments will be designed to thoroughly investigate the behaviour of the AML in terms of its temporal and behavioural response to light exposure of different wavelengths. The result of this investigation will play a critical role in determining the experimental parameters that will be implemented for high-resolution imaging.
The subsequent structure of the thesis includes a detailed introduction to the basics of image formation in conventional and confocal microscopy as Chap.2. Thereafter, a thorough introduction to absorbance modulation and its application in reflection microscopy is discussed to provide a basic framework for understanding the research work in Chap. 3. Chap. 4 is concerned with the development of the confocal reflection microscope that will be used for experiments and high-resolution imaging. Chap. 5 provides a detailed discussion of the experiments and the obtained results during the coarse of the research work. A general summary of the thesis and future scope of the project is provided at the end of the thesis in Chap. 6.

Chapter 2

Fundamentals of Conventional and High-Resolution Microscopy

The high-resolution reflection microscope developed within the scope of this thesis is derived from the concept of confocal microscopy [13, 14] and Stimulated Emission Depletion (STED) microscopy [2, 9, 15]. This chapter describes the fundamentals of image formation of point-like objects and extended objects in conventional microscopes. Based on illumination light and object properties, imaging systems are broadly categorised as coherent and incoherent; foundational differences between the two imaging systems and their associated resolution are also explained in this chapter. In the section on confocal microscopy, we review the basics of image formation in confocal arrangement and its eminence over conventional microscopy. As STED microscopy is an extension of confocal microscopy, the basic principles and their implementation for the development of a STED microscope are also discussed later in this chapter.

2.1 Introduction to Microscopy

In this section, the basics of the image formation in a microscope are discussed. We start with the image of a point-like object and then extend the idea to the image of an extended object. The key aspects of two kinds of imaging systems, coherent and incoherent, are also discussed in detail further in this section. A key concept, resolution, which is essential to understand microscopy thoroughly, is also introduced in the following section.

2.1.1 Fundamental Unit of an Image

Consider an infinitesimally small point-like object or point source imaged by a perfect lens. A point-like object emits spherical waves in all directions. To reproduce a point image, the lens must collect and focus all the waves emanating from the object into the image plane. However, due to the finite aperture of the lens, only some of the emitted waves are collected and focused. Due to the wave nature of the light, instead of a point image, the light waves interfere at the focal point to

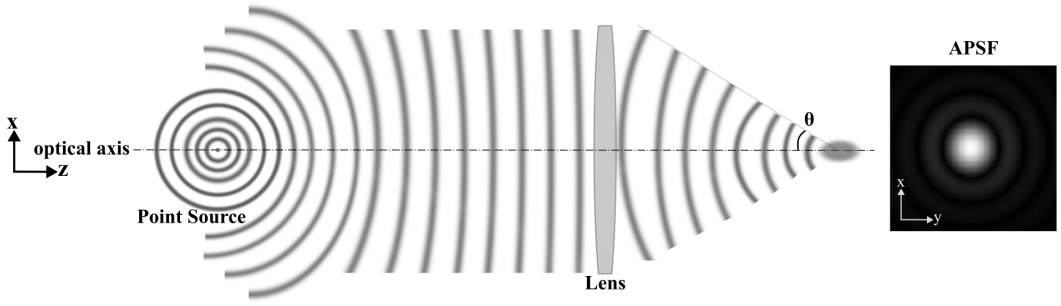

Figure 2.1: The figure demonstrates imaging of a point source using a lens. The electric field emitted from the point source is collected and focused forming a blurred pattern in the image plane. This electric field distribution is known as the APSF. The angle θ denotes the semi-aperture angle of the lens; it is the maximum angle of the cone of light that can enter or exit the lens. Additionally, the (real) electric field distribution of APSF in xy-direction in the image plane is shown [17].

produce a pattern of a bright central disk surrounded by concentric rings of light; when viewed in the x-y plane as depicted in Fig. 2.1. The electric field distribution thus generated in the image plane is known as the Amplitude Point Spread Function (APSF).

According to scalar diffraction theory with Fraunhofer approximation or the far-field approximation, the APSF, $h_A(x, y)$, generated by imaging a point-like object is given by the Fourier transform ($\mathcal{F}$) of the pupil function, $P(x, y)$, of the lens [16–18].

$$h_A(x, y) \propto \mathcal{F}\{P(x, y)\} \tag{2.1}$$

The APSF is a complex-valued function, i.e., it contains both amplitude and phase information. However, the detectors used in imaging systems can only measure intensity; hence, defining the intensity distribution known as (Intensity) Point Spread Function (IPSF) is more convenient. IPSF, $h(x, y)$, is given by the square of the modulus of APSF.

$$h(x, y) = \left|h_A(x, y) \cdot h_A^*(x, y)\right| = \left|h_A(x, y)\right|^2 \tag{2.2}$$

A lens, in general, has a circular aperture; thus, the pupil function is defined by:

$$P(x, y) = \begin{cases} 1, & \rho \leq a \\ 0, & \rho > a \end{cases}$$

Where $\rho = \sqrt{x^2 + y^2}$ is the radial position in the transverse plane from the optical

axis and a is the radius of the aperture. The APSF is then calculated as:

$$h_A(x,y) = \frac{exp(-jkd)}{j\lambda d}\pi a^2\left[\frac{2J_1(2\pi\rho a/\lambda d)}{2\pi\rho a/\lambda d}\right] \tag{2.3}$$

where J_1 is the first order Bessel function of first kind and d is the position of the imaging plane on the optical axis (z-axis) from the focal plane [17, 19]. $k = \frac{2\pi}{\lambda}$ is the wave number, here $\lambda = \lambda_o/n$, where λ_o is the vacuum wavelength and n is the refractive index of the medium. The IPSF, $h(x,y)$, the intensity pattern in the imaging plane is then given by:

$$h(x,y) = \left|h_A(x,y)\right|^2 = \left(\frac{\pi a^2}{\lambda d}\right)^2\left[\frac{2J_1(2\pi\rho a/\lambda d)}{2\pi\rho a/\lambda d}\right]^2 \tag{2.4}$$

The IPSF generated by a circular aperture is also known as the Airy pattern, named after George Biddell Airy [20]. Fig. 2.2 shows a simulation of 2D and 1D profiles of the APSF and IPSF generated by a circular pupil using vectorial diffraction theory (VDT).

Various imaging systems employ annular pupils, for e.g., dark field and phase contrast imaging systems [21, 22]. The APSF and IPSF for a thin annular pupil, with outer and inner radii a and γa such that $(1-\gamma) = \epsilon$, with $\epsilon << 1$, is given by

$$h_A(x,y) = \frac{exp(-jkd)}{j\lambda d}exp\left(\frac{-jk\rho^2}{2d}\right)2\pi\epsilon a J_0(2\pi\rho a/\lambda d) \tag{2.5}$$

$$h(x,y) = \left(\frac{2\pi\epsilon a}{\lambda d}\right)^2\left[J_0(2\pi\rho a/\lambda d)\right]^2 \tag{2.6}$$

respectively, where J_0 is the zero-order Bessel function of the first kind.

Schwarzschild objectives (SO) or reflective objective are another kind of objectives used for imaging which consist of reflecting surfaces called primary and secondary mirrors. They are based on Schwarzschild's design [23–25], such that they focus light just like a lens-based objective. However, SO have the upper hand when an imaging system needs a significant working distance and needs to work over an extended spectral range. Unlike lens-based objectives, where the refractive index of the lens varies with the wavelength and hence cannot focus all the wavelengths at the same focal point, SO are designed to focus light without introducing chromatic aberration. They also have an annular aperture, as shown in Fig. 2.3, with additional legs, also called spider legs, to hold the secondary mirror. Using VDT, simulations of the two-dimensional (2D) APSF and IPSF in the focal plane as well as one-dimensional (1D) line profiles through the PSFs are shown in Fig. 2.3.

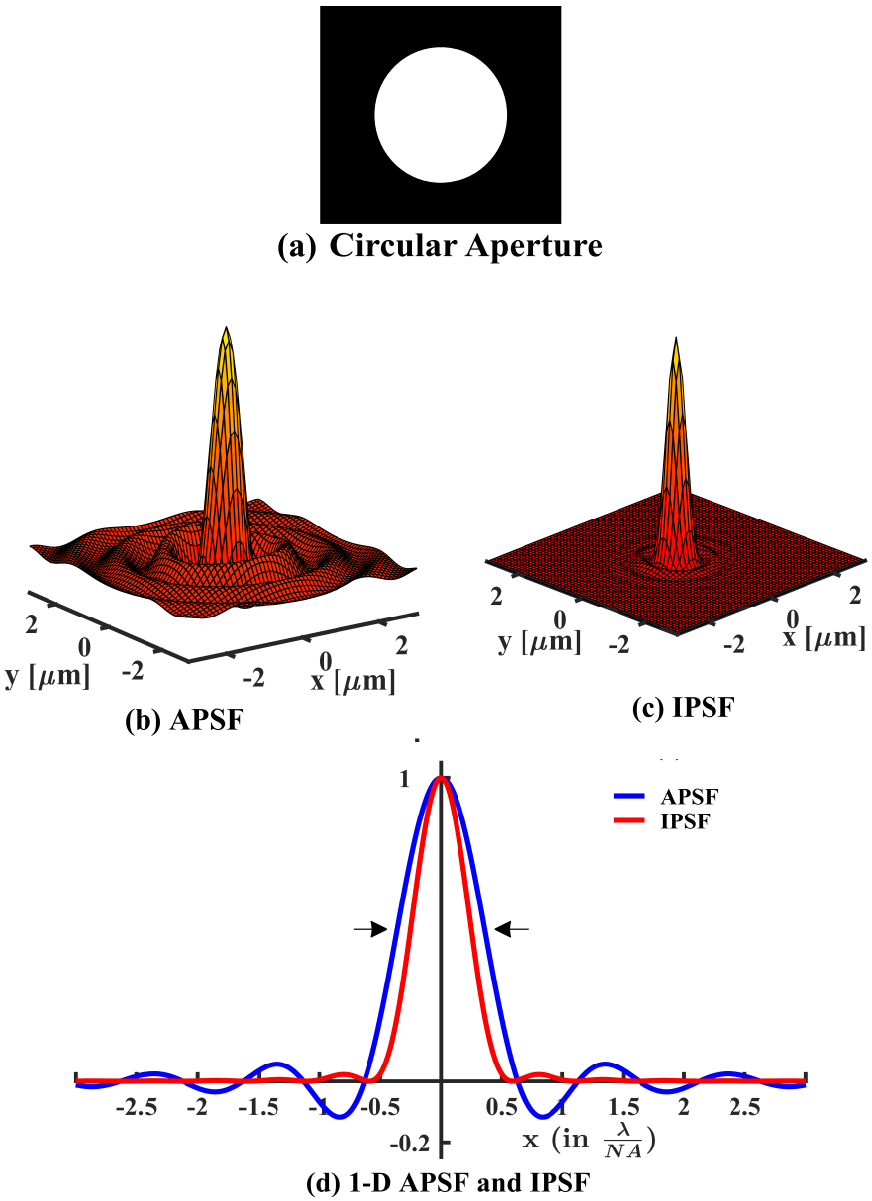

Figure 2.2: In this figure, (a) is a representation of a circular aperture of an objective lens. (b,c) Simulation of the (real) APSF and IPSF in the focal plane, generated by focusing light with a lens with a circular aperture (d) shows a normalised 1D profile through the centre of APSF (blue) and IPSF (red) shown in (b) & (c). The full width at half maximum (FWHM) of the PSFs is marked with arrows. The plots are computed for $\lambda = 633\,\mathrm{nm}$, $n = 1$ and a numerical aperture of 0.65. The x-axis shows the position of the maxima and minima of the PSFs, it is normalised with $\frac{\lambda}{NA}$.

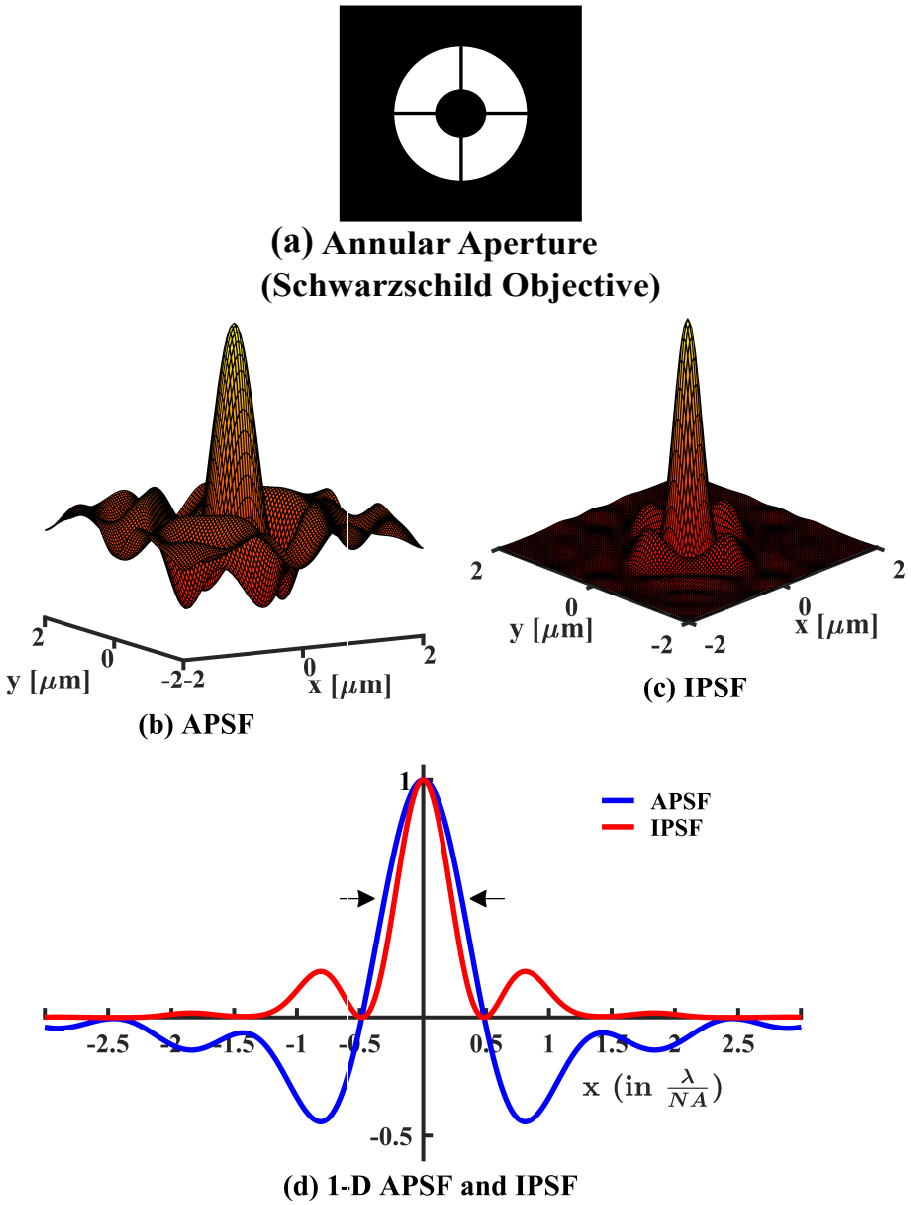

Figure 2.3: In this figure, (a) is a representation of the annular aperture of SO. (b,c) Simulation of the (real) APSF and IPSF in the focal plane, generated by focusing light with an annular aperture shown in (a). (d) shows a normalised 1D profile through the centre of APSF (blue) and IPSF (red) shown in (b) & (c). The full width at half maximum (FWHM) of the PSFs are marked with arrows. The plots are computed for $\lambda = 633\,\text{nm}$, $n = 1$ and a numerical aperture of 0.65. The x-axis shows the position of the maxima and minima of the PSFs, it is normalised with $\frac{\lambda}{NA}$.

It is clearly visible that the APSF and IPSF generated by SO are affected by the additional central obscuration. Obscuration is defined as the percentage of obstructed areas. The PSFs in Fig. 2.3 are simulated for an obscuration of 17.5%. The first bright ring of the annular aperture IPSF has a considerably higher intensity than the circular aperture IPSF. A closer look at the first minima of 1D IPSFs in Fig. 2.2d and 2.3d shows that the size of the central peak is slightly smaller for SO than those of the circular aperture (see Fig. 2.4) [23, 26].

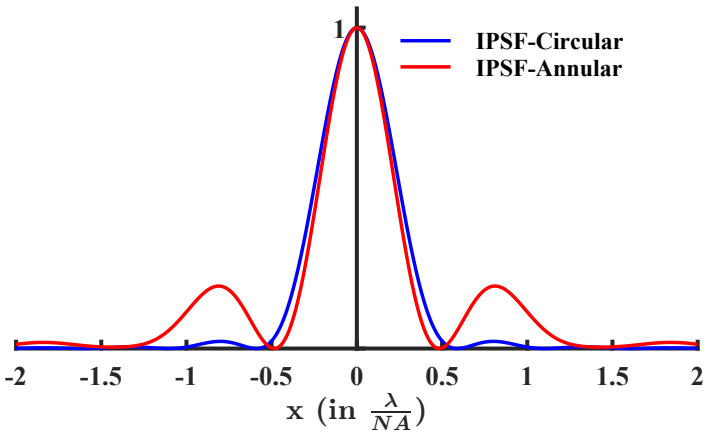

Figure 2.4: The figure compares the 1D IPSFs generated by a circular and an annular aperture. The x-axis shows the position of the maxima and minima of the PSFs, it is normalised with $\frac{\lambda}{NA}$.

2.1.2 Coherent and Incoherent Imaging Systems

An optical imaging system is comparable to a linear shift-invariant (LSI)[1] system [18, 27, 28]. An LSI system is characterised by its impulse response which defines the input-output relationship of the system. Therefore, if we have an input and a known response function, the output is calculated by convolution ($\otimes$) of the input and the response function. Mathematically, the impulse response function is defined as the output of an LSI system when a delta function, called impulse, is fed as an input. The impulse for an imaging system is synonymous with a point-like object or a point source. As previously discussed, the response function of an imaging system for a point-like object is given by the APSF or IPSF. Thus, the output image is given by combining all the individual PSFs generated by each point in the object.
A microscope collects light emanating from the sample, for e.g., fluorescence, reflected and scattered light and projects it onto an imaging plane. Based on the properties of the reflected light, which depends on the specimen and the illumination light source, the imaging systems can be broadly classified into two categories

[1]Linearity implies that the total electric field at a position in the image plane is the superposition of the contributions from different elements of the object, a direct consequence of the linearity of Maxwell's equations. The optical system is considered shift-invariant when the imaging properties are constant over the whole field of view.

coherent and incoherent.
Coherent imaging is characterised by a fixed phase relationship between the light waves emerging from different parts of the object. The image $I(x, y)$ of an object with complex amplitude $O_A(x, y)$ in a coherent imaging system is given by

$$I(x, y) = \left| O_A(x, y) \otimes h_A(x, y) \right|^2 \tag{2.7}$$

where $\otimes$ symbolises a 2D convolution. The object is defined as $O_A(x, y) = A(x, y) \cdot e^{-j\phi}$ with an amplitude $A(x, y)$ and a phase $\phi(x, y)$ and $h_A(x, y)$ is the response function of the imaging system. A coherent imaging system is linear in complex amplitude[19, 29, 30].
In incoherent imaging, phase relationships do not exist, i.e., different parts of the object have random phases. Hence, the output image I(x,y) for the incoherent system is given by

$$I(x, y) = \left| O_A(x, y) \right|^2 \otimes \left| h_A(x, y) \right|^2 = O(x, y) \otimes h(x, y) \tag{2.8}$$

The incoherent image is simply a convolution of the object intensity $O(x, y)$ and the IPSF $h(x, y)$ of the imaging system. An incoherent imaging system is linear in intensity [19, 30].

2.1.3 Resolution of a Microscope

As explained earlier, the image of a point-like object is not a point but rather an extended intensity distribution. It is determined by the pupil function of the lens, which describes the limited aperture size. Another expression that describes the convergence and divergence of the light cone is the F-number ($f\#$ or F). It is defined as $F = f/D$ where f is the focal length of the lens, and D is the diameter of the finite pupil of the lens. It is related to the numerical aperture as $F \approx 1/2\text{NA}$ [14, 16].
Resolution defines the size of the smallest detail that a microscope can resolve. There are multiple definitions and ways of determining the theoretical resolution of an imaging system. In 1873, the first definition of the resolution was given by E. Abbe [1] where he considered the object as a periodic diffraction element such as a grating and mathematically defined the resolution as:

$$d = \frac{\lambda_0}{2\text{NA}} \tag{2.9}$$

where d is the smallest resolvable grating period. The equation is famously known as Abbe's resolution limit. According to eq.(2.9), the resolution is limited to half of the wavelength used for imaging for NA = 1. The equation also suggests that

decreasing the wavelength and increasing the NA will increase the resolution of the system.

There are various criteria [31] for defining the resolution of a microscope; however, the most accepted standard is the Rayleigh criterion [32]. It states that, for a circular aperture, lens, or mirror, images of a pair of point-like objects are resolvable when the centre of the Airy pattern of one is directly over the first minimum of the Airy pattern of the other. Therefore, the minimum resolvable separation between two point objects is given as:

$$d = 1.22\frac{\lambda_0 f}{D} \tag{2.10}$$

where D is the diameter of the circular aperture, and f is the focal length of the lens. Eq.(2.10) can also be defined in terms of NA and F as:

$$d = 1.22\lambda_0 F \ = 0.61\frac{\lambda_0}{\mathrm{NA}} \tag{2.11}$$

The Rayleigh criterion presumes that the two point-like objects are emitting incoherent waves. While there is no difference between coherent and incoherent imaging of a single point object in respect of the output intensity distribution, for a pair of point objects, it might vary for the former. A simple model can be utilised to investigate whether two point-like objects separated by Rayleigh distance would be better resolved with a coherent imaging system than with an incoherent imaging system. In accordance with eq.(2.7), the coherent image of two point-like objects can be modelled as [30]:

$$\begin{aligned} I(r) &= \Big|\delta(r-\beta_1)\otimes h_A(r) + \exp(i\phi)\cdot\delta(r-\beta_2)\otimes h_A(r)\Big|^2 \\ &= \Big|h_A(r-\beta_1) + \exp(i\phi)\cdot h_A(r-\beta_2)\Big|^2 \end{aligned} \tag{2.12}$$

with $h_A(r)$ the APSF, $\delta(r)$ the Dirac delta function representing the point-like object, $r = (x, y)$ a 2D vector in the image plane, β_1 and β_2 the positions of the two objects, ϕ the relative phase between the two objects, and $\otimes$ is the convolution operator. Following eq.(2.8) and using the same imaging system in incoherent mode, the model becomes:

$$\begin{aligned} I(r) &= \Big|\delta(r-\beta_1)\otimes h_A(r)\Big|^2 + \Big|\exp(i\phi)\cdot\delta(r-\beta_2)\otimes h_A(r)\Big|^2 \\ &= \Big|h_A(r-\beta_1)\Big|^2 + \Big|h_A(r-\beta_2)\Big|^2 \\ &= h(r-\beta_1) + h(r-\beta_2) \end{aligned} \tag{2.13}$$

with $h(r)$ the incoherent IPSF and is given as the squared modulus of the APSF $h(r) = \Big|h_A(r)\Big|^2$. It is apparent from eq.(2.12) & (2.13) that the relative phase

between the point objects affects the image in coherent imaging and has no effect in incoherent imaging [30, 33]. Fig. 2.5 shows the normalised intensity profiles through the image of a pair of point like objects imaged with a coherent and an incoherent imaging system. For the latter, the image varies with the phase difference (ϕ); at $\phi = 0$, there is no dip in the intensity distribution due to constructive interference between the APSFs generated by the two-point objects. Therefore, the points are not resolved at $\phi = 0$ as in an incoherent image. At $\phi = \pi/2$, the pattern is similar to that in incoherent imaging. At $\phi = \pi$, the two maxima are more widely separated, with the intensity dip dropping to zero, indicating significantly better resolution than in incoherent image [19, 33]. It should be noted that when the two-point objects are not resolved, by coherent or incoherent imaging, they appear at an incorrect lateral position. However, this is also true in the case of coherent imaging when $\phi = \pi$, as shown in Fig. 2.5. This shift in the lateral position is one of the apparent effects of coherent imaging [34, 35].

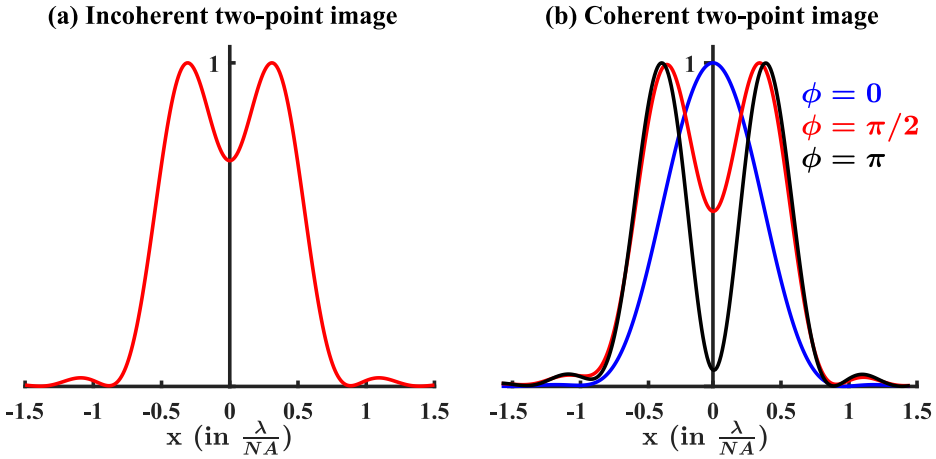

Figure 2.5: The figure shows a comparison of the intensity profile through the image of a pair of point objects formed by an (a) incoherent and (b) coherent imaging system. The coherent image (b) varies with the phase difference (ϕ) between the two points. The x-axis shows the position of the maxima and minima of the PSFs, it is normalised with $\frac{\lambda}{NA}$.

The intensity profile of an image produced by a coherent imaging system is phase-dependent, making it more complex. Merely measuring its intensity response is unsuitable for characterising its resolution limit.

When extended objects are imaged by an incoherent imaging system, the resolution can be simply estimated by the FWHM of the IPSF, which is given by:

$$d = 0.51\frac{\lambda_0}{\mathrm{NA}} \tag{2.14}$$

for a circular aperture. The advantage of using the FWHM is that it can be easily measured experimentally by imaging a pseudo point object, such as a nano gold bead, and therefore be used as a comparison unit for real microscope systems. The FWHM

of a Gaussian-fit to the experimentally obtained IPSF is a good approximation of realistically achievable system performance [36, 37].
It is worth noting that resolution is a miscellaneous concept, and measuring it is not so trivial for a coherent imaging system. In general, various external factors such as signal-to-noise ratio and contrast, although they do not affect resolution directly, alter the final image quality of the imaging system. With newly developed super-resolution imaging techniques, the definition of resolution limit has changed, and it is crucial to understand them to compare different techniques.

2.2 Confocal Microscopy

Lukosz's principle [19, 38] states that reducing the field-of-view can lead to a better resolution. In other words, if a tiny aperture is placed extremely close to the object, then the resolution is defined by the size of the aperture and not the radiation. This principle has been demonstrated at microwave frequencies [39, 40]; however, there are practical complications in placing a small aperture compared to half of the wavelength close to the object. It is even more challenging to implement the same at optical frequencies. Nevertheless, there is a way to take advantage of this principle at optical frequencies. Instead of placing a physical aperture in the focal plane, one can use a back-projected image of an aperture or a point detector in conjunction with a focused point source. The described arrangement of optics is simply known as a confocal arrangement or Type2 scanning microscope [19], as shown in Fig. 2.6. Since it is a scanning technique, the specimen is scanned by moving the source and the detector in synchronisation or simply moving the specimen itself to form a complete image.

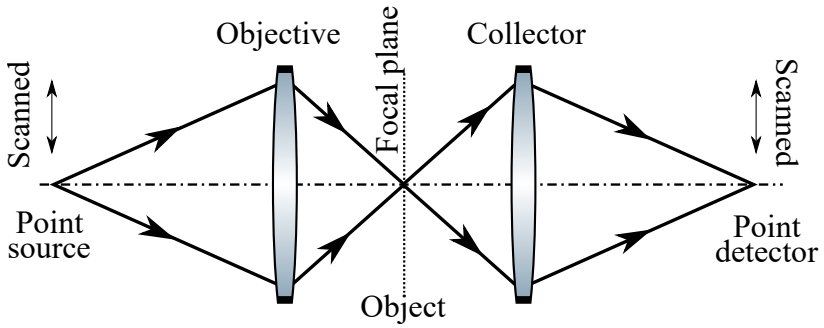

Figure 2.6: The optical arrangement of Type-2 or confocal scanning microscope. A point source illuminates a small region of the object, and the point detector detects light only from the same area [19].

In the 1950s, Minsky patented the first confocal microscope. In his setup, the sample was placed on an electronically controlled moving stage. He focused a light source through a pinhole, creating a point source, on the sample and detected the signal through another pinhole, which behaves as the back-projected aperture placed before

the detector. The placement of the pinhole in the imaging plane is such that only the signal that stems from the focal plane is detected; any out-of-focus light does not reach the detector. The point source, its image in the focal plane, and the detection pinhole lies in a conjugated plane. Fig. 2.7a shows the optical arrangement of a confocal microscope in transmission mode. The confocal microscope in a reflection mode is achieved by placing a single lens (objective) and pinhole on only one side of the sample. A half-silvered mirror or a beamsplitter (BS) is used to separate the illumination and detection light, as shown in Fig. 2.7b.

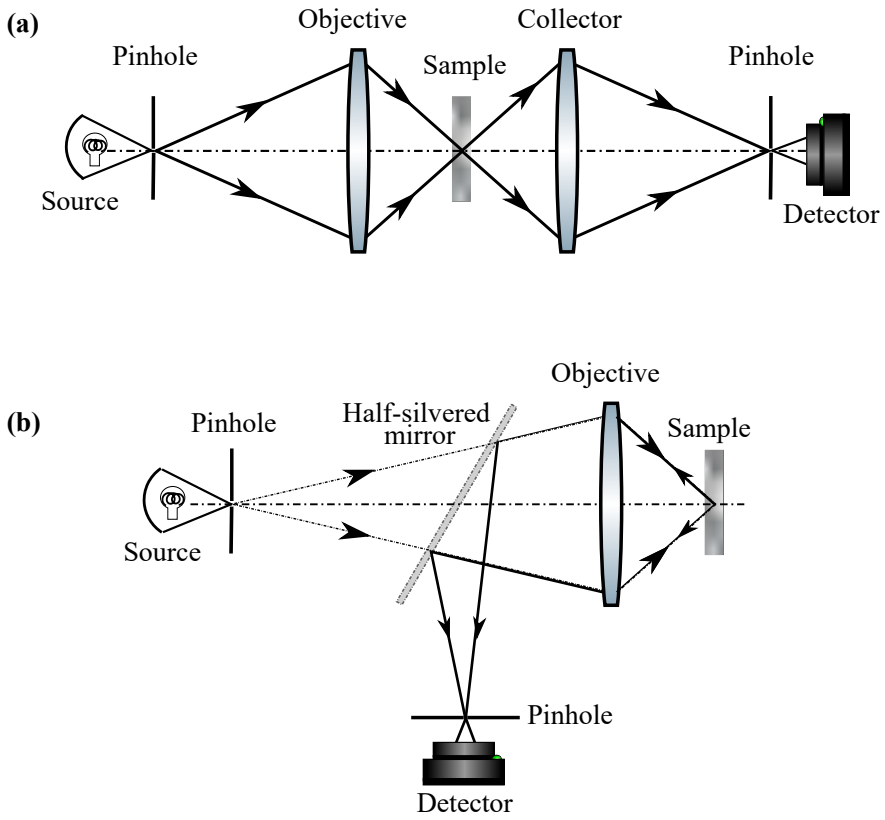

Figure 2.7: The figure shows the optical arrangement of a confocal microscope by Minsky (a) transmission mode and (b) reflection or fluorescence mode [13].

Nowadays, instead of an illumination pinhole, a laser is used as the illumination source focused on the sample through an objective lens (circular aperture), in a standard confocal microscope, generating a focal spot, referred to as illumination APSF, $h_{A,ill}(x, y)$. The detection pinhole is back-projected on the focal plane by the same objective producing a detection APSF, $h_{A,det}(x, y)$. If the pinhole is given by a pupil function, $p(x, y)$, then the detection APSF can be written as :

$$h_{A,det}(x, y) = h_{A,ill}(x, y) \otimes p(x, y) \tag{2.15}$$

The product of the illumination APSF and detection APSF defines the APSF for a

confocal imaging system, which is given as:

$$h_{A,conf}(x,y) = h_{A,ill}(x,y) \cdot h_{A,det}(x,y) \tag{2.16}$$

and the confocal IPSF is given by the product of the illumination and detection IPSFs:

$$h_{conf}(x,y) = \left|h_{A,ill}(x,y) \cdot h_{A,det}(x,y)\right|^2 = h_{ill}(x,y) \cdot h_{det}(x,y) \tag{2.17}$$

Fig. 2.8 shows the intensity profiles through the image of a point-like object imaged with a confocal microscope with a circular and an annular pupil objective. The central peak is sharpened for both the circular and annular aperture compared to the conventional IPSF described in the previous section; additionally, the side lobes are also reduced.

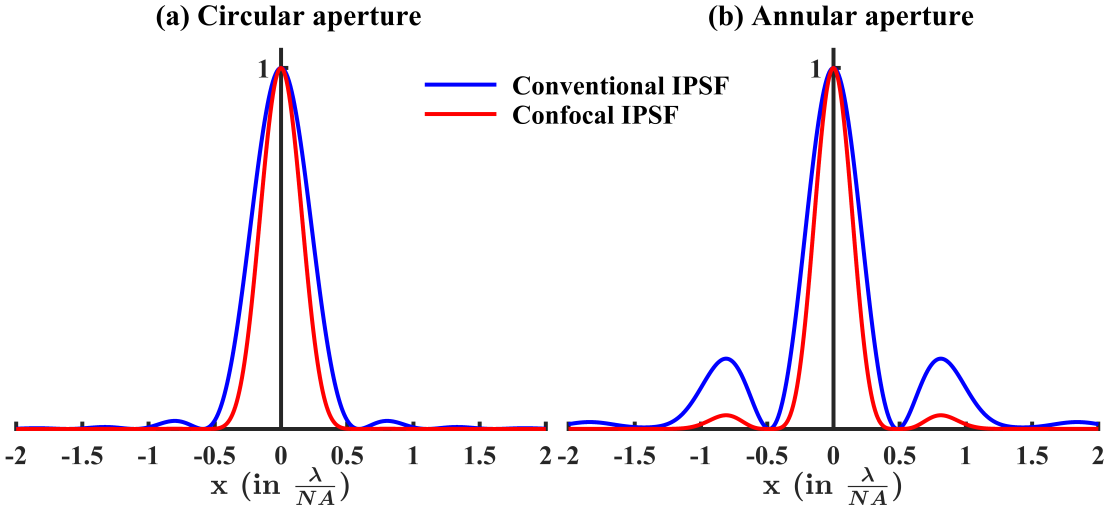

Figure 2.8: The figure shows a comparison of the intensity profiles of conventional and confocal IPSF generated by (a) circular aperture and (b) annular aperture. The confocal IPSF has a narrower central peak and suppressed side lobes. The x-axis shows the position of the maxima and minima of the PSFs, it is normalised with $\frac{\lambda}{NA}$.

Integrating the knowledge about confocal point spread functions and different kinds of imaging systems from the previous section, the image formation in a confocal microscope is given by [29]:

$$I(x,y) = \left|O_A(x,y) \otimes h_{A,conf}(x,y)\right|^2 \tag{2.18}$$

when the microscope behaves as a coherent imaging system. A confocal microscope, such as a confocal fluorescence microscope, can also be used as an incoherent imaging system. The incoherent image formation in a confocal microscope is described as:

$$I(x,y) = \left|O(x,y)\right| \otimes \left|h_{conf}(x,y)\right| \tag{2.19}$$

where, $O_A(x, y)$ and $O(x, y)$ are the object amplitude and intensity, respectively. $h_{A,conf}(x, y)$and $h_{conf}(x, y)$ are the confocal APSF and IPSF, respectively.
As mentioned before, the detectors used in the imaging systems can only measure intensity; henceforth, IPSF is referred to as PSF, as APSFs are not measurable.

Resolution of a confocal microscope

As discussed earlier, defining the resolution for a coherent imaging system is not straightforward. Hence, we will discuss the resolution of an incoherent confocal microscope. As depicted in Fig. 2.8, the size of the confocal PSF is narrower than in a conventional microscope. The size of the detection pinhole used in confocal microscopes is defined with respect to the Airy unit (AU). 1 AU is the diameter of the first minimum of the Airy pattern obtained by a circular aperture [41–43].

$$1\text{AU} = 1.22\frac{\lambda_0 M}{\text{NA}} \tag{2.20}$$

where M is the magnification of the imaging system. For a pinhole size of $\approx 1\ AU$, the FWHM of a confocal PSF is given by:

$$d_{conf} = 0.51\frac{\lambda_0 f}{\text{D}} \tag{2.21}$$

and for a pinhole size of $0.25 - 0.5\ AU$, the FWHM is given by:

$$d_{conf} = 0.37\frac{\lambda_0 f}{\text{D}} \tag{2.22}$$

In confocal microscopy, if an annular aperture is used with a pinhole of size $\approx 1\ AU$, the FWHM of the confocal PSF will be:

$$d_{conf,annular} = 0.44\frac{\lambda_0 f}{\text{D}} \tag{2.23}$$

and for a pinhole size of $0.25 - 0.5\ AU$, the FWHM is:

$$d_{conf,annular} = 0.32\frac{\lambda_0 f}{\text{D}} \tag{2.24}$$

The imaging systems discussed in this section were based on the linear interaction of the illumination source and the object. So far, we have focused on image formation and resolution basics in conventional and confocal microscopes. We also discussed the properties and distinction of coherent and incoherent imaging systems. However, to circumvent the resolution limit discussed in the previous sections, one needs to exploit the non-linear interaction of light with the object. In the next section, an incoherent, super-resolution microscopy technique, STimulated Emission Depletion

(STED), will be briefly discussed. Stefan W. Hell was awarded the Nobel Prize in Chemistry in 2014 for its development[2, 44].

2.3 STimulated Emission Depletion (STED) Microscopy

STED microscopy belongs to a family of far-field scanning optical techniques that exploit reversible fluorescence transitions to achieve super-resolution [9, 45–48]. As discussed earlier, in scanning microscopy, the illumination PSF or excitation PSF in the case of fluorescence plays a major role in determining the resolution limit of a microscope. In 1994, Hell and Wichmann proposed a method to limit the spatial extent of the illumination PSF (consistent with Lukosz's principle in section(2.2)), thereby increasing the resolution [2]. The idea is to selectively switch off fluorescence (spontaneous emission) near the periphery of excitation PSF using a high-intensity depletion beam (stimulated emission), with a characteristic doughnut-shaped PSF, which is overlapped with the excitation PSF. As a result, an effective PSF of reduced size is obtained. In the following section, the concept and implementation of STED microscopy are described in detail.

Principle of STED

A molecule (fluorophore) is excited instantaneously once illuminated with an appropriate excitation laser of wavelength λ_{exc}. The average fluorescence lifetime is in the range of a nanosecond. Consequently, a photon is spontaneously emitted as fluorescence (λ_{fl}) within some nanoseconds. Due to vibrational relaxations, λ_{fl} is always red-shifted. This is schematically shown in Fig. 2.9(left). However, a molecule can also be de-excited by a process called stimulated emission, a natural counterpart of spontaneous emission [15, 49]. When the molecule, while being in the excited state, is irradiated by a light of wavelength λ_{dep}, it relaxes to the ground state by emitting a photon that is identical to the stimulating photon (see Fig. 2.9(right)). Thus, the molecule returns to the ground state without emitting any fluorescence. λ_{dep} is equal to the energy difference between the ground and excited state (part of its emission spectrum). This stimulated emission is the basis of STED imaging.
Both the PSFs, excitation and depletion PSF, are overlapped with each other. To selectively deplete (or switch off) the fluorophores that are not in the centre of the illumination spot, depletion PSF must have zero intensity at the centre; hence, it has a doughnut shape. The characteristic doughnut shape is achieved by imprinting the beam with a 2π helical phase mask such that a nodal axis of zero intensity along the optical axis is generated in the focus of the objective lens. The emission probability of a stimulated photon is exponentially proportional to the intensity of

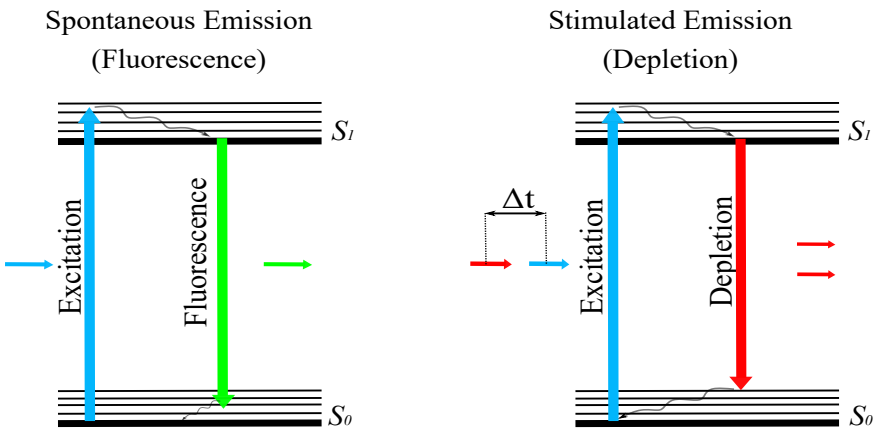

Figure 2.9: The figure illustrates the electronic states of a fluorophore, S_0 is the ground state, and S_1 is the first excited state. Multiple thin lines represent different vibrational states of S_0 and S_1. When light of the appropriate wavelength impinges on the molecule (blue arrow), a photon is absorbed, and the molecule is excited to a higher vibrational level of S_1. It quickly relaxes back to the lowest vibrational level of S_1 non-radiatively (curved arrow). Two possible de-excitation processes are shown here. On the left, the fluorophore spontaneously relaxes back to the ground state or higher vibrational state of S_0, releasing energy as a photon. This process is called fluorescence or spontaneous emission (green arrow). The energy of the emitted photon is red shifted. On the right, it shows the other de-excitation process called stimulated emission. While the molecule is in the excited state, another beam of light is illuminated with a time delay of Δt (red arrow). The photon of the second beam forces the excited fluorophore to relax back to the ground state by emitting a photon identical to itself [50].

the depletion beam. For a given fluorophore, saturation intensity (I_{sat}) is defined as the intensity of the depletion beam required to reduce the fluorescence emission by half. It is possible to empirically calculate I_{sat}. The resolution of a STED microscope strongly depends on the efficiency of stimulated emission, which eventually depends on the intensity of the depletion beam. The STED resolution and its relation to the depletion beam intensity are expressed as a refined form of Abbe's resolution equation [51, 52]:

$$d = \frac{\lambda}{2 \cdot NA \cdot \sqrt{1 + \frac{I}{I_{sat}}}} \tag{2.25}$$

Where λ is the emission wavelength, NA is the numerical aperture, I_{sat} is the saturation intensity of the corresponding fluorophore, and I denote the applied depletion beam intensity bordering the zero region. STED microscopy was first experimentally demonstrated in 1994 [2, 9]. Fig. 2.10b shows a basic STED setup with excitation and depletion laser beam, which are overlapped and temporally synchronised to arrive at the sample consecutively with a time delay of Δt. A $0 - 2\pi$ phase mask is used to create the doughnut-shaped depletion beam. The emitted fluorescence photons are discerned using a dichroic mirror and are focused on a detector. One of the essential factors in achieving high resolution is the time delay between the

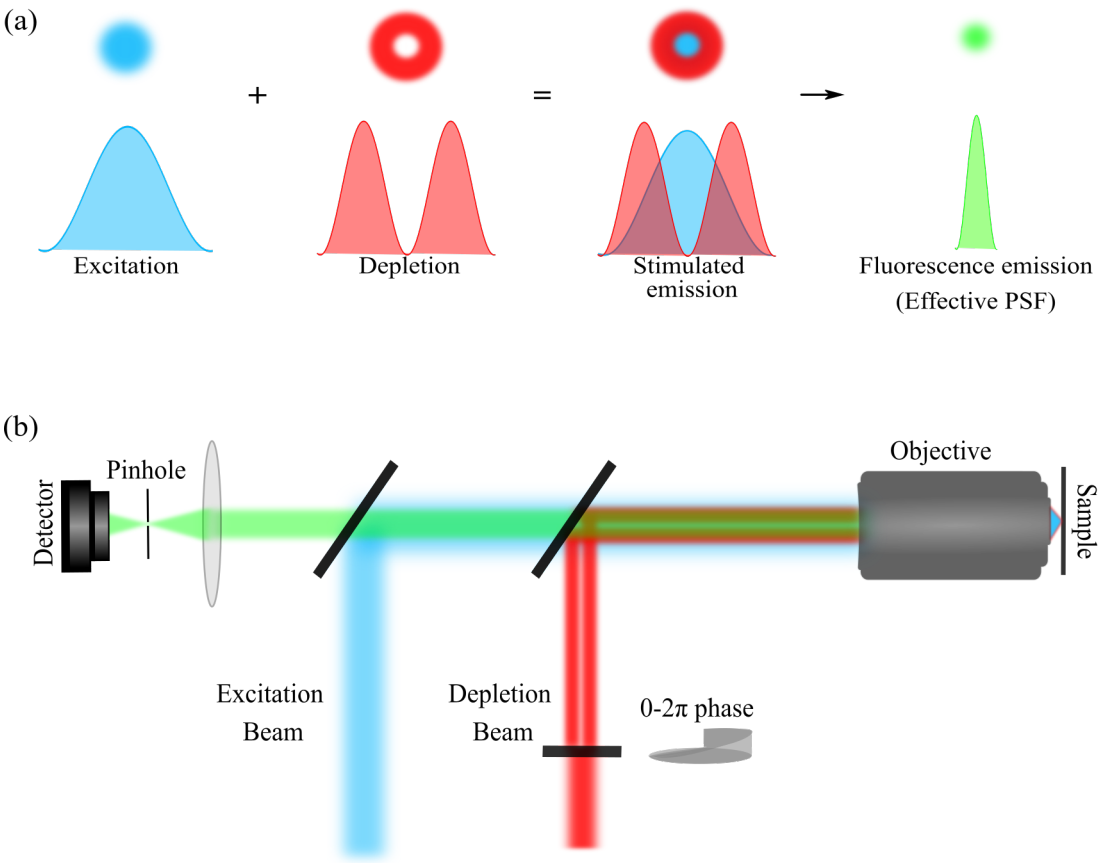

Figure 2.10: In this figure (a) demonstrates the concept of the effective PSF in STED microscopy. An excitation laser with a Gaussian-shaped focal spot (blue) is overlapped with a depletion beam of a doughnut-shaped focal spot (red). When this combination is irradiated on a fluorophore sample, the depletion beam suppresses the spontaneous emission due to the excitation laser. The suppression occurs in the illuminated region except in the doughnut's centre, which has zero intensity, effectively resulting in a sub-diffraction-limited emission spot. (b) A schematic of the experimental setup of a STED microscope. It is a confocal setup with an additional depletion beam. The depletion beam is imprinted with a $0-2\pi$ phase mask to produce a doughnut-shaped focal spot.

excitation and depletion lasers. The other factor that aids in super-resolution is the non-linear dependence of the depletion of excited molecules on the depletion beam intensity. In other words, after a specific value of depletion beam intensity, stimulated emission dominates spontaneous emission, leading to complete fluorescence suppression. Mathematically, if the ratio in the denominator $\frac{I}{I_{sat}} \to \infty$, then STED microscopy can achieve an infinite resolution. Extremely high resolution of 6 nm was attained when highly stable nitrogen-vacancy defects in diamond samples were imaged [53]. However, in biological samples,sample preservation limits the usable laser power; thus resolution between 30-80 nm is achievable.

Techniques like Gated-STED, two Photon excitation-STED, Reversible saturable optical fluorescence transitions (RESOLFT), and MINFLUX [45, 47, 54, 55] deal

with the problem of photo-bleaching, making it more suitable for life science imaging. So far, STED microscopy has been mainly implemented to study biological systems. A new concept of absorbance modulation is introduced to expand its applications in lithography and imaging in material science. In the next chapter, the foundation of absorbance modulation and its practical implementation to achieve the goal of this thesis are discussed in detail.

Chapter 3

Introduction to Absorbance Modulation Imaging (AMI)

The fundamental concept in fluorescence nanoscopy to exploit the reversible optical transitions to achieve super-resolution, as described in the previous chapter using the example of STED microscopy, is not limited to fluorescence. In 2006, Menon and Smith expanded this concept to optical lithography as absorbance modulation in optical lithography (AMOL) [3, 10]. Instead of utilising the optically reversible switchable transitions of fluorophores, a layer of photochromic molecules is used to achieve high resolution. These molecules can reversibly switch between two distinct states with different absorption properties based on the illumination wavelength. In AMOL, a thin layer of these photochromic molecules, called the absorbance modulation layer (AML), is coated on a photoresist layer. The absorbance of the AML is modulated spatially by simultaneous illumination of a doughnut-shaped spot and a Gaussian spot at two different wavelengths. Except at the null of the doughnut, the illuminated area of the AML renders opaque, creating a narrow aperture in the layer. Thus, a highly confined spot is transmitted through the aperture exposing the underlying photoresist with a nanoscale illumination spot. Andrew *et al.* have successfully used this technique to produce structures with a minimum linewidth of 35 nm. Absorbance modulation was also successfully implemented in absorbance modulation imaging (AMI) in transmitted light microscopy. Imaging of structures spaced by distances as small as ≈ 40 nm was presented [4, 12].

In material science, a more comprehensive range of samples are imaged, including opaque, transparent and metallic specimens. In 2018, Kowarsch *et al.* published a theoretical study on AMI in reflection microscopy to address this wide range of samples. They presented a theoretical model for AMI in confocal reflection microscopy and showed that imaging well beyond the diffraction limit should be feasible [5]. This thesis aims to experimentally realise AMI in reflection microscopy by developing a high-resolution reflection microscope based on this theoretical study.

This chapter will discuss the basics of absorbance modulation and its application in reflection microscopy. Absorbance modulation relies on the properties of photochromic molecules. Hence, a brief description of photochromic molecules is also

provided within this chapter. As discussed in Chap. 2, for the other imaging modalities, a resolution equation is also derived and discussed at the end of this chapter [5].

3.1 Photochromic Molecules

Photochromic molecules are widely used in ophthalmics, cosmetics, optical storage devices and photo-optical switches [56–59]. The first observation of photochromic behaviour was reported in the late 19^{th} century. *"Photochromism is a reversible transformation of a chemical species induced in one or both directions by absorption of electromagnetic (EM) radiation between two forms having different absorption spectra"* [56]. The most common model to describe photochromism is a simple two-way reaction between molecular species A and B. The reaction is assumed unimolecular even though sometimes it might involve other molecular species. Fig. 3.1 shows the energy diagram of a unimolecular photochromic molecule. A potential barrier of ΔE separates the energy states of molecular species A and B. Depending on the value of this potential barrier, the photochromic system is characterised as either T-type or P-type. If the barrier is low, B is metastable and can revert to A spontaneously. Such systems are T-type, where T refers to the thermally induced transition from B to A. On the other hand, a high barrier attributes a bistable system, where only photons can cause the reaction from B to A. Such systems are called P-type, where P denotes photochemically induced reaction.

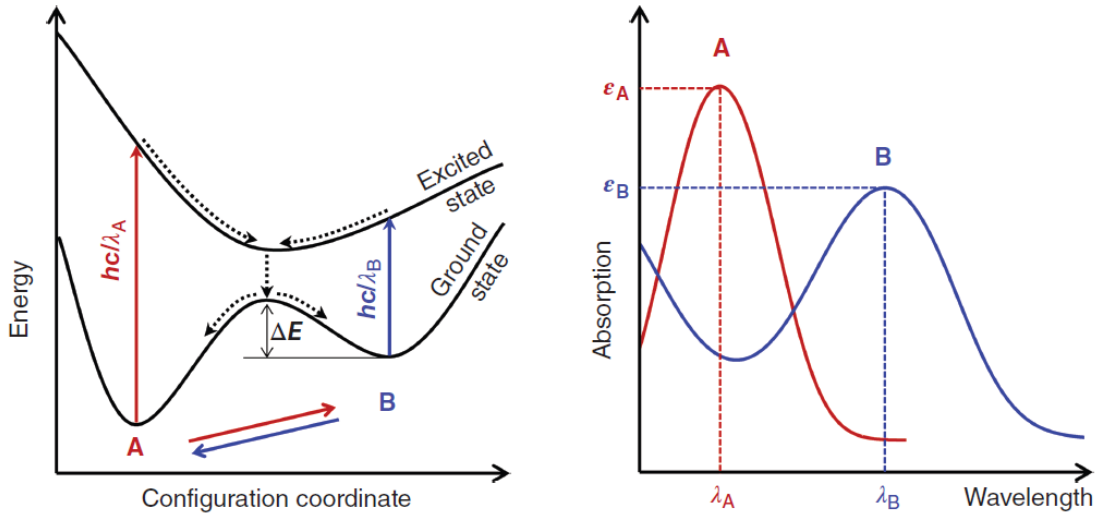

Figure 3.1: (left) Potential energy diagram of a unimolecular photochromic system. (right) The absorption spectra of the molecular species A and B. ε_A and ε_B are the absorption cross-sections of A and B, respectively, at the characteristic absorption wavelengths λ_A and λ_B, respectively. Taken from [60].

Generally, the molecular species A absorbs in the UV region and B absorbs in the VIS region of the EM spectrum, with a characteristic absorption band at λ_A and

λ_B, respectively. ε_A and ε_B are the absorption cross-sections of molecules in state A and B at λ_A and λ_B, respectively. When a photon of energy hc/λ_A, where h is the Planck's constant and c is the speed of light in vacuum, is absorbed, the molecular species A is excited from the ground state to an excited state. The excited molecule will transform into a molecule of the species B depending on the probability $QE_{A\rightarrow B}$, also known as the quantum yield or quantum efficiency (QE). On the contrary, molecule of species B will convert back to species A with a probability of $QE_{B\rightarrow A}$ when it is excited at λ_B. Different absorption spectra result in different optical and physical properties of the photochromic molecules in the two distinct forms, A and B.

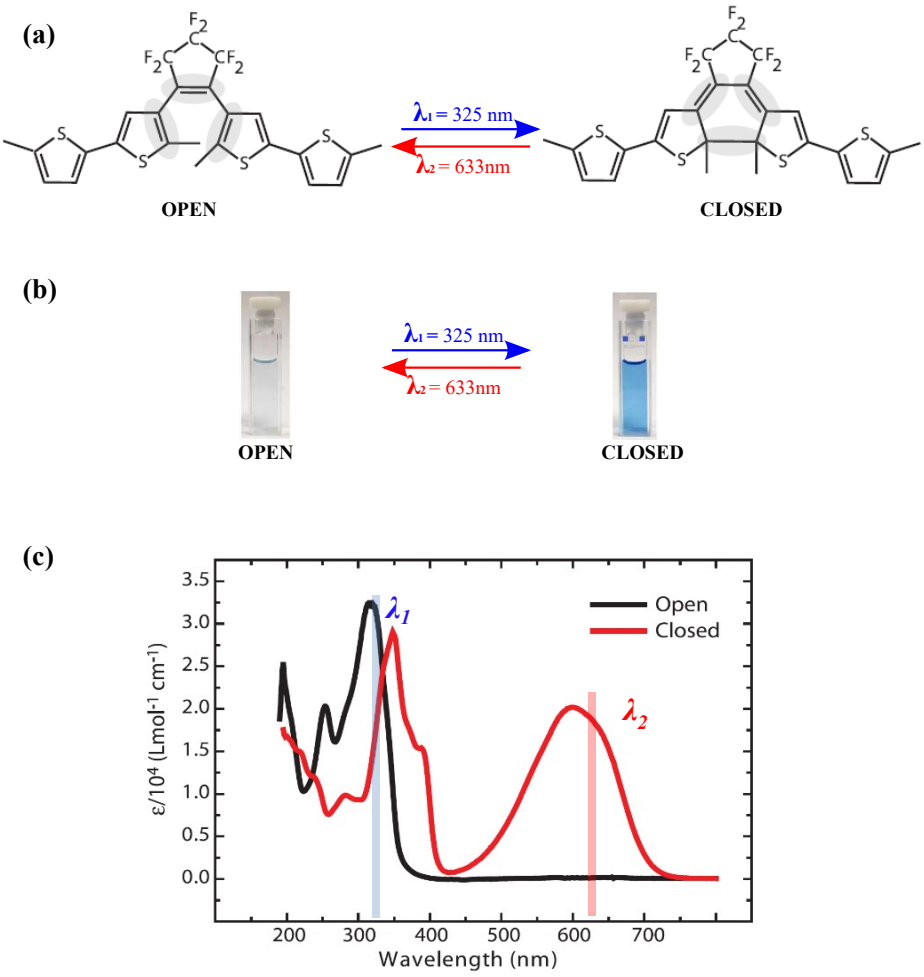

Figure 3.2: (a) Molecular structure of BTE-1 molecules in their isomeric open and closed forms. (b) The photochromic molecules switch between two states, namely, the open and closed states, which look colourless or lightly coloured and blue coloured, respectively. (c) The absorption spectra of the BTE-1 in open and closed form. ε is the decadic molar absorptivity [11].

In this thesis, the photochromic molecules comprising the AML, spin-coated on the samples for experiments, are P-type photochromic molecules from the family

of diarylethene. The specific type of diarylethene explored in our experiments is $1,2-bis(5,5'-dimethyl-2,2'-bithiophenyl)\ perfluorocyclopent-1-ene$, referred to as BTE-1. These molecules have a central benzene ring. As mentioned before, the photochromic molecules inter-convert between two isomeric forms. In one of these isomeric forms, the central benzene ring is "open", hence, referred to as the open state (O). In the other isomeric state, the benzene ring is "closed" and hence, is referred to as the closed state (C). Fig. 3.2a and 3.2c show the BTE-1 molecule in its open and closed state and the absorption spectra of the BTE-1 in the two isomeric forms, respectively. Fig. 3.2b shows the thermodynamically stable state of BTE-1, open state, in solution form, which is colourless or lightly coloured. Upon UV irradiation, the BTE-1 switches to a blue-coloured closed state.
In absorbance modulation, the AML is switched between the two states, and in practice, the AML must be stable and should be able to undergo numerous switching cycles. The property that describes the ability of the photochromic molecule to undergo numerous cycles is called fatigue resistance. A cycle is when BTE-1 is photochemically switched between the two isomeric forms, open to closed, also referred to as "switch OFF" and closed to open as "switched ON". The number of cycles BTE-1 can undergo is an essential experimental parameter and is explored in detail later in Chap. 5.

3.2 Absorbance Modulation

The concept of absorbance modulation is inspired by STED microscopy. However, instead of utilising the optically reversible switchable transitions of fluorophores, a layer of photochromic molecules, AML, is used to achieve high resolution. Analogous to STED microscopy, two lasers are simultaneously illuminated on the AML-coated sample. When a focal spot of measurement beam at λ_2 is co-illuminated with a doughnut-shaped spot of confinement beam at λ_1, the region of the AML affected by λ_1 converts to state C and is opaque to λ_2. Except for the region at the zero-intensity centre of the doughnut and the focal spot of λ_2, AML remains in state O and is transparent to λ_2. Therefore, λ_2 photons can penetrate through the sub-wavelength dynamic aperture generated in the AML as shown in Fig. 3.3a. It is worth noting that the PSFs of the two laser beams, measurement and confinement beam, are diffraction-limited, but the effective illumination PSF that penetrates through the AML is governed by the photochemistry of the layer and thus can surpass the diffraction limit [3, 10]. Absorbance modulation is a relatively new technique used in optical lithography, AMOL, and transmission microscopy, AMI, demonstrating a high lateral resolution [3, 4]. Until recently, the application of absorbance modulation in reflection microscopy was not investigated. A theoretical

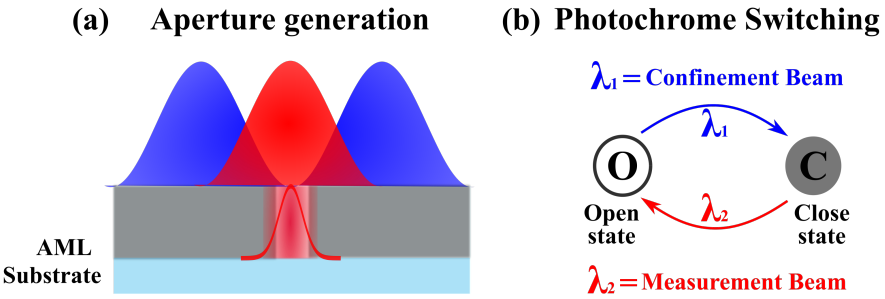

Figure 3.3: Scheme of absorbance modulation. (a) Simultaneous illumination of a Gaussian focal spot at λ_2 (633 nm) and a doughnut-shaped focal spot at λ_1 (325 nm) generates a sub-wavelength aperture through the AML. The size of the effective illumination PSF, shown in the layer, is below the diffraction limit. (b) The switching of photochromic molecules between two states, open state (O) and close state (C), upon respective illumination of λ_2 and λ_1.

model of AMI in reflection microscopy was recently published [5], showing that imaging beyond the diffraction limit is feasible. The following section will discuss the theoretical model and implementation of absorbance modulation for AMI in confocal reflection microscopy.

3.3 Modeling AMI in Reflection

A combination of dual-wavelength exposure and spectrally reversible photochromism in the AML allows light confinement to a sub-diffraction spot. The size of the generated aperture and the effective PSF depends on the AML (BTE-1 molecules) properties and the parameters of the two superimposed laser beams. A comprehensive model is required to understand and analyse the technique of absorbance modulation. This section presents a brief review of the theoretical model, specifically for reflection microscopy [5], to facilitate understanding of AMI in reflection microscopy.

In order to understand the role of photochromic molecules in aperture generation during illumination with two lasers, a kinetic model of the photochromic reaction is considered. For this purpose, a P-type bistable system is assumed where the conversion between the two isomeric states A and B is light-driven, thermally stable and follows first-order kinetics [61]. The switching A $\rightarrow$ B is induced by the light with confinement wavelength λ_1 and B $\rightarrow$ A by the light with measurement wavelength λ_2 [1]. Some parasitic absorption also exists i.e., some photons at λ_1 are absorbed in state B and vice versa. When a sample coated with photochromic molecules is simultaneously illuminated with light of both wavelengths, the photochromic molecules in the AML experience a dynamic process until a photostationary state is achieved.

[1] The states A and B are for generic nomenclature. For the BTE-1 molecules, state A corresponds to open state O, and state B corresponds to close state C

Let the concentration of photochromic molecules in state A and state B be given by $C_A(r,z,t)$ and $C_B(r,z,t)$, respectively, in molecules m^{-3}, at radial and axial position r and z and time t (see Fig. 3.4). The conservation of photochromic molecules in the AML, ignoring any photo-bleaching or other reactions gives $C_{tot} = C_A + C_B$. Given that the AML layer is homogeneous and consists of photochromic molecules in its two isomeric states, A and B, the composition of the mixture evolves with the following general differential equation:

$$\begin{aligned}\frac{d}{dt}C_A(r,z,t) &= -\frac{d}{dt}C_B(r,z,t)\\ &= -\phi_{\lambda_1}(r,z,t)\Big[\sigma^{\lambda_1}_{A\to B}\ C_A(r,z,t) - \sigma^{\lambda_1}_{B\to A}\ C_B(r,z,t)\Big]\\ &+ \phi_{\lambda_2}(r,z,t)\Big[\sigma^{\lambda_2}_{B\to A}\ C_B(r,z,t) - \sigma^{\lambda_2}_{A\to B}\ C_A(r,z,t)\Big] + k_B\ C_B(r,z,t)\end{aligned} \tag{3.1}$$

where $\phi_{\lambda_1}(r,z,t)$ and $\phi_{\lambda_2}(r,z,t)$ are the local photon flux density at the confinement and measurement wavelength, in photons $\mathrm{s}^{-1}\,\mathrm{m}^{-2}$, respectively. The change of concentration of molecules in state A is proportional to the interaction cross-sections $\sigma^{\lambda_n}_{A\to B}$ and $\sigma^{\lambda_n}_{B\to A}$, in m^2, for A $\to$ B and B $\to$ A conversion at the confinement and measurement wavelength ($n = 1, 2$), respectively. The interaction cross-sections are calculated using the absorption cross-sections, $\varepsilon^{\lambda_n}_{A,B}$ ($n = 1, 2$), and the quantum yield, $QE_{A\to B}$, $QE_{B\to A}$, of the respective states and wavelengths. The absorption cross-section, in m^2, describes the probability of an absorption process. Quantum yield is a unit less quantity that describes the efficiency of conversion of states per mole of the photons absorbed by the photochromic molecules. Although the AML is made from P-type, there are some thermal relaxations of state B. k_B is the thermal rate that accounts for the thermal relaxations. Fig. 3.4 shows the schematic of the AML on the substrate and the coordinates assumed in the modelling of AMI in reflection.

For simplicity of the model, the photochromic molecules in the AML are assumed to be randomly oriented, and the EM fields of the illumination light are considered unpolarised. The influence of the photon flux reflected at the substrate surface must be considered to model AMI in reflection. As shown in Fig. 3.4, the photon flux in the illumination direction is denoted by $\phi^{\rightarrow}_{\lambda_n}$ and the reflected photon flux is denoted by $\phi^{\leftarrow}_{\lambda_n}$. Therefore, the photon flux at a position and time (r,z,t) is a superposition of all the local photon fluxes, illuminating and reflected. It is referred to as omnidirectional photon flux ($\phi^{\leftrightarrow}_{\lambda_n}$) and is given as $\phi^{\leftrightarrow}_{\lambda_n} = \phi^{\rightarrow}_{\lambda_n} + \phi^{\leftarrow}_{\lambda_n}$.

When illuminated on the AML, the two beams, measurement and confinement beam, are absorbed to generate the aperture. The Lambert-Beer law relates the attenu-

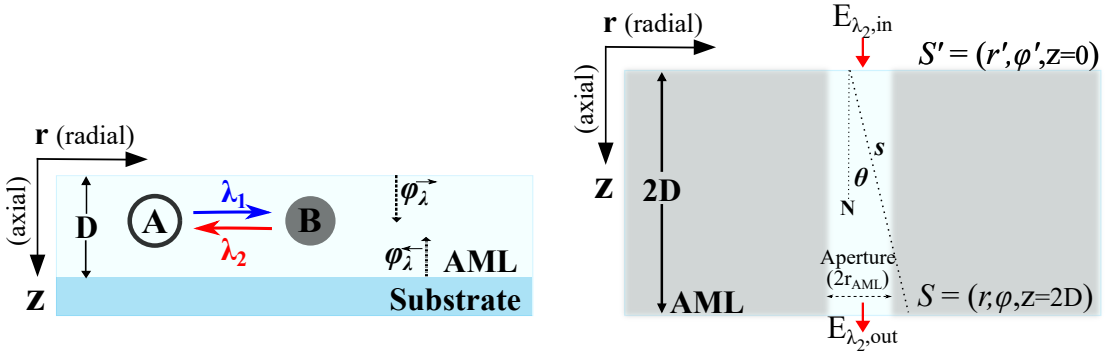

Figure 3.4: The model coordinate system is (r, z, t), where r is the radial, z is the axial coordinate and t is the time. An AML of thickness D is coated on the sample containing molecules that can inter-convert between states A and B by absorbing photons of the wavelenghts λ_1 and λ_2. The illumination of the laser is in the direction of the z-axis. The photon flux in the illumination direction is denoted by $\phi^{\rightarrow}_{\lambda_n}$ and the photon flux reflected from the substrate is denoted by $\phi^{\leftarrow}_{\lambda_n}$, with $n = 1, 2$.(right) The model coordinate system for imaging through the aperture. Double thickness $(2D)$ of the AML is considered to incorporate the reflection from the substrate surface. N is the normal and s is the straight path between $S' = (r', \phi', z = 0)$ and $S = (r, \phi, z = 2D)$. θ is the angle between the normal N and s. The grey and transparent area within the AML portrays the sub-wavelength aperture of diameter $2r_{AML}$.

ation of light intensity to the properties of the medium through which the light is travelling. According to this law, the photon flux decays exponentially along the depth of the AML. Both the incoming and reflected photon flux of both wavelengths influence the aperture generation. The local omnidirectional photon flux for λ_n $(n = 1, 2)$ at time t and radial and axial positions at r and z is given by:

$$\begin{aligned}
\phi^{\leftrightarrow}_{\lambda_n}(r,z,t) = \;& \phi^{\rightarrow}_{\lambda_n}(r,z,t) + \phi^{\leftarrow}_{\lambda_n}(r,z,t) \\
= \;& \phi_{\lambda_n,in}(r)\;\exp\left[-\int_0^z \alpha_{\lambda_n}(r,\zeta,t)\,d\zeta\right] \\
+ \;& \phi_{\lambda_n,in}(r)\;R_{\lambda_n}\;\exp\left[-\int_0^D \alpha_{\lambda_n}(r,\zeta,t)\,d\zeta - \int_z^D \alpha_{\lambda_n}(r,\zeta,t)\,d\zeta\right]
\end{aligned} \tag{3.2}$$

Here ζ is the integration variable for the axial position, and D is the thickness of the AML. $\phi_{\lambda_n,in}(r)$ is the incident photon flux of the confinement and measurement wavelength $(n = 1, 2)$ on the surface of the AML and R_{λ_n} is the reflectance of the confinement and measurement beam at the boundary between the AML and the substrate surface, and it is calculated using the Fresnel equations [27]. $\alpha_{\lambda_n}(r, \zeta, t)$ is the absorption coefficient, given by the product of the absorption cross-section, $\varepsilon^{\lambda_n}_{A,B}$ for both the states and concentration of molecules in each state. Mathematically it is expressed as:

$$\alpha_{\lambda_n}(r,\zeta,t) = \varepsilon^{\lambda_n}_{B}\;C_B(r,\zeta,t) + \varepsilon^{\lambda_n}_{A}\;C_A(r,\zeta,t) \tag{3.3}$$

The photon fluxes of the illuminated beams decrease over depth, influencing the photochromic molecules' local concentrations in states A and B. The set of equations, eq.(3.1) and (3.2), are solved numerically to describe the sub-diffraction aperture generation in the AML.

Since it is instructive for the experimental design to understand the dynamics of aperture generation, it was simulated for BTE-1. Following Kowarsch *et al.*, the incoming PSFs of the confinement and measurement beam were assumed to be Laguerre-Gaussian polynomials. The following equations were employed for modelling axially symmetric PSFs for the incoming photon flux densities:

$$\phi_{\lambda_1,in}(r) = \frac{\lambda_1}{hc}\,\frac{4}{\pi}\,\frac{P_1}{W_1^2}\left(\frac{r}{W_1}\right)^2 \exp\left[-2\left(\frac{r}{W_1}\right)^2\right]$$
$$\phi_{\lambda_2,in}(r) = \frac{\lambda_2}{hc}\,\frac{2}{\pi}\,\frac{P_2}{W_2^2}\,\exp\left[-2\left(\frac{r}{W_2}\right)^2\right] \tag{3.4}$$

With the photon energy hc/λ, h is the Planck constant, c is the velocity of light and λ is the wavelength. r is the radial position, P_1 and P_2 are the power of each beam and W_1 and W_2 are the waist radii[2].

For the simulation, an AML of 200 nm thickness is simultaneously exposed to a doughnut-shaped PSF at λ_1 and Gaussian PSF at λ_2. The waist radii, 425 nm (or FWHM = 500 nm) and powers of 1 µW are kept the same at both wavelengths. Fig. 3.5 shows snapshots of simulation of aperture generation at different time stamps of 50 µs, 2 ms, 10 ms, 30 ms and 50 ms. The initial state of the photochromic molecules in the AML is assumed to be in state A i.e., transparent for λ_2. The figure shows the evolution of the aperture in terms of change in concentration of molecules in state A and state B. The width of the channel decreases with the increasing time of illumination. A significant change in the width of the aperture is seen after 10 ms of illumination. However, the AML does not reach the photostationary state until 50 ms of illumination. The time required to generate the aperture depends on the powers of confinement and measurement beams. Here we have shown an illustration of when the illumination power and width of the PSFs are kept the same.

The dynamics of aperture generation can also be analysed as in terms of change in absorbance of the BTE-1 molecules at λ_1 and λ_2. Fig. 3.6 shows the spatial distribution of absorbance at (left) λ_1 and (right) λ_2, for various illumination times. The change in the width of the curves indicate the narrowing of the aperture. The arrow indicates the increasing time of illumination from 10 µs − 50 ms. The parameters

[2]The waist of the Gaussian beam is the radius at which the intensity has decreased to $1/e^2$ or 13.5% of its peak value. For a doughnut beam the waist is the diameter at which the intensity of the valley has increased to 86.5% of its minimum value.

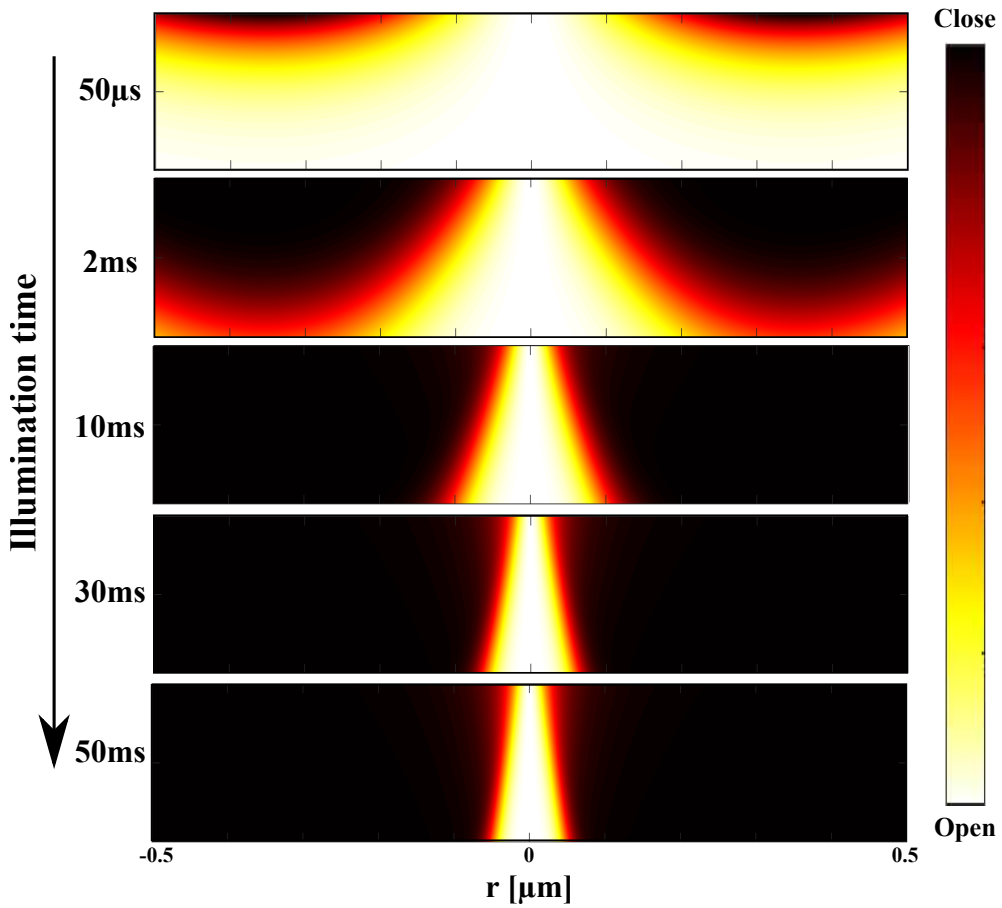

Figure 3.5: The figure shows snapshots of the change in concentration of molecules in state A (open) and state B (close) in an AML of 200 nm thickness. The initial state of the photochromic molecules in the AML is assumed to be in state A. The dark region in the AML depicts the molecules in a close state, and the bright central region is the sub-wavelength aperture generated via absorbance modulation. The illumination of measurement and confinement beams are simulated using eq.(3.4) at $P_1 = 1\,\mu W$ and $P_2 = 1\,\mu W$. It is simulated for 50 ms, here snapshots are shown as different time points. All the parameters listed in table 3.1 & 3.2 are used in the simulation. z and r are the axial and radial position as described in Fig. 3.4.

listed in table 3.1 & 3.2 are used in the simulation. Since no parasitic absorption occur at λ_2, the minimum absorbance reaches zero, whereas, due to parasitic absorption at λ_1 ($\varepsilon_B^{\lambda_1}$), absorbance does not reach a minimum of zero.

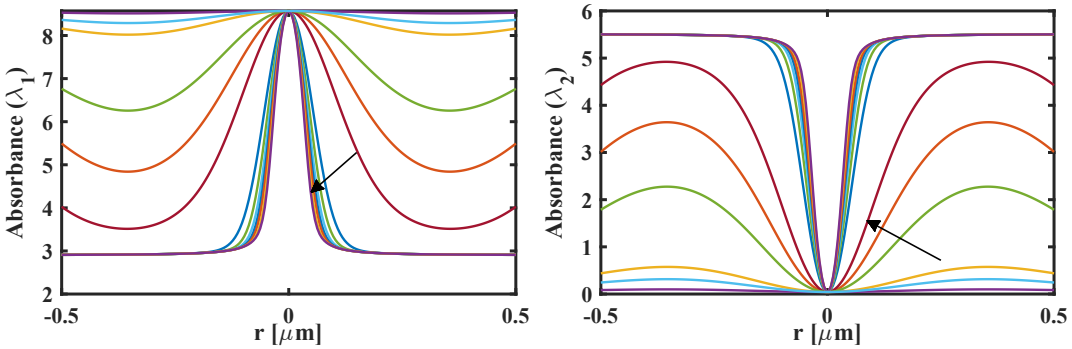

Figure 3.6: The spatial distribution of absorbance of the AML at (left) λ_1, and (right) λ_2 at illumination times, along the radial position. The arrows indicate the increasing illumination time: 10 µs, 50 µs, 100 µs, 500 µs, 1 ms, 2 ms, 10 ms, 15 ms, 20 ms, 25 ms, 30 ms, 40 ms and 50 ms.

Absorption cross-section	**Value**
$\varepsilon_A^{\lambda_1}$	$1.19 \times 10^{-20}\text{m}^2$
$\varepsilon_A^{\lambda_2}$	$6.04 \times 10^{-23}\text{m}^2$
$\varepsilon_B^{\lambda_1}$	$4.02 \times 10^{-21}\text{m}^2$
$\varepsilon_B^{\lambda_2}$	$7.66 \times 10^{-21}\text{m}^2$
Quantum Yield	**Value**
$QE_{A\to B}$	0.24
$QE_{B\to A}$	0.00088

Table 3.1: Photochromic parameters for BTE-1. Note that the parameters are given in natural logarithmic (Napierian) form in the tables. The chosen wavelengths are $\lambda_1 = 325\,\text{nm}$ and $\lambda_2 = 633\,\text{nm}$ [11].

Interaction cross-section	**Value**
$\sigma_{A\to B}^{\lambda_1}$	$2.86 \times 10^{-21}\text{m}^2$
$\sigma_{B\to A}^{\lambda_1}$ (Parasitic)	$3.54 \times 10^{-24}\text{m}^2$
$\sigma_{B\to A}^{\lambda_2}$	$6.74 \times 10^{-24}\text{m}^2$
$\sigma_{A\to B}^{\lambda_2}$ (Parasitic)	0m^2
Thermal rate	**Value**
k_B	$3 \times 10^{-6}\text{s}^{-1}$
C_0	$2990 \times N_A$ molecules m^{-3}

Table 3.2: Photochromic parameters for BTE-1. The interaction cross-sections are calculated by multiplying the absorption cross-section and the specific quantum yield. The initial concentration of BTE-1 in the AML is calculated using the Lambert-Beer law, here N_A is the Avogadro's number [11].

To image an extended object using AMI in reflection, the dynamic aperture is

rastered over the measurement surface. Therefore, the time required to reach a dynamic equilibrium, t_{stat}, also referred to as time to equilibrium, to generate the aperture is a critical parameter. It determines the pixel dwell time (time at each scan position) and consequently, the image acquisition speed of the imaging system. Kowarsch *et al.* derived an analytical solution of eq. (3.1) & (3.2), to determine t_{stat} for AMI in reflection microscopy, which is given as:

$$t_{stat} > 5 \left[(1+R_{\lambda_1})\, \phi_{\lambda_1,in}\, (\sigma_{A\to B}^{\lambda_1}+\sigma_{B\to A}^{\lambda_1}) + (1+R_{\lambda_2})\, \phi_{\lambda_2,in}\, (\sigma_{A\to B}^{\lambda_2}+\sigma_{B\to A}^{\lambda_2}) \right]^{-1} \quad (3.5)$$

Here $\phi_{\lambda_n,in}$ $(n = 1, 2)$ is the incident photon flux density of the confinement and measurement beam, and $\sigma_{A\rightleftharpoons B}^{\lambda_1}$ and $\sigma_{A\rightleftharpoons B}^{\lambda_2}$ are the interaction cross-sections of the molecules in state A and B at λ_1 and λ_2, respectively. Eq. 3.5 shows an inverse relationship between the photon fluxes and t_{stat}. Additionally, since $QE_{B\to A}$ is significantly low, the photon flux of λ_1 primarily controls t_{stat}. This correlation agrees with the simulations as well. An identical absorbance curve is obtained just after 1 ms of illumination, when the AML is exposed to high illumination powers of the measurement and confinement PSFs, $P_1 = 40\,\mu W$ and $P_2 = 40\,\mu W$ (not shown). Kowarsch *et al.* used a beam propagation model using the Huygens-Fresnel principle to model the imaging through the generated sub-wavelength aperture. It propagates an input complex electric field, $E_{\lambda_2,in}$, through the AML in the photo stationary state. Propagation through the AML with a double thickness, such that $0 \leq z \leq 2D$, is calculated, first the original and then its mirrored version at the substrate surface, to incorporate the reflection at the substrate surface. Hence, it considers a modified local photostationary absorption coefficient, α_{stat,λ_2}, along the depth $(2D)$ of AML. The superposition of the spherical waves emerging from the complex electric field at $z = 0$ is calculated at $z = 2D$ to give the exiting complex electric field, $E_{\lambda_2,out}$. Mathematically, it is given as:

$$E_{\lambda_2,out}(r, \phi, z = 2D) = \\ \frac{-i}{\lambda_2} \int_0^\infty E_{\lambda_2,in}(r', z = 0)\, r' dr' \left[\int_0^{2\pi} \frac{\exp ik|s|}{|s|} cos(\theta) \exp\left(\frac{-1}{2} \int_s \alpha_{stat,\lambda_2}\, ds \right) d\phi' \right] \quad (3.6)$$

with $r, r'$and ϕ, ϕ' as the radial and angular coordinates, respectively. $k = 2\pi n_{AML}/\lambda_2$ is the wave number with n_{AML} as the refractive index of the AML and λ_2 is the measurement wavelength. s is the straight path between $S' = (r', \phi', z = 0)$ and $S = (r, \phi, z = 2D)$ and θ is the angle between vector $S - S'$ and the normal to the AML (see Fig. 3.4). $cos(\theta)$ is the obliquity factor, same as in Rayleigh-Sommerfeld diffraction formula [17, 27]. For AMI in reflection, it is crucial to consider the reflec-

tion at the boundary between AML and the ambient medium with refractive index n_{amb} and n_{AML}, respectively. The reflectance at the measurement wavelength in the photostationary state is

$$R^{AML}_{stat,\lambda_2}(r, z = 0) = \left| \frac{n_{amb} - n_{AML} + i\frac{\lambda_2}{4\pi}\alpha_{stat,\lambda_2}(r, z = 0)}{n_{amb} + n_{AML} - i\frac{\lambda_2}{4\pi}\alpha_{stat,\lambda_2}(r, z = 0)} \right|^2 \tag{3.7}$$

The reflectance at this boundary increases with the absorption coefficient, α_{stat,λ_2}, of the AML. This also results in a constant background during imaging.

3.3.1 Lateral Resolution Enhancement

The absorption distribution within the AML provides an axially symmetric transparent channel [5]. This channel confines the region in which the measurement beam can traverse by absorbing photons in the out-of-centre regions, thereby an effective illumination PSF is generated that is smaller than the diffraction limited measurement PSF (see Fig. 3.3). If the diameter of the generated aperture is $2r_{AML}$ and the FWHM of the measurement PSF is denoted by Δx, then for a resolution enhancement aperture diameter must be less than the FWHM of the measurement PSF, $2r_{AML} < \Delta x$. The FWHM of the effective PSF, Δx_{AMI}, is therefore determined by the FWHM of the generated aperture:

$$\Delta x_{AMI} \approx 2r_{AML} \tag{3.8}$$

After time t_{stat} of illumination with the measurement and confinement beams, the photochromic molecules reach a photostationary state. The rate equation, eq.(3.1), of a thermally stable AML such that $k_B = 0$, in photostationary state is set equal to zero:

$$\begin{aligned} &\frac{d}{dt}C_A(r, z, t) = \frac{d}{dt}C_B(r, z, t) = 0 \\ &\Rightarrow\ \phi^{\leftrightarrow}_{\lambda_1,stat}(r, z)\Big[\sigma^{\lambda_1}_{A\to B}\ C_A(r, z, t) - \sigma^{\lambda_1}_{B\to A}\ C_B(r, z, t)\Big] \\ &= \phi^{\leftrightarrow}_{\lambda_2,stat}(r, z)\Big[\sigma^{\lambda_2}_{B\to A}\ C_B(r, z) - \sigma^{\lambda_2}_{A\to B}\ C_A(r, z, t)\Big] \end{aligned} \tag{3.9}$$

with the omnidirectional fluxes $\phi^{\leftrightarrow}_{\lambda,stat}(r, z)$ at both the wavelengths. A homogeneous concentration of photochromic molecules over the AML thickness is assumed, such that $C_{A,stat}(r, z) = C_{A,stat}(r)$ and $C_{B,stat}(r, z) = C_{B,stat}(r)$. If the ratio of the photochromic molecules in state B exists with a ratio β, $(0 < \beta < 1)$, then at the radial position r_{AML}, the concentration of molecules in state A and state B can be written as:

$$\begin{aligned} C_{B,stat}(r_{AML}) &= \beta \cdot C_{tot} \\ C_{A,stat}(r_{AML}) &= (1-\beta) \cdot C_{tot} \end{aligned} \tag{3.10}$$

For simplification, the contribution from parasitic absorption is neglected. Therefore, eq.(3.9) is simplified to:

$$\frac{\phi^{\leftrightarrow}_{\lambda_2,stat}(r_{AML})}{\phi^{\leftrightarrow}_{\lambda_1,stat}(r_{AML})} = \frac{1-\beta}{\beta} \frac{\sigma^{\lambda_1}_{A\to B}}{\sigma^{\lambda_2}_{B\to A}} \tag{3.11}$$

Since it is difficult to experimentally determine the omnidirectional fluxes $\phi^{\leftrightarrow}_{\lambda,stat}(r,z)$, the efficacy ξ is introduced. It relates the ratio of the incident photon fluxes ($\phi_{\lambda,in}$) into the AML to the omnidirectional fluxes and concentrations ratio.

$$\xi \frac{\phi_{\lambda_2,in}(r_{AML})}{\phi_{\lambda_1,in}(r_{AML})} \approx \frac{\phi^{\leftrightarrow}_{\lambda_2,stat}(r_{AML})}{\phi^{\leftrightarrow}_{\lambda_1,stat}(r_{AML})} = \frac{1-\beta}{\beta} \frac{\sigma^{\lambda_1}_{A\to B}}{\sigma^{\lambda_2}_{B\to A}} \tag{3.12}$$

Both the incident PSFs, measurement and confinement, are overlapped such that the maximum of measurement PSF is superimposed with the central zero minimum of the confinement PSF (at $r = 0$). However, to calculate the effective PSF, we are just interested in the vicinity of the minimum of the doughnut-shaped confinement PSF (small r). Hence, parabolic approximations of the illuminated PSFs are employed. The equations for the parabolic approximation of the photon flux for both axially symmetric PSFs at $r = 0$ are:

$$\begin{aligned} \phi_{\lambda_1,in}(r) &\approx \frac{\lambda_1}{hc} \frac{4}{\pi} \frac{P_1}{W_1^2} \left(\frac{r}{W_1}\right)^2 \\ \phi_{\lambda_2,in}(r) &\approx \frac{\lambda_2}{hc} \frac{2}{\pi} \frac{P_2}{W_2^2} \left[1 - 2\left(\frac{r}{W_2}\right)^2\right] \end{aligned} \tag{3.13}$$

Using the above equations in eq.(3.12) we get:

$$\frac{\phi_{\lambda_2,in}(r_{AML})}{\phi_{\lambda_1,in}(r_{AML})} \approx \frac{\lambda_2}{\lambda_1} \frac{\frac{2}{\pi} \frac{P_2}{W_2^2} \left[1 - 2\left(\frac{r_{AML}}{W_2}\right)^2\right]}{\frac{4}{\pi} \frac{P_1}{W_1^2} \left(\frac{r_{AML}}{W_1}\right)^2} \approx \frac{1}{\xi} \frac{1-\beta}{\beta} \frac{\sigma^{\lambda_1}_{A\to B}}{\sigma^{\lambda_2}_{B\to A}} \tag{3.14}$$

Hence, solving the above equation for $2r_{AML}$ and using eq.(3.8) we get:

$$\Delta x_{AMI} \approx 2r_{AML} \approx \frac{\sqrt{2}W_2}{\sqrt{1 + \frac{1}{\xi}\frac{1-\beta}{\beta}\frac{\sigma^{\lambda_1}_{A\to B}}{\sigma^{\lambda_2}_{B\to A}}\frac{\lambda_1}{\lambda_2}\frac{W_2^4}{W_1^4}\,PR}} \tag{3.15}$$

where, PR is the power ratio of the confinement and measurement beam powers, $PR = \frac{P_1}{P_2}$. PR is a decisive quantity that impacts the resolution enhancement [3, 10, 11, 61–64]. The ratio of the FWHM of the effective PSF, Δx_{AMI}, and the diffraction-limited PSF, Δx, is defined as the lateral resolution enhancement factor, κ:

$$\kappa = \frac{\Delta x_{AMI}}{\Delta x} \tag{3.16}$$

Analogous to the resolution enhancement is STED microscopy (eq.(2.25)), the lateral resolution enhancement factor, κ can be expressed as:

$$\kappa = \frac{\Delta x_{AMI}}{\Delta x} \approx \frac{1}{\sqrt{1 + \frac{PR}{PR_{sat}}}} \tag{3.17}$$

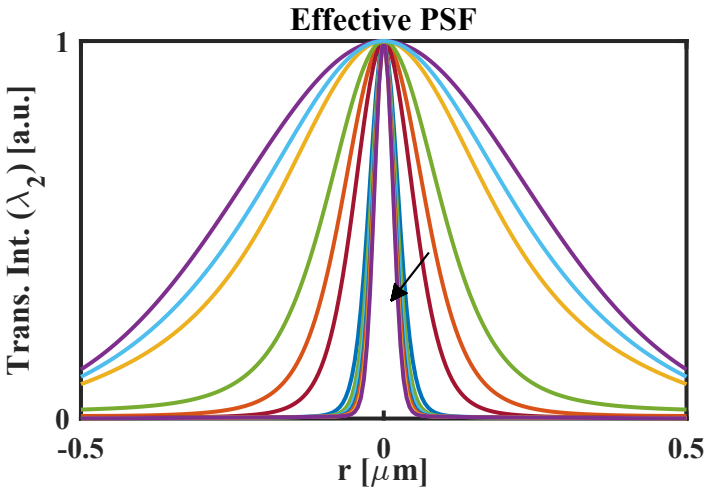

Figure 3.7: The spatial distribution of the transmitted intensity of the measurement beam through the aperture using the Lambert-Beer law. The arrow indicated the increasing time of illumination. Estimated FWHM of the effective PSF after 50 ms of illumination is 60 nm. The illumination times shown in the figure are: 10 µs, 50 µs, 100 µs, 500 µs, 1 ms, 2 ms, 10 ms, 15 ms, 20 ms, 25 ms, 30 ms, 40 ms and 50 ms

Using the data from the simulations shown in Fig. 3.3 and 3.6, we estimated the profile of the effective PSF generated in an AML of a thickness of 200 nm. However, instead of using a beam propagation model, as done by Kowarsch *et al.*, we computed the spatial transmitted intensity through the AML using the Lambert-Beer law. The reflection from the surface of the substrate was also incorporated such that the effective thickness of the AML was twice its original thickness. Fig. 3.7 shows

the effective PSFs at various illumination times. At the photostationary state, the computed FWHM is $\approx 60\,\mathrm{nm}$. At the length scale of the sub-wavelength aperture size and the thickness of the AML, the effect of diffraction is substantial. Since we do not consider any diffraction losses of the measurement beam at the AML aperture, the estimated effective PSFs in Fig. 3.7 are likely overestimated, predicting tighter PSF confinements.

Chapter 4

Experimental Implementation of AMI in a Confocal Reflection Microscope

In the presented work, we developed a confocal reflection microscope[1] to demonstrate AMI in reflection experimentally. Fig. 4.1 shows the schematic of the microscope. It is mainly divided into three units: the Measurement Unit (MU), the Confinement Unit (CU), and the Imaging Unit (IU). As discussed in the previous chapter, AMI requires two lasers: the measurement and the confinement laser. The individual units of the confocal microscope, MU and CU, contain optics to control and modulate the measurement and confinement lasers, respectively, for AMI. The optics required to combine the two lasers to illuminate the sample and detect its reflected signal are incorporated in the IU. An additional WF microscope is also incorporated in the setup.

Following the original design of a confocal microscope [13], described in chapter 2, the sample is placed on a 3-D piezo stage (NanoMax, 3-Axis $NanoMax^{TM}$ Flexure Stage, *Thorlabs, Dachau, Munich, Germany*). However, instead of using a refractive lens, generally used in imaging systems, a four spider-legged Schwarzschild objective (SO, 52x, NA = 0.65, BOS 5004-000-D, *Mountain Photonics GmbH, Landsberg am Lech, Germany*) is used for focusing the laser beams on the sample. The beam diameter is adjusted using appropriate telescopes such that the entrance pupil of the objective is fully illuminated. Additionally, half-wave-plates (HWP) and quarter-wave-plates (QWP) are used in the CU and MU in order to control the polarisation state of the respective laser beams. Other parameters for e.g., laser power and illumination time, movement of the stage and data acquisition, are coordinated electronically via a National Instruments Data Acquisition (NIDAQ) card (PCIe-7856R, National Instruments, *Austin, TX, USA*) in combination with the acquisition software Imspector (Abberior Instruments GmbH, *Göttingen, Germany*). In the following sections, each unit of the setup and some individual optical components are explained in detail.

[1] In this thesis, from this chapter on, the terms confocal reflection microscope, reflection microscope and confocal microscope are used synonymously.

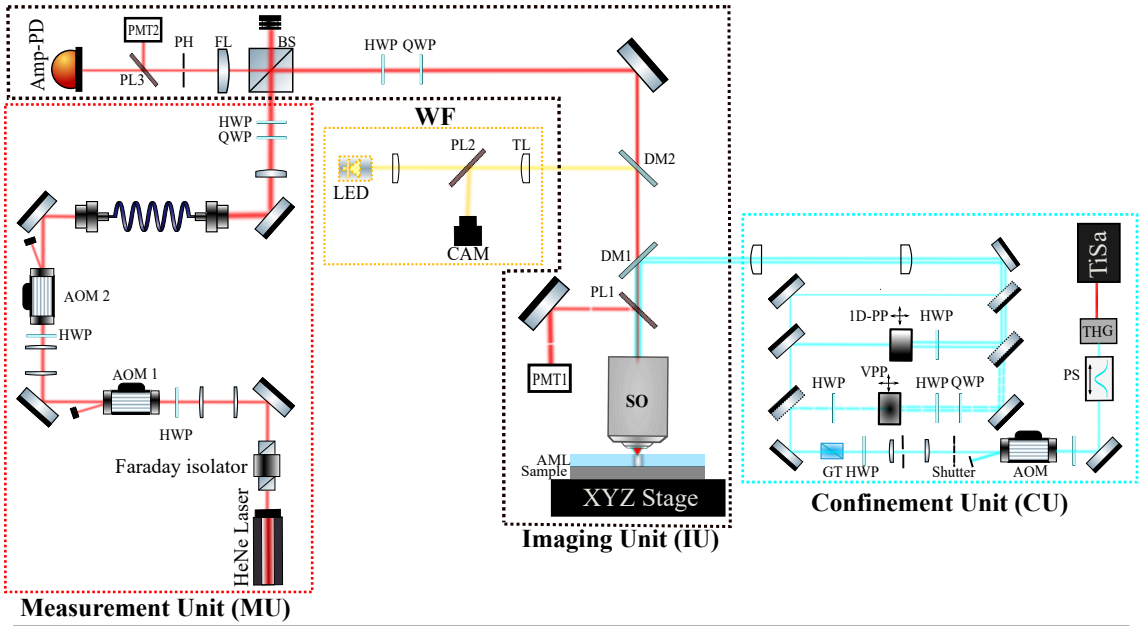

1D-PP: 1D Phase Plate	FL: Focusing lens	PS: Pulse Stretcher
Amp-PD: Amplified Photodiode	GT: Glan-Taylor polariser	SO: Schwarzschild Objective
AOM: Acousto Optic Modulator	HWP/QWP: Half/Quarter waveplate	THG: Third Harmonic Generator
BS: Beamsplitter	PH: Pinhole	TiSa: Titanium Sapphire Laser
CAM: Camera	PL: Pellicle	TL: Tubelens
DM: Dichroic mirror	PMT: Photomultiplier Tube	VPP: Vortex Phase Plate

Figure 4.1: High-resolution confocal reflection microscope. The WF microscope (yellow box) is used for overviewing the sample under investigation. The confocal setup combines the measurement unit (MU), confinement unit (CU), and the imaging unit (IU). The MU (red box) and CU (cyan box) contain optics to modulate properties of 633 nm laser (λ_2) and 325 nm (λ_1) laser, respectively, for optimal imaging. The laser beams are combined using dichroic mirror a (DM1) and a BS and focused on the AML-coated sample through the SO (52x, NA = 0.65) in the IU.The co-illumination of λ_1 and λ_2, modulates the AML and generates an aperture within the AML. The reflected signal from the sample at λ_2 through the generated aperture is collected through the same objective, and is focused using a focusing lens (FL) onto a detection pinhole. The light passing the pinhole is detected on a photo-receiver (Amp-PD). The sample and the pinhole are in conjugated planes to eliminate out-of-focus signal.

4.1 WF Microscope

The WF microscope built in this setup is used to acquire overview images of the sample under investigation. It assists in finding the micro-structures on the sample used for high-resolution imaging. The yellow box in Fig. 4.1 shows the schematic of the WF microscope. A broadband LED (470-850 nm, MBB1L3, *Thorlabs, Dachau, Munich, Germany*) is used as the light source. The beam is collimated and coupled into the IU by using dichroic mirror (DM2). Only a selected portion of the spectrum ($\geq$ 775 nm) is reflected by DM2 on the sample because the AML coated on the sample is affected by the wavelengths below 750 nm. The tube lens (TL) and the objective provide a wide field illumination on the sample. The reflected signal from the sample is collected and reflected on the detector by the pellicle (PL2, BP145B2, *Thorlabs, Dachau, Munich, Germany*). The detector used for WF imaging is a charge-coupled device (CCD) camera (Sony ICX694, *Point Grey Research*).

4.2 Confocal Microscope

The confocal microscope consists of three units. Each unit contains optics to modify the laser beams required for achieving high-resolution imaging. In the following paragraphs, each unit is described in detail.

4.2.1 The Measurement Unit

A vertically polarised, continuous wave helium-neon (He-Ne) laser source (633 nm, 21 mW, HNL210LB, *Thorlabs, Dachau, Munich, Germany*) is used as the measurement laser (see Fig. (3.2)). In order to prevent any back-reflections into the laser system a Faraday-isolator (IO-3-633-LP, *Thorlabs, Dachau, Munich, Germany*) is placed immediately after the laser. As mentioned before, a confocal microscope uses point illumination and the sample is scanned pixel by pixel to generate an image. Acousto-optic modulators (AOM, AA.MT110-1.5−VIS *Opto Electronic, France*) are installed in the measurement beam pathway as their ability for fast switching allows on- and off-switching of the laser beam as well as control the light intensity on each pixel. The extinction ratio of the AOM used in the setup is $10^4 : 1$; however, for the required range of intensities (mW to nW), this extinction ratio is not enough; hence, we have used two AOMs sequentially (AOM1 and AOM2 in Fig. 4.1). Using two AOMs ensures that no residual intensity of the measurement beam reaches the sample plane. A voltage range of $0 - 5$ V, required by the AOMs for intensity modulation, is provided by the NIDAQ card. The efficiency of the AOM, which corresponds to the maximum achievable laser power after the AOM, depends on the beam size and its polarisation [65]. Therefore, appropriate telescopes and waveplates are placed before the AOMs to achieve maximum efficiency.

The measurement beam is then coupled into the IU using a polarisation-maintaining single-mode fibre (P1-630PM-FC-2, *Thorlabs, Dachau, Munich, Germany*). Using a lens of focal length 20 mm at the output of the fibre, the beam is collimated to a spot size of 5 mm to ensure that the entrance pupil of the objective is completely illuminated. A pair of HWP and QWP is placed after the lens to optimise the required polarisation state before it is coupled into the IU.

4.2.2 The Confinement Unit

According to the absorption curve of BTE-1, shown in Fig. 3.2, light of wavelength 325 nm is needed to switch the AML to opaque state. A mode-locked ultrashort pulsed laser, Titanium-Sapphire laser (TiSa, *Chameleon Ultra II, Coherent Inc., Santa Clara, Ca, USA*) that delivers pulses with a temporal pulse length of 140 fs at a wavelength of 975 nm with a repetition rate of 80 MHz is used as a pump source to generate laser beam 325 nm via nonlinear frequency conversion. For this, a Third Harmonic Generator (THG, HarmoniXX THG, *APE Angewandte Physik & Elektronik GmbH, Berlin, Germany*), optimised for frequency tripling at the fundamental wavelength of 975 nm is used to generate a laser beam of 325 nm. Since the temporal pulse length of the generated 325 nm pulses is too short (140 fs) for an effective absorption within the AML; the pulses are stretched using a self-built pulse stretcher [66].

A laser pulse comprises of many frequency components, that propagate at different speeds inside a dispersive medium. As a result, a laser pulse propagating through a dispersive medium experiences a temporal delay between the frequency components, resulting in the temporal stretching of the pulse. Consequently, pulse stretching can be realised by introducing an appropriate amount of dispersion to the pulses. Various techniques are available for pulse stretching; however, grating pairs can achieve higher effective dispersion values in compact space. Therefore in our setup, two custom-designed transmission gratings (*Ibsen Photonics, Denmark*), with a grating resolution of 3076.9 ln/mm, are used to build a pulse stretcher. The gratings are installed on a multi-axis stage (TTR001, *Thorlabs, Dachau, Munich, Germany*) that can provide tip, tilt and rotation adjustments. A retro-reflector (HRS1015-F01, *Thorlabs, Dachau, Munich, Germany*) placed after the gratings spatially separates the input and output pulses and redirects them back into the gratings, thus introducing two-fold dispersion. A temporal pulse length of approximately 10 ps is achieved with the grating grating-pair based pulse stretcher.

To modulate the intensity of 325 nm laser pulses, an AOM (I-M110-3C10BB-3-GH27, *EQ Photonics GmbH, Eching, Germany*) is used. The voltage range required for modulation is between 0 -1V, provided by the NIDAQ card. A fast shutter (Uniblitz LS6 series, *Rochester, NY*) is placed after the AOM to block any residual laser

intensity from the AOM. Thus, the on- off- switching of the confinement beam is governed by the maximum frequency of the shutter, which is 150 Hz.

After the shutter, the laser beam is spatially filtered using a pinhole to get a clean Gaussian beam. A combination of a Glan- Taylor (GT) polariser and a HWP is used to purify the linear polarisation of the beam before any beam modulation optics. This combination also helps in further modulating the laser power. Hereafter, the beam is diverted into three different beam paths using magnetic mirror mounts (KB1X1, *Thorlabs, Dachau, Munich, Germany*), as shown in the cyan box in Fig. 4.1. Each beam path modulates the beam distinctively so that different confinement foci are generated in the focal plane. The three possible confinement foci are (top to bottom): Gaussian intensity distribution, one-dimensional confinement (1D doughnut) or two-dimensional confinement (2D doughnut).

Beam modulation refers to imprinting a suitable spatial phase distribution onto the wavefront to produce the required intensity pattern, when focused. Various alternatives are used in different STED setups for modulating the beam [67, 68]. In this setup, the suitable phase distribution is imprinted onto the beam by a 1D phase plate (1D-PP, BHalle, Bernhard Halle Nachfl. GmbH, *Berlin, Germany*), designed explicitly for a wavelength of 325 nm. 1D-PP is a half-coated glass plate made of fused silica such that an optical phase of $0 - \pi$ is imprinted on the beam. Half of the beam acquires a phase of π, which results in a destructive interference with the other half of the beam along the optical axis. This results in a 1-D pattern with a line-shaped zero intensity, in other words, confinement along in one axis in the focal plane. Experimental and vectorial simulations have shown that minimum zero intensity in the focal plane is achieved when the polarisation of the incoming beam is perpendicular to the 1-D phase step [49, 52, 69]. The polarisation is tuned using a HWP before the beam goes through the 1D-PP.

The 2D-doughnut pattern is generated by placing a vortex phase plate (VPP, Viavi Solutions (RPC Photonics, Inc.), *Rochester, New York*) into the Gaussian beampath. VPP is etched in fused silica with a locally varying thickness such that a variable phase of $0 - 2\pi$, also known as helical phase ramp, is imprinted onto a linearly polarised beam. The phase is acquired in such a manner that each ray in the beam has a $\pi-$ shifted counterpart that interferes destructively along the optical axis in the focal plane[2]. This results in a doughnut-shaped intensity distribution, confinement in 2D, with a zero centre in the focal plane. The best results are obtained when the beam is circularly polarised, hence, a QWP is used after the VPP to achieve circular polarisation and an optimised doughnut-shaped focus in the focal

[2]This is true for paraxial conditions. For high NA objectives, an axial field (z-field) is generated due to radial component of the incoming beam and a null centre is not achieved. To balance this residual z-field, the beam is circularly polarised before it interferes in the focal plane [52].

plane [50].
The beam path for a Gaussian intensity distribution of confinement beam in the focal plane contains a pair of HWP and QWP. This combination of waveplates allows us to access all the possible polarisation states to match the polarisation of the measurement beam during experiments. After phase modulation, the three beam paths of the confinement beam are combined, and through a telescope, they are coupled into the IU via DM1. Only one of the beams, Gaussian, 1-D pattern and doughnut, can be accessed at a time.

4.2.3 The Imaging Unit

The IU includes the illumination and the detection elements. Here, the confinement and measurement lasers modulated in the CU and MU, respectively, are overlapped and focused by the objective on the sample. The measurement beam from the MU is coupled in to the IU using a 10:90 beamsplitter (BS) such that the reflected beam is used for illumination. Using a 10:90 BS reduces the illumination power; however, its primary purpose is to maximise the collected signal during measurements on the detector. The power of the reflected beam is highly dependent on the polarisation of the beam. Therefore, a pair of HWP and QWP is placed before the BS to maximise its reflected power. Another pair of HWP and QWP is placed after the BS to control the polarisation of the beam on the sample plane, as it is a crucial property that affects the imaging technique. The modulated confinement beam and WF microscope are coupled into this unit via DM1 and DM2, respectively.
The lasers used for AMI are from two different spectrums, UV and visible; therefore, a SO is used in the setup to eliminate chromatic aberrations due to the significant difference in the spectrum. The sample is placed on the NanoMax stage, integrated with stepper motor actuators for large travel distance and coarse adjustment, and closed-loop piezo for scanning and fine adjustments. The stepper motor actuators provide a travel range of 4 mm along the X, Y and Z axis with a resolution of 0.5 µm. The piezo provides a travel range of 20 µm with a finer resolution of 5 nm. The NIDAQ card provides the driving voltages for the piezo and stepper motors via Imspector. The stepper motors are controlled using the APT user software provided by Thorlabs.
There are three detectors in the IU, two analog photo-multiplier tubes (PMT1 and PMT2, H10722-20, Hamamatsu Photonics Europe GmbH, *Herrsching Germany*) and fibre coupled amplified photo-diode (Amp-PD, also known as photoreceiver, OE-200-SI-FC, FEMTO Messtechnik GmbH, *Berlin, Germany*). PMTs can measure photons in a broad spectral range (230 nm - 920 nm) and are equipped with low-noise amplifiers with variable gain that convert the PMTs' current output to a voltage output. An external power supply (C10709, Hamamatsu Photonics Europe

GmbH, *Herrsching Germany*) is connected to each PMT to provide both the driving voltage of 5 V to run the PMT and the control voltage or gain voltage, 0 - 1 V. The pellicles, PL1 and PL3, are placed on removable magnetic base between the objective and DM1, and after the pinhole, respectively. PL1 and PL3 partially reflect the reflected signal from the sample onto PMT1 and PMT2, respectively. Except for high-resolution imaging, the PMTs are used for detection in all the other measurements.
The Amp-PD is a Si-PIN detector with a low noise trans-impedance amplifier with variable gain and bandwidths. It is connected to a power supply of 15 V and can measure in a broad spectral range of 320 nm-1060 nm. The Amp-PD is used for confocal detection as it has a high gain conversion factor and adds minimal noise to the signal. For high-resolution confocal detection, the pellicle (PL1) is removed, and the reflected signal is transmitted through the beamsplitter (90% transmission) to the Amp-PD. Using a focusing lens (FL) of 160 mm, the reflected signal is focused and coupled into the fibre coupled Amp-PD. The core diameter of the fibre effectively behaves as a confocal pinhole with a diameter of $\approx$ 1AU. The scanning and detection are synchronized via Imspector.

The confocal reflection microscope described in this chapter is implemented for high-resolution imaging via absorbance modulation. The series of experiments performed using the microscope, and their results are discussed in the next chapter.

Chapter 5

Experimental Results and Discussion

The first experimental results of the effect of absorbance modulation on confocal reflection imaging are presented in this chapter. We first characterise the AML coated on the samples. We then use the results from the characterisation of the AML to design experiments for high-resolution imaging. The optical setup, confocal reflection microscope, discussed in the previous chapter, is utilised for the experiments discussed in the chapter.

Samples used in the experiments

Three different kinds of sample structures, a half-coated chromium mirror (referred to as mirror sample), a layer of 80 nm gold beads (GB sample) and a calibration grid structure, all on quartz substrates, are used in multiple experiments that will be discussed in the following sections. The BTE-1 molecules were synthesised and spin-coated, embedded in a polymethylmethacrylate (PMMA) matrix, as AML onto the substrates at the *IPC* and *IOC, TU-Clausthal*. As the scope of the thesis is restricted to the application of BTE-1 for high-resolution imaging, the synthesis of these molecules is not discussed here. The method of synthesising BTE-1 is described in detail by Andrew *et al.* [11].

The mirror sample is a quartz substrate that was half-coated with chromium at the *Precision Optics Workshop at MPI, Göttingen*. The sample was then spin-coated with an AML of thickness 400 nm.

To prepare the GB sample, a quartz substrate is first covered with a drop of 100 µL Poly-L-Lysine (PLL) solution (P8920, *Merck, Darmstadt, Germany*) and incubated for five minutes. In the meantime, a diluted colloidal solution of gold beads of 80 nm diameter (BBI solutions, *Freiburg, Germany*) is sonicated in an ultrasonic bath for five minutes. After the PLL is removed, 100 µL of the diluted colloidal solution is placed on the substrate. Some of the beads stick to the surface, and the rest of the solution is removed after 2-3 minutes. The GB sample is then coated with an AML of thickness 1200 nm.

The calibration sample (Supracon AG, *Jena, Germany*) is a standard sample used for calibration and resolution-check of high-resolution optical microscopy techniques. It consists of various grating structures etched in nanocrystalline silicon on a quartz substrate. Two calibration samples were coated with an AML, one with a thickness of 400 nm and the other with a thickness of 1200 nm. Fig. 5.1(left) shows an illustrative picture of an AML-coated calibration sample. A magnified image of the area marked with the red box is shown on the right. The image is taken using a reflected light microscope (Mikroskop Axio Imager.Z2m, *Carl Zeiss Microscopy Deutschland GmbH, Oberkochen, Deutschland*).
Another GB sample is prepared following the same steps as described above. However, it is prepared on a 200 µm quartz coverslip, and once the gold bead solution is removed, the coverslip is flipped over on a quartz substrate coated with mowiol. Mowiol acts as a glue that hardens, thus adhering the coverslip to the substrate. The refractive index of mowiol is comparable to the refractive index of the coverslip and the substrate. This alignment sample is used for the setup alignment, discussed in the next section.

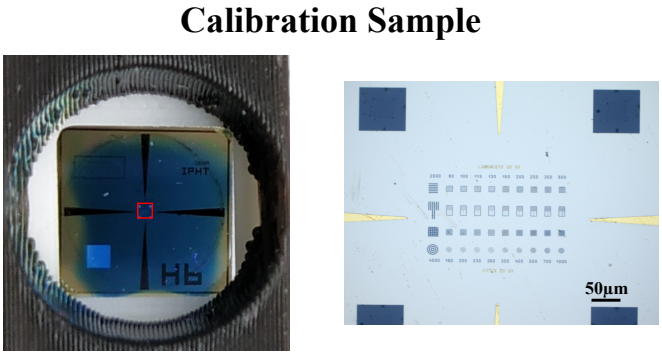

Figure 5.1: (left) An illustrative picture of an AML-coated calibration sample. (right) A magnified image of the centre of the sample, marked by a red box.

At present, the samples are not coated in a clean room, but instead under regular lab conditions. This introduces some impurities in the layer, e.g., dust particles, which introduces inhomogeneity in the layer. In order to produce an AML of greater thickness, the concentration of BTE-1 molecules and PMMA dissolved in the solvent (Anisole) is increased, while keeping the ratio of PMMA and concentration constant. This high concentration of BTE-1 makes it difficult to dissolve it in Anisole, resulting in some undissolved clusters of BTE-1 in the layer.

Alignment of the setup

The reflective objective, SO, used in the setup can be adapted for various coverslip thicknesses, in order to correct for aberrations. For AML characterisation and high-resolution imaging measurements, the SO is set at zero coverslip thickness. Once

the settings are adjusted, the lateral and angular position of the secondary mirror (see Fig. 5.2) is optimised using the adjustment screws of the objective. For this, a bright-field (BF) microscope (Motic B3 Series, *Motic Deutschland GmbH, Wetzlar, Germany*) and a silverpoint sample[1] provided by the manufacturers of the objective are used. Fig. 5.2(right,top) shows a BF-image of such a silverpoint sample for a misaligned objective. The point-like holes are visible as strongly distorted intensity distributions due to coma aberrations introduced by the wrong positioning of the secondary mirror. For a well-aligned objective, the image of the silverpoint sample shows spherical structures as shown in Fig. 5.2(right,bottom).

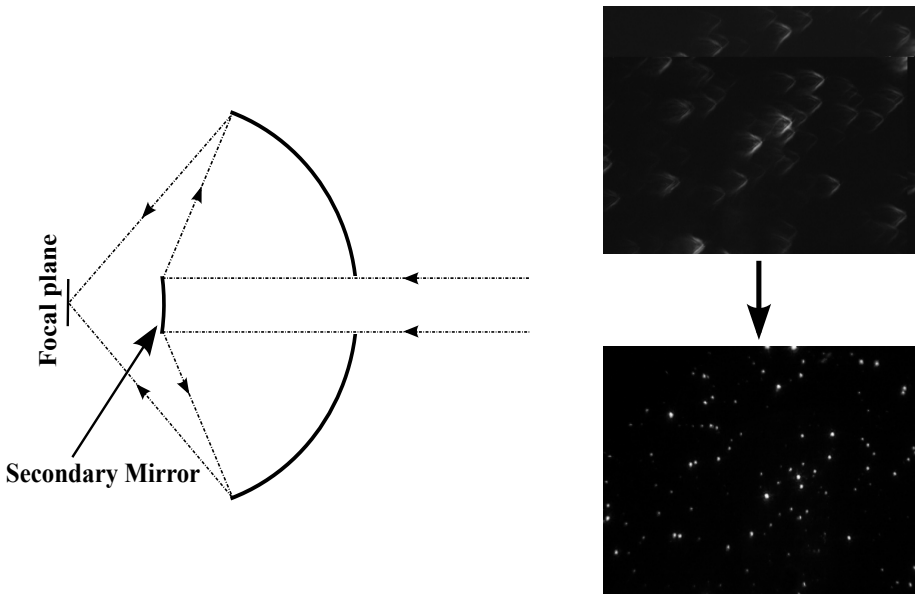

Figure 5.2: The figure shows the fundamental design of the SO (left). On the right, the top image shows the BF image through a misaligned SO. The bottom image shows the BF image through an aligned SO (modified from [70]).

With the aligned SO mounted in the confocal microscope, the NanoMax stage that is used for scanning the sample under investigation is calibrated using a standard grid sample (R1L1S1P, *Thorlabs, Dachau, Munich, Germany*). The maximum area that can be scanned is $15 \times 15\,\mu m^2$. For 2D scanning, the minimum pixel dwell time of the stage is limited to 10 ms with a minimum pixel size of 70 nm. At the same time, for 1D scanning, NanoMax can be used with a minimum pixel size of 30 nm. Before performing any measurements using the confocal microscope, it is aligned such that the focal spots of the confinement and measurement beam are superimposed. For this, the alignment sample containing gold beads of diameter 80 nm is consecutively scanned through the focus of the confinement (Gaussian or 1D-PP) and measurement beam and the back-reflected signal is imaged onto PMT1. Since

[1] A thin film of silver is coated on a microscopic slide. Holes of various sizes (0.5-5 µm) are then pricked in the layer to create point-like objects for imaging.

the gold beads are small compared to the size of the PSF, the measured intensity distribution gives a sufficiently well estimate of the PSF shape. The mirrors and lenses in the individual laser beam paths are used to overlap both PSFs laterally and axially, respectively. Fig. 5.3 shows a xy-section of measurement of three single gold beads. The displayed FOV is 5.60×3.60 µm^2. On the left, three gold beads measured with the confinement beam of wavelength 325 nm are shown, and on the right, the measurement beam of 633 nm wavelength is used to image the same beads. The 1D-pattern as well as the Gaussian shape are clearly visible.

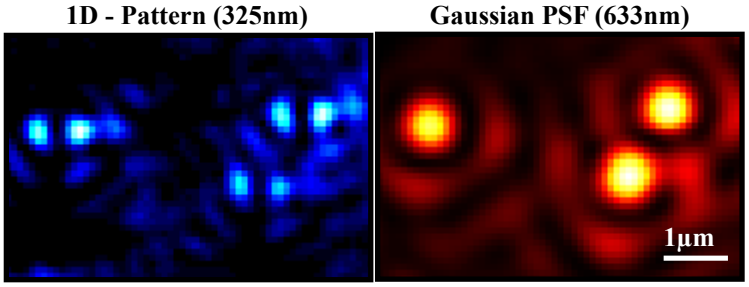

Figure 5.3: The figure shows a FOV of 5.60×3.60 µm^2 of the GB sample scanned consecutively through the confinement (left) and the measurement PSF (right).

5.1 Characterisation of the AML

The synthesis of BTE-1 molecules and estimation of various parameters, for e.g., absorption cross-section and quantum yield to characterise these molecules, were performed following the procedure stated in reference [11]. These measurements were carried out at the *IPC* and *IOC, TU-Clausthal*. A short overview of the calculations is provided in the following paragraphs.

To calculate the absorption cross-sections of the open and closed form of BTE-1 molecules, UV-VIS absorption spectra were measured using a spectrometer. A cuvette filled with a BTE-1/Anisole solution, of a known concentration of BTE-1, was used for the measurement. The absorption spectra provide the values of absorbance (A) at $\lambda_1 = 325$ nm and $\lambda_2 = 633$ nm. Then using the integrated form of the Lambert-Beer law, $A = \varepsilon \cdot l \cdot C$, where A is the absorbance, l is the optical path length and C is the known concentration of BTE-1 molecules, the absorption cross-sections ($\varepsilon_{A,B}^{\lambda_{1,2}}$) are derived.

As discussed in Chap. 3, for AMI in reflection microscopy, a channel is generated in the AML by modulating the absorbance of the layer. As stated above, the absorbance is directly proportional to the concentration of the BTE-1 molecules. Therefore, for our experiments, the initial concentration, C_0, of the BTE-1 molecules in the AML-coated samples is an important quantity. To determine C_0 for a 400 nm thick AML-coated substrate, we used the provided values of the UV-VIS absorp-

tion spectra of the AML layer and the absorption cross-sections ($\varepsilon_{A,B}^{\lambda_{1,2}}$) that were measured previously. Using the Lambert-Beer law and the given values of the absorbance, the layer thickness and the absorption cross-sections, we calculated $C_0 = 1157.65\text{mol}\,\text{m}^{-3}$. In comparison to the original value shown in table. 3.2, the initial concentration of the BTE molecules in the layer is significantly less.
In order to use the AML for high-resolution imaging, it is important to understand the temporal and behavioural response of the layer at various powers of the confinement and measurement beam. Therefore, before carrying out high-resolution imaging measurements, we first experimentally characterised the AML to determine its damage threshold, its temporal response to various powers of the illuminating beams of wavelength $\lambda_1 = 325\,\text{nm}$ and $\lambda_2 = 633\,\text{nm}$, and its fatigue resistance to evaluate favourable experimental conditions for AMI. For these experiments the mirror sample coated with an AML of thickness 400 nm is used. Both the beams, the confinement and measurement beam, are modulated to have circular polarisation and Gaussian focal spots. The measurement beam is also utilised as the monitoring beam at a very low power of 20 nW. The power of the monitoring beam is empirically chosen as the influence of the absorption of photons of λ_2 on the AML at such low power is insignificant. PMT1 and PMT2 are used for the detection of the reflected signal of the monitoring beam and measurement beam, respectively, from the mirror sample (see Fig. 4.1). To ensure detection only at the monitoring wavelength, a narrow bandpass filter (FL05635-10, *Thorlabs, Dachau, Munich, Germany*) is placed in front of PMT1 to block the signal at λ_1 and reduce noise, added due to ambient light.

5.1.1 Threshold of the AML

In this section, we will quantify the limit of powers of the confinement (P_{325}) and measurement (P_{633}) beam that can be illuminated on the AML without damaging or affecting its photochromic properties.
We will first evaluate the effect of the high power of the measurement laser on the AML. For this purpose, firstly, a 2D image of a selected region of the AML-coated mirror sample is acquired through the monitoring PSF. The selected region is then illuminated with a Gaussian focus of the confinement beam at power $P_{325} = 1\,\mu\text{W}$ for 100 ms, to switch the AML to its closed form, at a constant scan position. Following this, a 2D image of the manipulated sample is recorded using the monitoring beam. Thereafter, the switched-OFF sample region is illuminated with a high power of measurement beam with a Gaussian focus for 200 ms at the same scan position. This is followed by acquiring another 2D image of the same region with the monitoring beam. This measurement is repeated at various powers of the measurement beam, P_{633} while keeping the P_{325} constant, in different regions of the sample. Fig. 5.4 shows

the illumination sequence followed during the measurements and the 2D images of the sample regions that are recorded before and after they are irradiated with the confinement and measurement beam. It should be noted that the images shown in the figure have different colorbars. Each image is normalised to the maximum signal within the FOV. This is done to visually highlight the effect of the measurement beam on the AML.

Fig. 5.4 shows a schematic of the sequence of illumination of the confinement and measurement PSF on the top, after which the 2D images in the respective columns are recorded. Each row in the figure represents one measurement. In the first row of Fig. 5.4, the first 2D image shows the selected region of the sample. The high pixel values in the image suggest that the AML is in its open state such that it is transparent to the monitoring beam. This is followed by a 2D image of the area after it is illuminated with the confinement beam at power $P_{325} = 1\,\mu\text{W}$ for 100 ms. The image shows a dark spot, indicating absorption of the monitoring beam in that region. This implies that the AML is switched to its opaque state in the observed dark region. This region of the sample is then illuminated with the measurement beam with a Gaussian focus for 200 ms at power $P_{633} = 2\,\text{mW}$ which equals to an intensity of $52\,\text{kW}\,\text{cm}^{-2}$. Fig. 5.4(first row,right) shows the 2D image of the sample area, previously illuminated with the measurement beam. The bright region at the centre shows that the AML is switched back to its open state by the measurement beam. This measurement shows that the AML is switching as expected i.e., it switches to its opaque state when illuminated with the confinement beam and to its open state when illuminated with the measurement beam.

The same measurement was repeated using the measurement beam at power $P_{633} = 5\,\text{mW}$ (intensity of $130\,\text{kW}\,\text{cm}^{-2}$). The recorded 2D images of the second measurement are shown in Fig. 5.4(second row). As before, a dark region is observed in the 2D image of the sample area after it is illuminated with the confinement beam. However, at the centre of the image of same area after slight exposure with the measurement beam, a small region with lower intensity is observed, indicating absorption of the monitoring beam (see Fig. 5.4(second row,right)). This strange behaviour of the AML suggests that the AML is either degraded or damaged in the opaque region. Degradation in a photochromic system can occur due to the parasitic side reactions, which produce by-products, also called degraded or inactive molecules. These molecules have their own absorption spectra thus, they can absorb the illuminated light but might not switch between the two states [56, 60, 71, 72].

We continued with the same measurement using even higher power of the measurement beam to verify if the degradation observed in Fig. 5.4(second row,right) persists. For this, the measurement beam at power $P_{633} = 8\,\text{mW}$, which equals to an intensity of $240\,\text{kW}\,\text{cm}^{-2}$, is illuminated on the sample for 200 ms. The 2D im-

age of the illuminated area with the measurement beam is shown in Fig. 5.4(third row,right). An evident opaque spot at the centre of the illuminated area is seen, indicating an increased degradation or damage of the AML. These measurements show that the high laser intensities of the measurement beam ($\geq$ 130 kW cm^{-2}) either switches the photochromic molecules to an entirely different state with a distinct absorption band or that the AML is damaged.

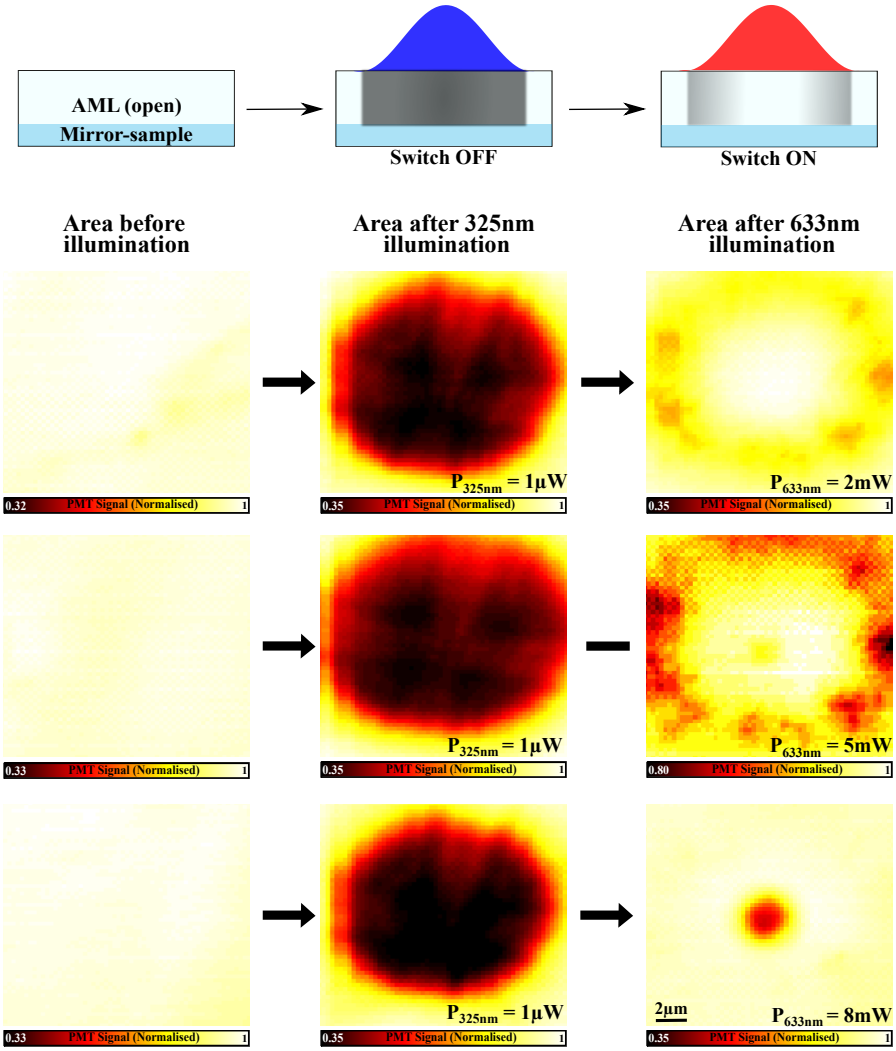

Figure 5.4: (top) The schematic shows the illumination sequence followed in each measurement, shown in the following rows. Each row represents one complete measurement. In each row, first the 2D image of the selected area of the AML in its open state is shown. Then the 2D image of the area of the AML after the illumination with Gaussian shaped foci, first with the confinement beam at power P_{325} = 1 µW for 100 ms (middle) and then with the measurement beam (right) for 200 ms at various powers (first row,right) P_{633} = 2 mW, (second row,right) P_{633} = 5 mW, and (third row,right) P_{633} = 8 mW. The shown signal is proportional to the intensity of the monitoring beam (at λ_2), which is back-reflected from the sample, and is thus a good indicator for the AML transmittance at this wavelength. At 2 mW, the AML switches back to its open form; however, at 5 mW and 8 mW, we see an opaque spot at the centre of the illuminated area. The colorbar for each image is adjusted to highlight the effect of the measurement beam visually.

A similar set of measurements is repeated to investigate the effect of the high powers

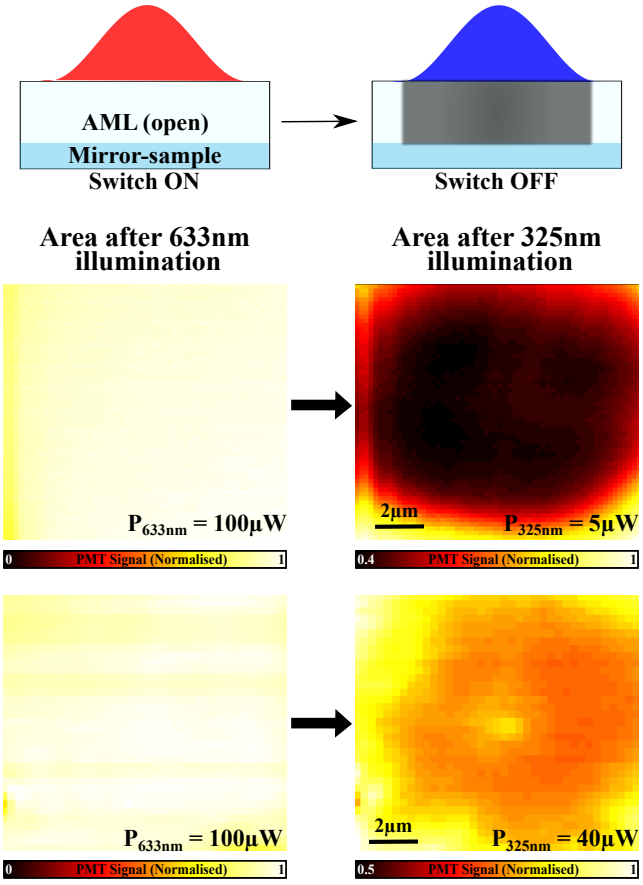

Figure 5.5: (top) The schematic shows the illumination scheme during one measurement. The figure shows 2D images of the area of the AML after illumination with Gaussian shaped focus of the measurement beam at power $P_{633} = 100\,\mu W$ for 200 ms (left column) and then with the confinement beam at power $P_{325} = 5\,\mu W$ and $40\,\mu W$ for 200 ms (right column). At $P_{325} = 5\,\mu W$ the AML switches as expected, however, at $P_{325} = 40\,\mu W$, instead of an entire dark region, a bright spot is observed at the centre of the illuminated region due to parasitic absorption of the light at wavelength λ_1. The colorbar for each image is adjusted to highlight the effect of the measurement beam visually.

of confinement beam on the AML. For this, the AML-coated mirror sample is first illuminated with the Gaussian-shaped focus of the measurement beam at power $P_{633} = 100\,\mu W$ for 200 ms. To ensure that the AML is in its open state, we acquire a 2D image of the illuminated area using the monitoring beam, as done in the previous measurements. This is followed by illumination with the confinement beam for 200 ms at various powers P_{325} and a 2D scan of the illuminated area to see the effect of the confinement beam on the AML. Fig. 5.5(top) shows a schematic of the illumination sequence during the measurement and the 2D images of the AML scanned after the illumination with the measurement beam at $P_{633} = 100\,\mu W$ (left) and the confinement beam at $P_{325} = 5\,\mu W$ and $40\,\mu W$ (right).

At lower powers of the confinement beam, the AML is switched to the closed state and an opaque region is observed. An exemplary measurement is shown in Fig. 5.5(first row,right) at $P_{325} = 5\,\mu W$. However, the same measurement at higher

power of the confinement beam $P_{325} = 40\,\mu W$, which is an intensity of $3\,kW\,cm^{-2}$, shown in Fig. 5.5(second row,right), we see a different behaviour. Instead of a complete opaque region, a bright spot at the centre of the area is observed, after illumination with the confinement beam. This inconsistency can be due to the degraded molecules that are produced during the switching of the AML.
To sum up, irradiation with different powers of the confinement and the measurement beam on the AML of thickness 400 nm shows that power $P_{325} \geq 40\,\mu W$ and $P_{633} \geq 5\,mW$ can change the behaviour of the AML. Therefore, for future experiments, the powers of the confinement and measurement beam are always kept an order of magnitude lower than their threshold values to avoid any degradation in the layer.

5.1.2 Temporal Response of the AML

After the maximum laser powers up to which the switching of the AML into its transparent and its opaque state takes place without visible AML degradation have been experimentally determined in the previous section, we take a closer look at the temporal behaviour of a single switching cycle. Since during AMI image acquisition, the AML needs to be repeatedly switched between opaque and transparent for generating and erasing a suitable aperture at each pixel, the characteristic time constants for the switching strongly influence not only the pixel dwell time but also the overall image acquisition time. The switching times are thus important parameters for the design of the AMI experiment.

Switching the AML opaque (photo-colouration): We will first consider the UV-induced switching of the AML from transparent to opaque, which is also known as photo-colouration. As explained before, the AML turns opaque during continuous UV illumination, because the photochromic molecules in the AML switch from their open to their closed form, which means that the absorbance of the AML for the measurement wavelength increases. This continues until a photostationary state of the concentration of molecules in their closed and their open form is reached and hence the AML absorbance saturates.
Since it is difficult to measure the AML absorbance directly, we instead measure the AML transmittance. For this, the mirror sample, coated with 400 nm thick AML, is used. The confinement beam is irradiated on the AML-coated mirror sample, at a constant position, for 100 ms. The average laser power of the confinement beam is set to $P_{325} = 2\,\mu W$, which is approximately one order of magnitude below the threshold power derived in the previous section. For monitoring the AML transmittance during this time, the monitoring beam at a very low power of 20 nW is simultaneously

illuminated on the sample. PMT1 is used for detection of the reflected signal of the monitoring beam from the mirror (see Fig. 4.1).
Fig. 5.6, on top, shows a schematic of the measurement process to measure the transmittance of the monitoring beam during photo-colouration. Fig. 5.6(bottom,left) shows the temporal evolution of the detected back-reflected signal $S(t)$ of the monitoring beam (black stars). The data set is normalised to the signal S_0 at the start of the measurement at $t = 0$. It is clearly visible, that the detected signal, $S(t)$, decreases with increasing time. This curve is also referred to as the decay curve and shows the transition of BTE-1 molecules to the closed state.
From Fig. 5.6(bottom,left), it is apparent that the measured signal does not go to zero; instead, it saturates at a value of about 0.486. A constant background signal because of the reflection of monitoring beam at the air-AML interface, which is $\approx$ 4-5% of the incident power of the monitoring beam, and an additional $\approx$ 5% offset due to the ambient light contributes to this saturated value. We expect only $\approx$ 1.5% residual transmission through an opaque AML of thickness 400 nm with a concentration of $C_0 = 1157.65\,\mathrm{mol\,m^{-3}}$ of BTE-1 molecules. However, all the background contributions can only account for an offset of 0.12. Since the thickness of the AML is well measured, we suspect that the initial concentration of the BTE-1 molecules in the AML is overestimated such that the AML does not provide enough absorbance at the monitoring wavelength of 633 nm.
In order to understand the temporal behaviour of $S(t)$, we need to refer to the two non-linear coupled differential equations which describe the concentration change of the photochromic molecules as a function of time, lateral (r) and axial (z) position for a given irradiating photon flux density (see eq.(3.1) and (3.3)). Many simplified position-independent models have been derived in the past to gain further insight into this dynamic behaviour. Under the assumptions of a homogeneous AML with no parasitic absorption at wavelength λ_2, a constant photon flux density of the irradiated light of wavelength λ_1, independent of the radial and axial position, the detected signal is given by [73]:

$$S(t) = S_0 e^{-A_{\lambda_2}(t)} \tag{5.1}$$

where $A_{\lambda_2}(t)$ is the AML absorbance for the wavelength at λ_2 (see Chap. 3.3).
In a weak absorption limit [71, 73], $A_{\lambda_2}(t)$ can be modelled as a mono-exponential function of time. Hence, the measured signal can be described as:

$$S(t) = S_0 e^{-(e^{-k_a t})} \tag{5.2}$$

where $e^{-k_a t}$ is the mono-exponential variation of absorbance in time, with k_a as the rate of change of absorbance.

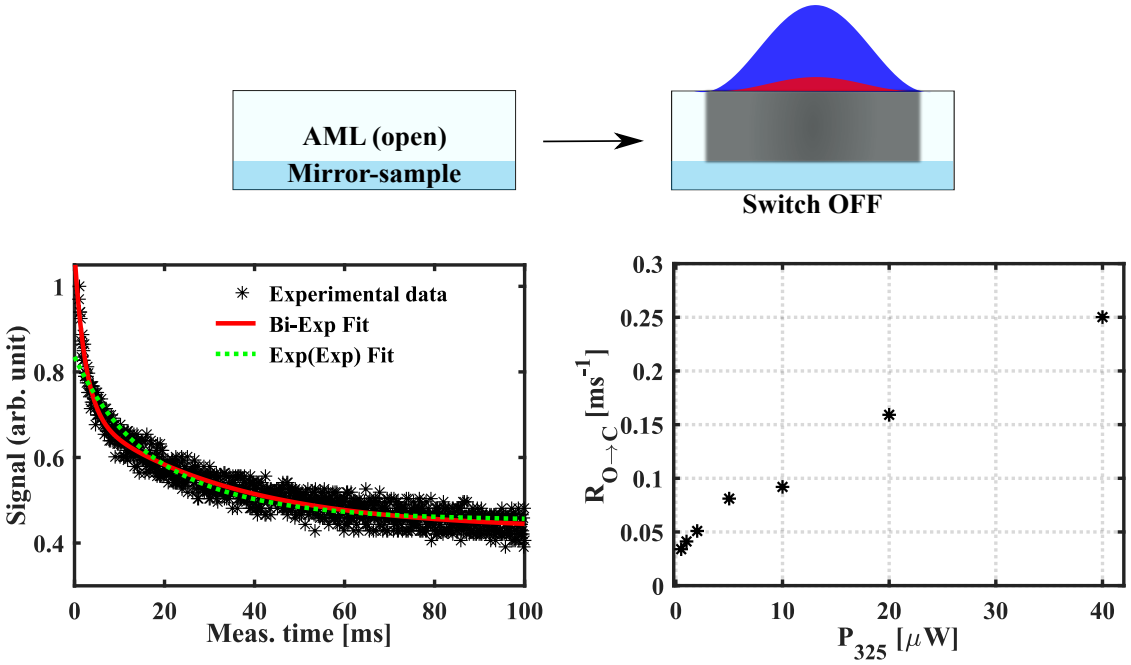

Figure 5.6: Temporal behaviour for switching the AML opaque. A schematic representation of the illumination scheme is shown on top. (left) The decay curve shows the temporal evolution of the detected back-reflected signal of the monitoring beam when the AML (in open state) is illuminated with the confinement beam at power $P_{325} = 2\,\mu W$. In addition to the experimental data points (black stars), a bi-exponential fit (red curve) and an fit according to eq.(5.2)(green curve) are plotted. (right) The conversion rates for switching the AML from its transparent to its opaque state are shown for various powers P_{325}.

However, the fit of the experimental data in Fig. 5.6(bottom,left) with a function of the form $e^{-a_1(1-e^{-k_a t})-a_0}$ (green curve, following eq.(5.2)) shows that the decay curve is only partially described by this. Instead, a bi-exponential function of the form: $a_1 e^{-k_1 t} + a_2 e^{-k_2 t} + c_0$ (red curve) describes the data much better. This might be due to the deviations from the approximations made for a mono-exponential behaviour of absorbance. Another reason for the better bi-exponential fit is due to the geometrical simplifications used for deriving eq.(5.2). The irradiated confinement and measurement beam have a Gaussian intensity distribution over the radial coordinate of the AML. Additionally, the photon flux also varies along the axial direction due to high absorbance of the AML. Therefore, the measured signal of the decay curve, plotted in Fig. 5.6(bottom,left), is an averaged signal over the radial and axial coordinate. Nonetheless, the data provides the basic information about the conversion rates of the AML. For further analysis, the conversion rate of the AML from transparent to opaque state, $R_{O\rightarrow C}$, is calculated by taking an amplitude weighted average of the rate constants obtained from the bi-exponential fit equation. Following the same measurement shown in Fig. 5.6, we measured the temporal evolution of the AML transmittance at various powers of the confinement beam at λ_1 ranging from $P_{325} = 0.5\,\mu W$ up to the limit power of $40\,\mu W$. The obtained conversion

rates of open form at varying laser powers is shown in Fig. 5.6(bottom,right). $R_{O\rightarrow C}$ increases linearly with the increasing power of the confinement beam.

For AMI measurements, it is reasonable to use powers of the confinement beam, which are at least one order of magnitude below the limit power $P_{325} = 40\,\mu W$, in order to avoid AML degradation. For this usable range of powers of a few µW, the conversion rates are of the order of $0.05\,ms^{-1}$ and below, which is equivalent to switching times of the order of 20 ms and longer.

Switching the AML transparent (fading process): In order to investigate the temporal behaviour of switching the AML from its opaque to its transparent state, also known as the fading process, measurements very similar to the ones described in the previous paragraph are performed. For this, we first illuminate the AML-coated mirror sample with the confinement beam at power $P_{325} = 1\,\mu W$ for 200 ms to switch the AML to its closed state and then illuminate with the measurement beam at power $P_{633} = 100\,\mu W$ for 200 ms, to switch the AML back to its open state. The power of the measurement beam is chosen such that it is at least one order of magnitude below the respective limit powers. The back-reflected signal of the measurement beam is detected by the PMT2. Fig. 5.7 shows a schematic of the measurement scheme on top. Fig. 5.7(bottom,left) shows an example of the temporal evolution of the detected back-reflected signal of the measurement beam, when the initially opaque AML is illuminated with light of the wavelength λ_2 with power P_{633}. The data is normalised to the signal at $t = 200\,ms$. The detected signal quickly increases due to the laser driven transition of the AML into its transparent state. Since this curve shows the recovery of the transparency of the AML, it is referred to as the recovery curve.

The rate equation for modelling the fading process is thoroughly derived by Pariani *et al.*, where a thin film of photochromic molecules in its opaque state is converted to transparent state by the means of VIS-light. For the case that the presumption of radially symmetric illumination, homogeneous concentration of photochromic molecules in the layer and no parasitic absorption at the VIS-wavelength (λ_2) holds true, a time-dependent absorbance (A_{λ_2}), averaged over the thickness of the layer can be derived as:

$$\langle A_{\lambda_2}(t)\rangle_z = \ln\left[1 + (e^{-\varepsilon_B^{\lambda_2} CD} - 1)\; e^{-R_{C\rightarrow O}t}\right] \tag{5.3}$$

where $\varepsilon_B^{\lambda_2}$ is the absorption cross section of the molecules in state B at λ_2, C is the total concentration of photochromic molecules in the layer, D is the total thickness of the layer and $R_{C\rightarrow O}$ is the rate constant for switching to transparent state. Together

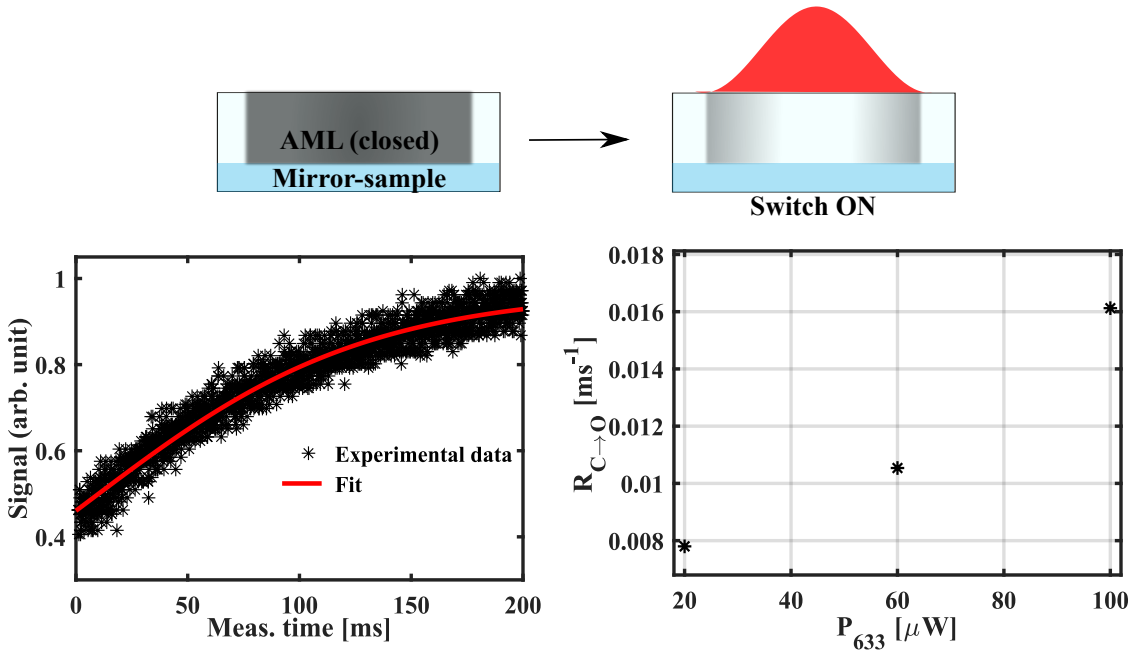

Figure 5.7: Temporal behaviour for switching the AML transparent. A schematic representation of the illumination scheme is shown on top. (left) The recovery curve shows the temporal evolution of the detected back-reflected signal of the measurement beam as a result of the change in absorbance of the AML (in closed state) when illuminated with the measurement beam at power $P_{633} = 100\,\mu\text{W}$. The experimental data is fitted using eq.(5.4) (red curve). (right) The conversion rates for switching the AML from its opaque to its transparent state are shown for selected powers P_{633}.

with eq.(5.1), this means that the transmitted signal of the light at λ_2 varies as:

$$\langle S(t)\rangle_z = \frac{1}{1+\left(\frac{1}{S_0}-1\right)e^{-R_{C\to O}t}} \tag{5.4}$$

where $S_0 = e^{-\varepsilon_B^{\lambda_2} CD}$ is the transmitted signal at $t = 0$.

Hence, the experimental data (black stars) in Fig. 5.7(bottom,left) is fitted using eq.(5.4) (red curve). Although the detected signal is averaged over the radial coordinate of the illuminated Gaussian focus of the measurement beam, the fit does not show any significant deviation from the rate equation and describes the temporal evolution of the signal well. Fig. 5.7(bottom,right) shows the conversion rates $R_{C\to O}$ for three selected powers P_{633}. It shows that for powers well below the limit power the conversion rates are of the same order of magnitude as the respective conversion rates for turning the AML opaque.

5.1.3 Fatigue Resistance

From the discussion in Chap. 3, it is apparent that the generation of the dynamic aperture in the AML is key to high-resolution imaging. For reflection microscopy,

this dynamic aperture is rastered over the measurement surface coated with the AML to form an image, which means the aperture is generated and erased at each scan position. For this, the BTE-1 molecules must undergo several switching cycles. The ability of a photochromic system to undergo numerous switching cycles without degradation is called fatigue resistance (Sect. 3.1), an essential property of photochromic molecules. It is a key parameter that limits the number of possible scan positions during imaging. The higher the number of cycles, the better the fatigue resistance, which should be as high as possible. Therefore, we analyse the maximum number of switching cycles the AML can sustain without degradation. The mirror sample, coated with 400 nm thick AML, is switched several hundred times between closed (OFF) and open (ON) states by sequential illumination with the confinement and measurement beam, respectively. The experimental settings are identical to those used for measuring the conversion rates of the AML in Sect. 5.1.2. PMT1 is used to measure the back-reflected signal of the monitoring beam (for decay curve) and PMT2 is used for detecting the back-reflected signal of the measurement beam (for the recovery curve).

The measurement procedure is schematically shown in Fig. 5.8(top). To ensure that the initial state of the AML is the open state, we first illuminate the mirror sample with λ_2 at 100 µW for 200 ms. For measuring the switching cycles, the AML is illuminated simultaneously with the confinement beam at power P_{325} and the monitoring beam for 200 ms, to switch the AML to its opaque state. While illuminating, the back-reflected signal of the monitoring beam is detected by PMT1 to acquire the decay curve. Subsequently, the sample is illuminated with the measurement beam at power P_{633} for 200 ms, to switch it back to the open state, and the back-reflected signal of the measurement beam is detected by PMT2 to obtain the recovery curve. This sequence of illumination and data acquisition is repeated 400 times. The complete measurement was repeated at different power combinations of the confinement and measurement beam.

Fig. 5.8 shows an example of such measurement. It shows the cyclic signal modulation of the back-reflected signal of the monitoring beam (decay curve) and the measurement beam (recovery curve). Here the laser powers used are $P_{325} = 1\,\mu W$ and $P_{633} = 1\,mW$. The inset in Fig. 5.8 shows the details of switching cycles 1-6 and 201-206. The grey and red dashed lines in Fig. 5.8 denote the full and half modulation depth of the detected signal. For the plots, the acquired data for the decay and recovery curves are smoothed and scaled using the maximum value of signal from the measured data sets.

Although the diarylethene family of photochromic molecules are known for their high fatigue resistance, a performance loss is often observed after a relatively low number of cycles [71, 72]. Here we observe that after about 200 cycles, the modulation

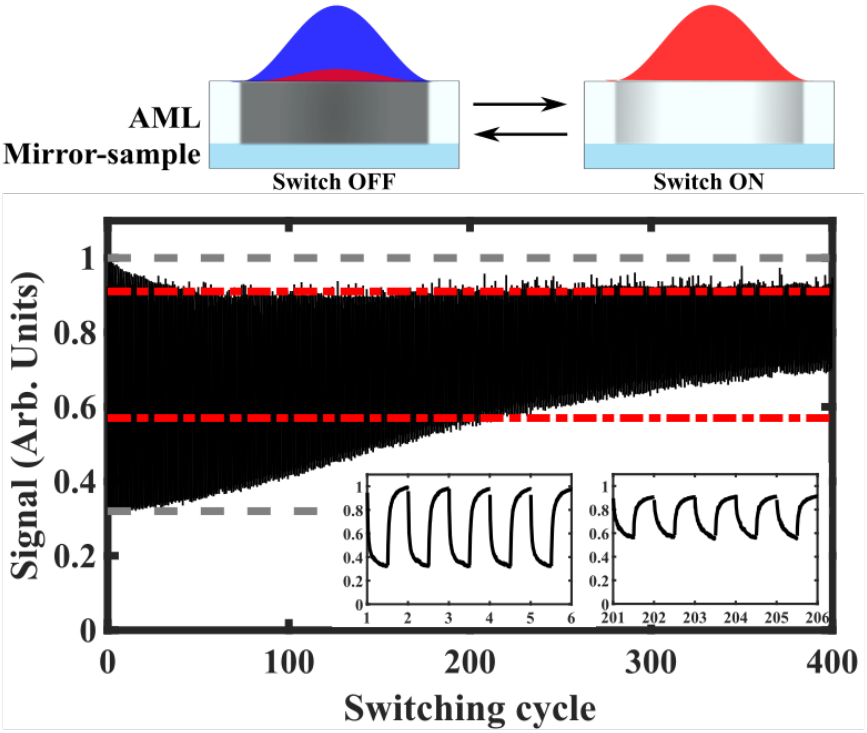

Figure 5.8: Switching cycles of the AML. A chromium mirror coated with a 400 nm thick AML sample is sequentially illuminated with Gaussian spots of the confinement beam of wavelength λ_1 and measurement beam of wavelength λ_2 at powers $P_{325} = 1\,\mu W$ and $P_{633} = 1\,mW$, respectively, for 200 ms. Monitoring beam at power of 20 nW is also simultaneously illuminated with the confinement beam to measure the change in transparency of the AML. The graph shows the normalised back-reflected signal of the monitoring beam (decay curve) and the measurement beam (recovery curve). Grey and red horizontal lines denote full and half modulation depth, respectively. Inset images: Details of switching cycles 1-6 and 201- 206.

depth drops to half of the initial value, denoted by the red dashed lines in Fig. 5.8, suggesting a degradation of the AML while maintaining the characteristic decay and recovery curve. The degradation is due to parasitic side reactions. As mentioned before, these side reactions produce one or more by-products that are undesirable; hence, they reduce the concentration of active molecules that switch between the two states with each cycle. The amount of degradation depend on the molecular structure of the photochromic molecules, experimental conditions and the irradiated photon flux. Several studies have investigated the degradation mechanism; however, there is no straightforward correlation between fatigue and the chemical structure of the molecules [60, 71, 72].

Another way to look at the degradation of the AML layer is to measure the change in modulation depth or contrast. We know from the previous measurements that the AML has a limited absorbance, which results in an offset value while measuring the decay curves. If S_{max} and S_{min} are the maximum (at $t = 0$) and minimum

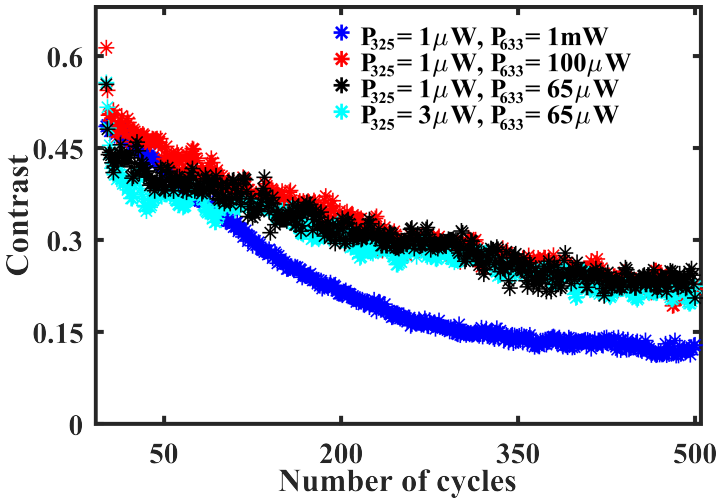

Figure 5.9: The figure compares the change in contrast, with increasing cycles, at various combinations of powers of λ_1 and λ_2.

(at t) detected signal in the decay curve, the contrast can be calculated using the equation:

$$Contrast = \frac{S_{max} - S_{min}}{S_{max} + S_{min}} \tag{5.5}$$

The measurement shown in Fig. 5.8 was measured at different powers of the confinement and measurement beam: $P_{325} = 1\,\mu W$ and $3\,\mu W$, and the measurement beam $P_{633} = 65\,\mu W, 100\,\mu W,$ and $1\,mW$.

Fig. 5.9 shows the change in contrast with increasing number of switching cycles for different laser powers P_{325} and P_{633}. The contrast decreases with increasing number of cycles because of the increase in the concentration of the degraded molecules after each switching cycle. The change in contrast is comparable for various power combinations which are an order magnitude less than their respective threshold powers. However, when the measurement beam is used at power $P_{633} = 1\,mW$, the contrast drops faster than the other power combinations such that after only 180 cycles the contrast is halved. This supports our previous observation that the AML can degrade even at a wavelength from VIS spectrum. However, since switching is a dynamic process, we cannot conclude any correlation between contrast and individual effect of the powers of the confinement and the measurement beams. Nevertheless, the decrease in contrast at small irradiation powers indicates that the parasitic side reactions occur even at lower powers of the confinement and the measurement beam.

5.2 Illumination scheme for AMI in Reflection

To achieve high resolution, the layer absorbance must be high enough to sufficiently suppress the signal outside of the aperture. However, the preliminary analysis of the AML shows that absorption of the layer is limited due to low concentration of the

BTE-1 molecules. Since concentration of BTE-1 molecules in an AML with a given thickness cannot be increased, we increased the thickness of the AML to improve the absorption of the layer [61].

Furthermore, the theoretical model investigating the implementation of absorbance modulation in 2D reflection microscopy is based on co-illumination of the confinement and measurement PSFs. For which, the AML must undergo numerous switching cycles to reach a photostationary state and generate a sub-wavelength aperture [4, 5]. The results of the previous section also reveals that the AML can undergo only a limited number of cycles. Therefore, with the goal to implement high-resolution imaging via absorbance modulation in a thick AML with limited number of switching cycles, we optimised the experimental conditions and implemented a sequential illumination scheme instead of simultaneous irradiation of the confinement and measurement PSFs. The schematics and timeline of the sequential illumination scheme are outlined in Fig. 5.10.

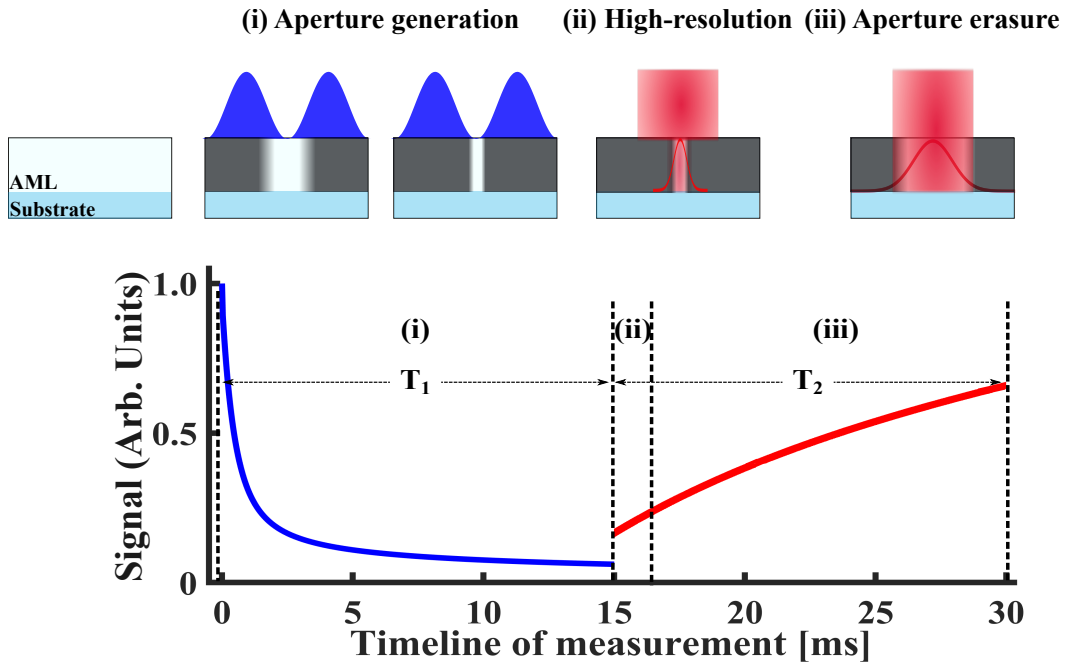

Figure 5.10: Schematics and timeline of the illumination scheme for AMI in reflection. (top) (i) An AML-coated substrate is first illuminated with a 1D doughnut-shaped confinement beam (λ_1) for time T_1 to generate an aperture. (ii) Sequentially, the Gaussian focus of the measurement beam (λ_2) is illuminated for time T_1, for a high-resolution measurement through the aperture, generating an effective PSF of sub-wavelength size. (iii) Simultaneously, the aperture is erased in time due to absorption of the opaque AML at wavelengthλ_2. (bottom) The figure shows the change in reflected signal from the substrate due to the change in absorbance of the AML over the measurement timeline at each scan position. The dotted vertical lines show the three phases (i), (ii) and (iii) of the illumination scheme.

This scheme has three phases: (i) aperture generation, (ii) high-resolution measure-

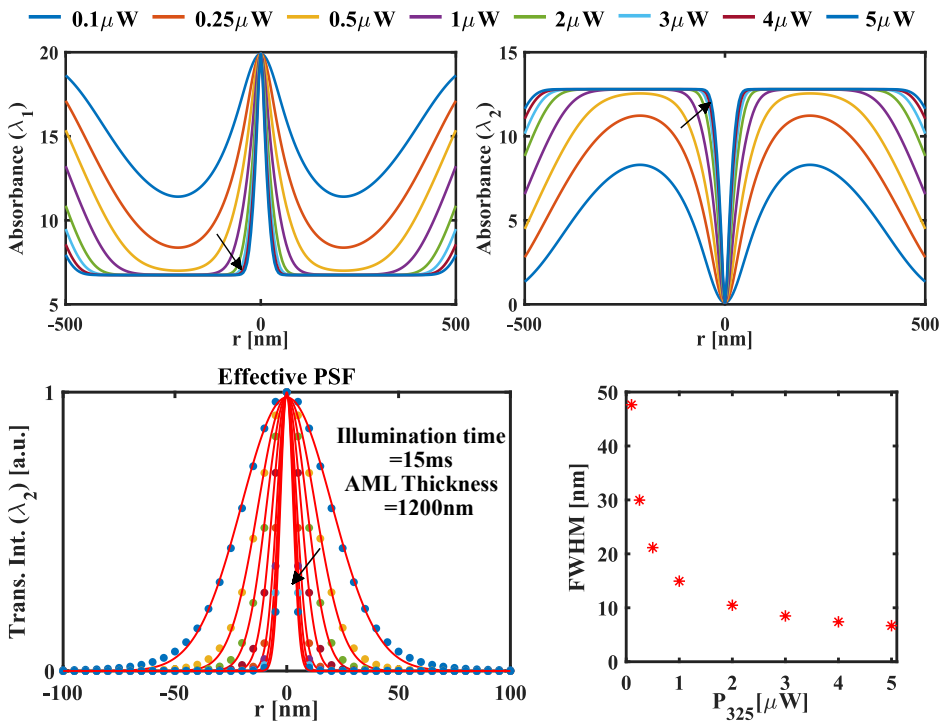

Figure 5.11: (top) The spatial distribution of absorbance of the AML at wavelength (left) λ_1 and (right) λ_2, effectively indicating the generation of the aperture. (bottom,left) The transmitted intensity of the measurement beam through the aperture, the effective PSFs, obtained at various illumination power of the confinement PSF. The arrows indicate the increasing power of the confinement PSF, P_{325} = 0.1 µW, 0.25 µW, 0.5 µW, 1 µW, 2 µW, 3 µW, 4 µW and 5 µW. (bottom,left) The estimated FWHM of the effective PSFs at various powers.

ment and (iii) aperture erasure. The initial photochromic state of the AML is the open state; thus, we first illuminate it with the 1D doughnut confinement beam (λ_1) for T_1 ms, until an aperture is generated. The AML is switched-OFF and is opaque for the light of wavelength λ_2 everywhere except in the vicinity of the central minimum of the 1D-pattern (see Fig. 5.10(i)). The sample is then illuminated with a Gaussian shaped focus of the measurement beam at λ_2 for T_2 ms, to measure the back-reflected signal from the sample through the generated aperture, resulting in an effective PSF of size below the diffraction limit, as shown in Fig. 5.10(ii). However, when the measurement PSF is illuminated for high-resolution measurement, the aperture is simultaneously erased due to high absorption of the AML at wavelength λ_2 (see Fig. 5.10(iii)) [10, 11]. As a result, the high-resolution image must be extracted from the earlier time points, marked as (ii) in the timeline illustrated in Fig. 5.10.

The timeline of measurement shown in Fig. 5.10 shows the time of measurement at a single scan position, and thus corresponds to a pixel dwell time of $T_1 + T_2$. This illumination sequence is rastered over the measurement surface to obtain the image of the object. As mentioned in Chap. 4.1, a shutter is used to block the residual

intensity of the UV laser which passes through the AOM. It has a maximum speed of 150Hz (see Fig. 4.1) which restricts the minimum pixel dwell time in the measurement to $\approx 7\,\mathrm{ms}$. Based on the limitation of the system and the results from Sect. 5.1, the exposure time and powers of the confinement and measurement beams were determined.

We also simulated the aperture generation using the sequential illumination scheme to estimate the size of the aperture and effective PSF. For the simulation, an initial concentration $C_0 = 1157.65\,\mathrm{mol\,m^{-3}}$ is used and rest of the parameters are used from table. 3.1 and 3.2. However, here an AML of thickness 1200 nm is exposed to a 1D-pattern with a waist radius of 280 nm (NA = 0.65) for $T_1 = 15\,\mathrm{ms}$. Fig. 5.11(top) shows the spatial distribution of absorbance of the molecules at wavelength λ_1 (left) and λ_2 (right), effectively indicating the generation of the aperture in the AML. The arrow indicates the increasing power of the 1D-Pattern from $P_{325} = 0.1\,\mu\mathrm{W}$ to $5\,\mu\mathrm{W}$. The corresponding effective PSFs transmitted through the aperture and their estimated FWHMs at different powers of the confinement PSF is shown in Fig. 5.11(bottom). We see that at the lowest power of the confinement beam, the estimated FWHM is similar to that for simultaneous illumination, which is $\approx 60\,\mathrm{nm}$ (see Fig. 3.7).

5.3 Resolution of AMI in Reflection

As discussed, our illumination scheme can reduce the required number of switching cycles for generating an aperture in the AML. However, for a homogeneous resolution over a measurement surface via 2D AMI in reflection, the available switching cycles are still insufficient. Therefore, to optimally use the AML with its existing low fatigue resistance, we have restricted the high-resolution measurements to one dimension in this thesis.

The first experimental results of the 1D AMI in reflection microscopy are presented and discussed in this section. We experimentally validate the sequential illumination scheme and demonstrate 1D resolution enhancement by measuring a sample containing gold nanoparticles. Subsequently, the results of measurements on nanostructured samples are shown to demonstrate the feasibility of the proposed scheme for the application in structural and morphological analysis of nanostructures.

Since we measure the reflected signal from nanoparticles, the size of gold beads is an important parameter. According to the general theory of light scattering by a spherical particle, developed by Gustav Mie, a particle of size R much smaller than the wavelength ($2\pi R << \lambda$) has a scattering cross section that varies as R^6, while its absorption cross section varies as R^3. This implies that for very small particles, absorption is more significant than scattering. On the other hand, scattering becomes

more important with the increasing size of the particle, when $2\pi R$ is comparable to the wavelength. However, in the latter scenario, the amount of back-scattering (reflected signal) from the particle is very sensitive to the refractive index of the particle in relation to the refractive index of the surrounding medium [75]. We selected the nanoparticles of 80 nm diameter, which lies on the boundary between the above mentioned cases. The chosen size of the gold beads works well with the alignment sample (Sect. 5) such that there is enough reflected signal collected by the objective to image them. However, with the AML-coated GB sample, depending on the apparent size of the gold bead in the FOV and the refractive index of the AML, we record a negative bead i.e. an image with a bright background and a dark gold bead. To make the presented results comprehensible, the recorded (1D) images of the gold nanoparticles have been inverted. The data is normalised using min-max normalisation after subtracting each pixel value from the maximum pixel value within the image.
Before performing high-resolution imaging, some of the optics in the setup are modified to optimise the experimental conditions. For AMI in reflection, a low noise detector Amp-PD will be used. To maximise the reflected signal of the measurement PSF that reaches the detector, the pellicles (PL1 and PL3, Fig. 4.1) are removed from the setup. It is essential to generate a perfect 1D-Pattern with a zero-intensity line to generate the channel in the AML. In order to do so, the confinement beam must be linearly polarised (perpendicular to the phase step) [52]. The polarisation state of the measurement beam is also changed to linear. This is because the rotational mobility of the photochromes in the PMMA layer is not known. In order to ensure that both beams act on the same subgroup of molecules, even if their dipole moment is fixed during the illumination time, we match the polarisation of the measurement beam to the one of the confinement beam. The confinement and the measurement beam have a 1D doughnut-shaped (1D-Pattern) and Gaussian intensity distribution in the focal plane, respectively.

5.3.1 Gold Nanoparticles

As discussed in Chap. 2, Sect. 2.2, a confocal reflection microscope is a coherent imaging system; however, the coherent nature of the imaging system does not affect the PSF obtained by imaging a point-like object. Therefore, we image gold nanoparticles to demonstrate the imaging capability of the AMI in reflection microscopy beyond the diffraction limit using the sequential illumination scheme discussed in Sect. 5.2.

Gold bead measurement: An 80 nm GB sample coated with 1200 nm thick AML is used for the measurements. At first, a 2D confocal image of a gold bead is acquired through the measurement PSF with focal power $P_{633} = 100\,\mu W$. The 2D image is scanned along the xy-axis using the NanoMax stage with a pixel size and pixel dwell time of 100 nm and 10 ms, respectively.

To acquire a 1D confocal image, the selected gold bead is scanned only along the x-axis through the measurement PSF at power $P_{633} = 100\,\mu W$, with a pixel size of 30 nm and pixel dwell time of 15 ms.

For a 1D AMI image, the gold bead is again scanned along the same line, using the sequential illumination of the confinement and measurement PSF. At first, the pixel is illuminated with the 1D-Pattern at power $P_{325} = 3\,\mu W$ for $T_1 = 15$ ms to generate the aperture. Then on the same pixel, the measurement PSF is illuminated with at power $P_{633} = 100\,\mu W$ for another $T_2 = 15$ ms. For 1D AMI measurement, pixel size is 30 nm and the pixel dwell time is $T_1 + T_2 = 30$ ms. During the complete measurement, the reflected signal of the measurement beam is recorded with a time resolution of 10 µs. Fig. 5.12 shows the measured 2D and 1D images of the gold bead.

Fig. 5.12a shows the acquired 2D confocal image of a gold bead. The 1D confocal image of the selected gold bead is measured by scanning along the red dotted line in Fig. 5.12a. The detected back-reflected signal at 633 nm for each pixel for 15 ms is shown in Fig. 5.12b. Note that the x-axis in 2D confocal image corresponds to the vertical-axis in Fig. 5.12b. The confocal line profile, shown in Fig. 5.12c, is obtained along the black solid line in Fig. 5.12b. A Gaussian function is used to fit the acquired line profile. An FWHM of 412.29 $\pm$1.53nm is estimated, which defines the resolution of the confocal reflection microscope.

For the 1D high-resolution imaging via absorbance modulation, the gold bead in Fig. 5.12a is again scanned along the red dotted line according to the illumination scheme illustrated in Fig. 5.10. The detected back-reflected signal at 633 nm for each pixel for 15 ms is shown in Fig. 5.12d. Here again the horizontal-axis shows the measurement time, and the vertical-axis corresponds to the scan positions (x-axis in Fig. 5.12a). During AMI, only the back-reflected signal of the measurement PSF is detected, hence, we refer time T_2 of the total pixel dwell time as the *measurement time*.

Since the aperture is erased in time upon illumination with the measurement beam, the high-resolution 1D image of the gold bead is extracted from the initial time points of the acquired data. The data is obtained at $T_2 = 50$ µs and averaged over a time window of 100 µs, depicted by the green rectangular window in Fig. 5.12d. Fig. 5.12e shows the line profile obtained by AMI (red stars). As before, a Gaussian function is used to fit the line profile (black solid line). The FWHM of the effective

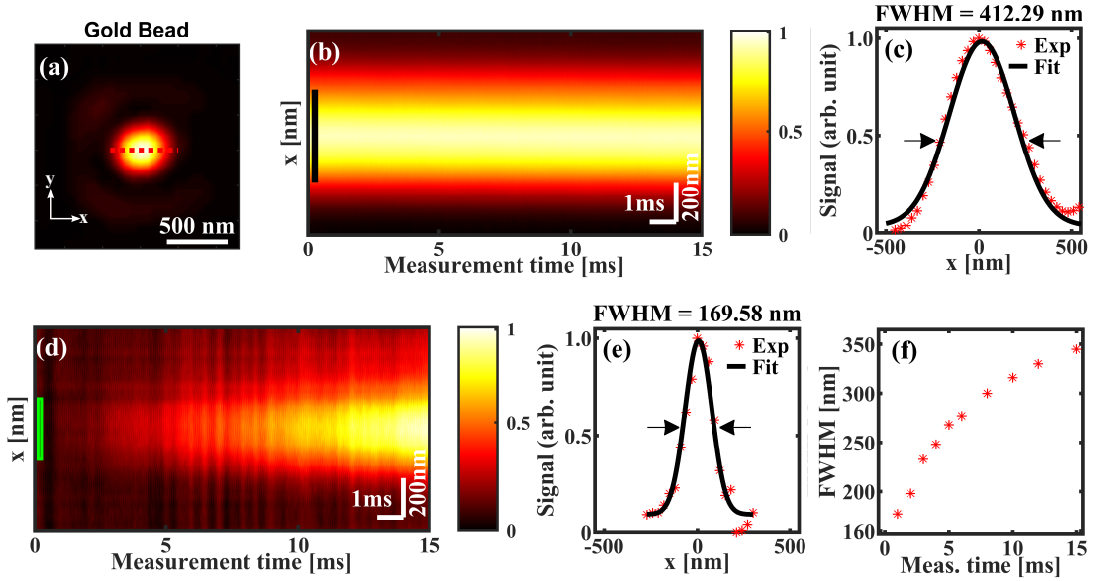

Figure 5.12: High-resolution gold bead measurement. (a) Acquired 2D confocal image of a single gold bead with the measurement PSF with power $P_{633} = 100\,\mu W$. (b) The measured back-reflected signal for each pixel (vertical-axis) for the 15 ms (horizontal-axis). (c) 1D confocal image of the same gold bead, scanned along the red dotted line in (a), through the measurement PSF with power $P_{633} = 100\,\mu W$. The line profile (red stars) is fitted using a Gaussian function (black solid line) and an FWHM of 412.29 $\pm$ 1.53nm is estimated. (c) Raw measurement data of the 1D AMI measurement scanned though the measurement PSF with power $P_{633} = 100\,\mu W$. (d) The measured back-reflected signal at 633 nm for each pixel (vertical-axis) for the 15 ms (horizontal-axis) during AMI image acquisition. (e) 1D AMI image of the gold bead obtained from the earlier times (green box) of measurement data in (d). AMI line profile (red stars) is fitted with a Gaussian function and an FWHM of 169.58 $\pm$ 0.72nm is computed. (f) The increasing FWHM of the measured gold bead in (d) with respect to time.

PSF is computed to be 169.58 $\pm$ 0.72nm. Compared to the confocal microscope, the resolution of AMI reflection microscope is thus enhanced by a factor of 2.43. With the vanishing aperture, the FWHM of the effective PSF increases to the value of the estimated confocal FWHM. The increase in the size of the effective PSF with respect to the illumination time of the measurement PSF can be directly visualised in Fig. 5.12f, where we show the FWHMs calculated from the data in Fig. 5.12d at different measurement times.

In Fig. 5.12, we have only compared the central peak of the confocal PSF and effective PSF. However, when we look at the experimental data over the entire scan range, significant side lobes are observed in the AMI line profile. Fig. 5.13 shows the normalised line profiles of the measured gold bead in Fig. 5.12 over the entire scan range. The green and blue solid lines show the line profile of the gold bead measured via AMI at different measurement times, $T_2 = 200\,\mu s$ and $T_2 = 10\,ms$, respectively. The red dashed curve shows the confocal line profile.

The confocal (red) and AMI (blue) line profile at $T_2 = 10\,ms$ have comparable

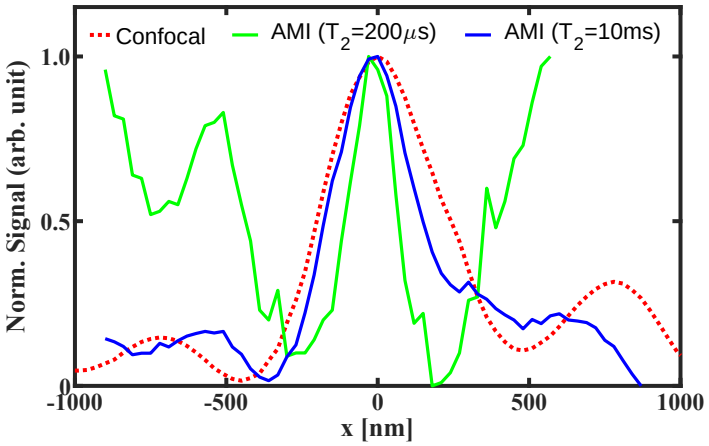

Figure 5.13: The figure shows the normalised line profiles of the measured gold bead, shown in Fig. 5.12, over the entire x range. The green and blue solid lines show the line profiles of the gold bead measured via AMI at different measurement times $T_2 = 200\,\mu s$ and $T_2 = 10\,ms$, respectively. The red dashed line shows the confocal line profile of the gold bead.

signals in the central peak and the side lobes. However, a significantly lower signal is collected via AMI during the initial measurement times due to the necessary absorption of the measurement PSF through the aperture. Compared to the confocal line profile's maximum signal, the AMI's maximum signal is approximately 10%. Comparing the positions of the side lobes in Fig. 5.13, it is inferred that the side lobes of the illuminated Gaussian measurement PSF are not sufficiently suppressed via the AML absorbance. As a consequence, the central lobe of effective PSF and the side lobes in the confocal line profile have approximately the same height. At the later measurement time however, the acquired signal increases with the vanishing aperture in the AML, resulting a clear central peak with lower side lobes (see Fig. 5.13, blue curve).

To understand the appearance of the side lobes in Fig. 5.13, we have to take a closer look at the illuminated PSFs. As pointed out earlier in Chap. 2, we are using a SO to eliminate chromatic aberrations. However, the Gaussian PSF generated by the annular aperture of SO has significant side lobes when compared to the Gaussian PSF generated by a standard objective with circular aperture (see Fig. 2.3 and 2.2). In order to verify if the SO influences the suppression of the side lobes, the 1D-Pattern and Gaussian PSF at the confinement and measurement wavelength, respectively, generated by a standard objective and a SO are compared. Fig. 5.14 shows the simulated (a,d) 1D-Pattern at the confinement and (b,e) Gaussian PSF at the measurement wavelength using a standard objective lens and SO, respectively, with a NA of 0.65. The line profiles along the red dashed lines in Fig. 5.14a,b and Fig. 5.14d,e are shown in Fig. 5.14c and Fig. 5.14f, respectively.

In Fig. 5.14c, we see that if both the PSFs are perfectly superimposed, such that the central minimum of the 1D-Pattern coincides with the central maximum of the

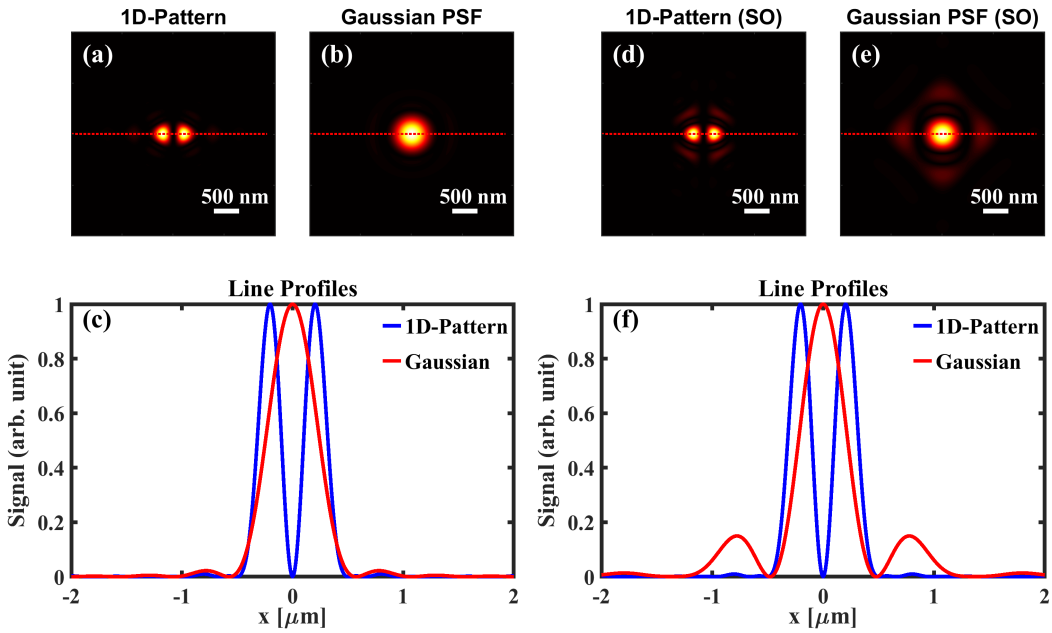

Figure 5.14: A 2D intensity distribution of (a,d) 1D-Pattern at λ_1 and (b,e) Gaussian PSF at λ_2 generated by a standard lens based objective and SO, respectively. (c) A 1D intensity distribution of 1D-Pattern (blue) and Gaussian PSF (red) along the red dashed lines in (a) and (b), respectively. (f) A 1D intensity distribution of 1D-Pattern (blue) and Gaussian PSF (red) along the red dashed lines in (d) and (e), respectively.

Gaussian PSF, the maxima and minima of the side lobes also coincide. Furthermore, the strength of the side lobes in 1D-Pattern is higher than that of the Gaussian PSF. Considering this intensity distribution during aperture generation in AMI, at appropriate powers of 1D-Pattern and measurement PSF, we can certainly assume that the side lobes of the Gaussian PSF will be well suppressed. On the contrary, in Fig. 5.14f, firstly, we see that the strength of the side lobes of the Gaussian PSF significantly increases to more than 10% of the central peak. Furthermore, at the same time, the side lobes of the 1D-Pattern become insignificant, which is unfavourable for the suppression of the side lobes via AMI.

In Fig. 5.13, it can also be noticed that the position of the side lobes in AMI profile (blue curve) is shifted with respect to that of the confocal side lobes (red curve). In order to understand this shift, the side lobes in Fig. 5.14 must be examined further. The intensity distribution of the side lobes of Gaussian PSF is not rotationally symmetric, it depends on the position of the spider legs in the SO (see Fig. 5.14). In the simulation, the position of the spider legs is assumed to be along x- and y-axis, like a plus sign "+". However, in our microscope, the SO is placed in a manner that the spider legs are in a cross position "×". Hence, the 1D line profiles along the x-axis in our measurements does not have an identical profile as shown in Fig. 5.13c. Fig. 5.15a,b show the experimental 1D-Pattern and Gaussian measurement PSF, respectively. When compared with the simulated Gaussian PSF in Fig. 5.14e, we can see that the position of the spider legs changes the intensity distribution of the side

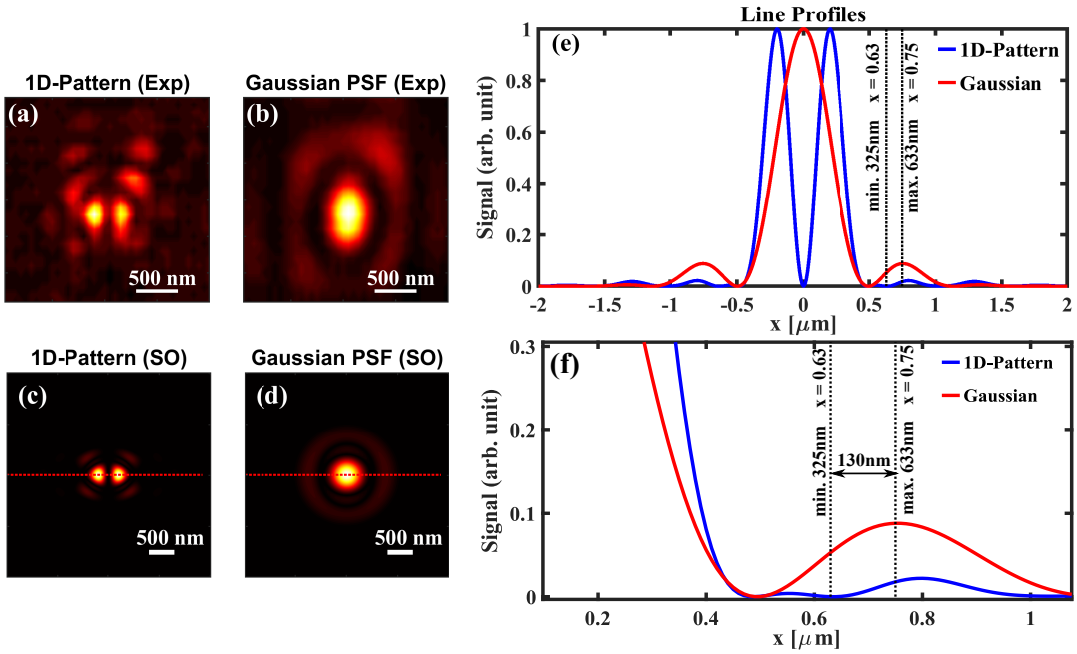

Figure 5.15: A 2D intensity distribution of experimentally measured (a) 1D-Pattern at λ_1 and (b) Gaussian PSF at λ_2. (c),(d) A 2D intensity distribution of simulated 1D-Pattern at λ_1 and Gaussian PSF at λ_2 generated by a SO without spider legs. (e) A 1D intensity distribution of 1D-Pattern (blue) and Gaussian PSF (red) along the red dashed lines in (c) and (d), respectively. (f) A magnified region from (e), containing the side lobes of the confocal and 1D-Pattern.

lobes. To understand the line profiles of the experimental 1D-Pattern and Gaussian PSF, we simulated the PSFs again using SO with a NA = 0.65, however, without the spider legs. Fig. 5.15c,d shows the simulated 1D-Pattern of wavelength λ_1 and Gaussian PSF of wavelength λ_2, respectively. Fig. 5.15e shows the superimposed line profiles of the PSFs along the red dotted line. Looking closely at the side lobes, we see that the 1D-Pattern features additional minima and maxima in the region with side lobes of the Gaussian PSF. Fig. 5.15f shows a magnified image of the region with the side lobes. It is clearly visible that due to the variation in the intensity distribution of the minima and maxima of the two PSFs, side lobes of the Gaussian PSF are partially (spatially) suppressed. The amount of suppression depends on the power of the confinement PSF, however, at the minimum (x = 0.63 µm) of 1D-pattern, we can safely assume that red curve is not suppressed. Whereas, at the maximum of the Gaussian side lobe (x = 0.75 µm), there will be some amount of suppression. This would result in a shift of ≈ 130 nm in the side lobes of AMI line profile with respect to the confocal line profile. This mismatch of the maxima and minima of the PSFs, results in shifted side lobes in the measured effective PSF as shown in Fig. 5.13.

As stated before, the acquired signal through the aperture in AMI is as low as the contribution of the side lobes in a confocal PSF. The combination of the unsup-

pressed side lobes and low signal in the central lobe of the effective PSF, results in the green curve shown in Fig. 5.13. A simple solution to prevent this outcome would be to switch to a standard objective, however, due to the illumination wavelengths used for AMI, which are governed by absorption spectra of the BTE-1 molecules (see Fig. 3.2), we continue our experiments with the SO.

As already noted in Sect. 5.1, it is established that higher powers of the irradiated PSFs induce degradation in the AML. In order to see the effect of degradation during AMI measurements, the measurement with 80 nm gold beads, as shown in Fig. 5.12, was repeated at different powers of the 1D-Pattern. Out of the three different powers, $P_{325} = 3\,\mu W,\ 5\,\mu W$ and $10\,\mu W$, selected for the measurements, two of them are less than the threshold and one has the same order of magnitude as the threshold power. The power of the measurement PSF is kept the same as before, $P_{633} = 100\,\mu W$ and the illumination time is reduced to $T_1 = T_2 = 10\,ms$. For each measurement, first a 2D confocal image of a gold bead is obtained. Following this, a 1D confocal image is acquired by scanning through the centre of the selected gold bead along the x-axis, similarly to what is shown in Fig. 5.12a. Thereafter, along the same x-axis scan, a 1D AMI image is acquired through sequential illumination of the 1D-Pattern and measurement PSF at each pixel. Fig. 5.16 compares the acquired confocal (red) and AMI (green) line profiles for three different sets of measurements. As before, the AMI line profile is extracted from the initial measurement time points. For all line profiles, the data is averaged over a time window of 100 µs. Please note that the three sets of measurements were recorded each at a different position in the GB sample.

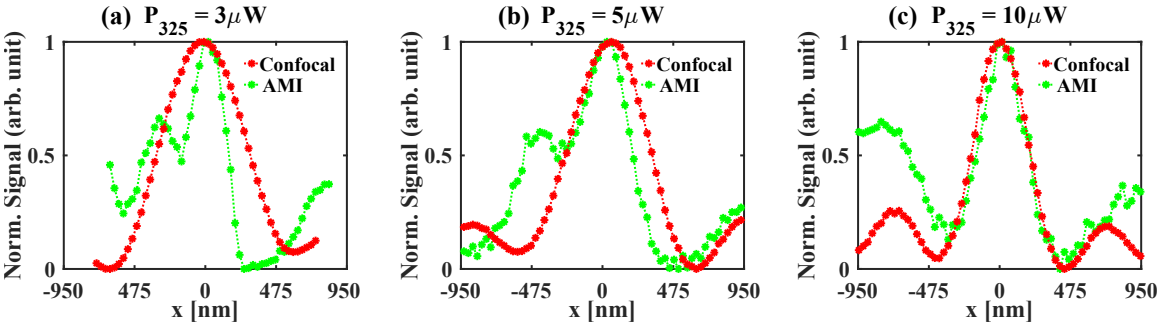

Figure 5.16: The figure shows results of 1D resolution measurements using the 80 nm GB sample with 1200 nm thick AML, at various powers of the 1D-Pattern (a) $P_{325} = 3\,\mu W$ and (b) $P_{325} = 5\,\mu W$ and (c) $P_{325} = 10\,\mu W$. The red and green curve in (a),(b) and (c) show the line profiles of the gold bead acquired by confocal and AMI, respectively.

Fig. 5.16a shows the results for the first set of measurements with $P_{325} = 3\,\mu W$. The FWHM of the confocal line profile is $602 \pm 4.3\,nm$, which is larger than the $\approx 415\,nm$, derived from the previous measurement of a single 80nm GB (Fig. 5.12). This indicates that the underlying reflective structure is larger than a single GB. Indeed, in the AMI line profile, we see two peaks at a distance of 310nm which

indicates that there are two closely spaced beads that are resolvable with AMI, but not with the confocal microscope.

Fig. 5.16b shows the obtained confocal and AMI line profiles for the second set of measurements ($P_{325} = 5\,\mu W$). Here the confocal line profile has an FWHM of 570 ± 12.92nm, which is again higher than expected for a single GB. As in the previous measurement, two peaks are observed in the AMI line profile. The distance between the two peaks is 417 nm. Since there are two separate beads in the object plane, the imaging process cannot be assumed to be incoherent anymore. Due to lack of phase information added because of the significant sidelobes in the obtained AMI PSF, neither the actual distance between the two beads nor the actual resolution enhancement can be determined exactly. However, for both cases, it can be stated that the resolution is indeed increased by AMI.

The line profiles for the third set of measurements ($P_{325} = 10\,\mu W$) are shown in Fig. 5.16c. Here, the confocal line profile has a FWHM of $392.5\,nm \pm 11.25\,nm$, indicating the presence of a single GB. However, the FWHM of the effective PSF is also estimated to be $348\,nm \pm 35.9\,nm$, virtually providing no resolution enhancement.

It can be inferred from this measurement, that the aperture in the AML is not generated as expected. This is also confirmed by the unnormalised line profiles (data not shown). They show that the height ratio of the main peaks in the AMI profile and in the respective confocal profile is significantly higher than for the other two sets of measurements. This indicates that the AML absorbance is significantly less than expected. It has been shown in Sect. 5.1.3 that the AML has a limited number of switching cycles, thus the comparatively high power ($P_{325} = 10\,\mu W$) of the 1D-Pattern (either because of the higher local intensity or because of the higher light dose) induces degradation in the AML such that the overall concentration of the active molecules decreases and the expected spatial distribution of the absorbance at λ_2 is not acquired. These measurements evidently show that the AML degrades at higher UV power which is not favourable for AMI. Therefore, for AMI measurements it is better to use powers well below the threshold quantified in Sect. 5.1.1.

5.3.2 Edge Response

Another practical way of defining the resolution of a microscope is by measuring its edge response. Characterising the edge response or the edge spread function (ESF) of a microscope can be done using the $20\% - 80\%$ edge-response criterion [34], using analytical function models for the ESF fitting or by deriving the PSF from the edge response of the microscope [76]. We will adopt the latter and derive the PSF from the measured ESF, to estimate the resolution of the microscope.

Edge measurement: The calibration sample, coated with 1200 nm thick AML, is used for the measurement. The dark squares surrounding the various grating structures (see Fig. 5.1) are used for the edge measurements. First a 2D confocal image of the edge is recorded using the measurement PSF at power $P_{633} = 100\,\mu W$. To measure the 1D confocal ESF, the sample is scanned along the x-axis, which is perpendicular to the edge, using the measurement PSF at power $P_{633} = 100\,\mu W$, with a pixel dwell time of 50 ms. Thereafter, an AMI line profile is measured along the same axis, by scanning sequentially through the confinement PSF with power $P_{325} = 1\,\mu W$ and measurement PSF with $P_{633} = 100\,\mu W$. Since the light dose of 1D-Pattern is critical for the aperture generation, an illumination time of $T_1 = 50$ ms is chosen, to keep the light dose same as in the previous measurements with the gold nanoparticles. Due to the limitation of the software used for acquiring data, the measurement time T_2 is also 50 ms. However, we did not reduce the power of the measurement PSF because at powers $P_{633} < 100\,\mu W$ the detected signal is insufficient to generate a high-resolution image. Therefore, a pixel dwell time of 100 ms is used for AMI. The results of the edge measurements are shown in Fig. 5.17.

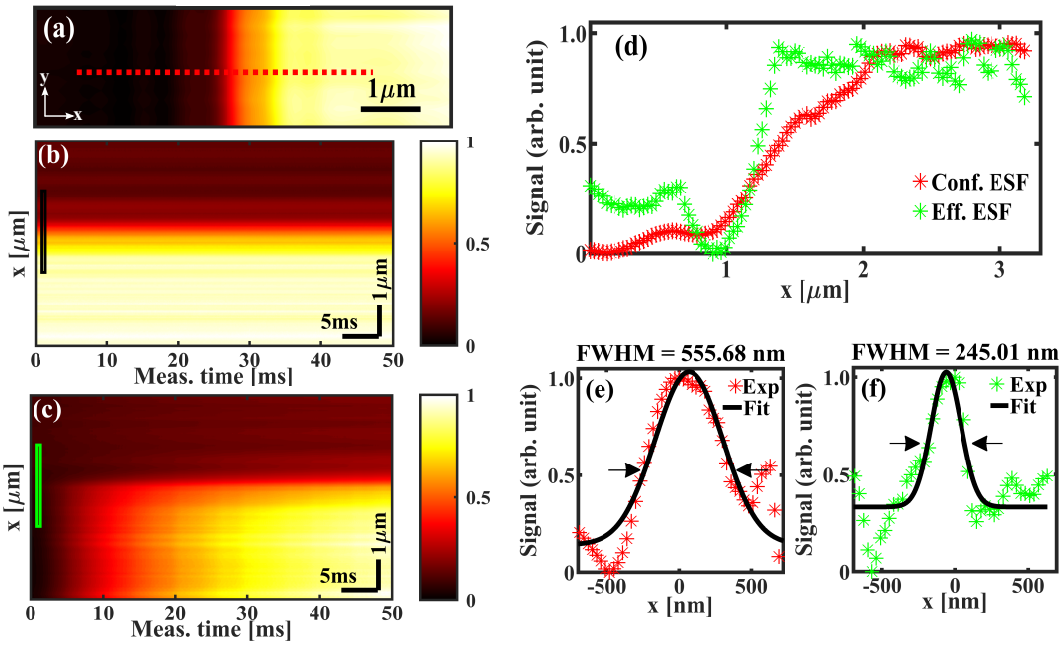

Figure 5.17: High-resolution edge measurement. (a) A FOV of $7 \times 1.40\mu m^2$ of an edge in the calibration sample. (b,c) The detected signal at measurement wavelength for each pixel for 50 ms for confocal and AMI measurement, respectively. (d) Confocal ESF and ESF obtained via AMI, effective ESF, are plotted against the scan positions marked with a black rectangle in (b), and green rectangle in (c), respectively. PSFs of the confocal and AMI obtained by differentiating the ESF in (d), are shown in (e) and (f), respectively.

Fig. 5.17a shows the 2D confocal image of a FOV of $7 \times 1.40\mu m^2$ of the edge in the calibration sample. Along the red dashed line in Fig. 5.17a, the sample is scanned to measure the confocal edge response. The detected signal at the measurement

wavelength for each pixel for 50 ms is shown in Fig. 5.17b, here the horizontal-axis is the measurement time and the vertical-axis corresponds to the scan positions (x-axis in Fig. 5.17a). The normalised data from the marked black rectangle in Fig. 5.17b is shown in Fig. 5.17d using red markers.

The sample is scanned again using the AMI illumination scheme. The recorded signal at the measurement wavelength for each scan position for 50 ms is shown in Fig. 5.17c. Since the aperture is erased upon illumination with the measurement PSF, the high-resolution image is produced by the data from early time points, as done in the gold bead measurements. The extracted high-resolution data is taken at $T_2 = 2$ ms averaged over a time window of 200 µs depicted by the green rectangular box in Fig. 5.17c. The normalised data from the selected region is plotted in Fig. 5.17d with green markers, showing the ESF of AMI. A distinct difference in the slope of the ESFs is observed in Fig. 5.17d, representing the improvement in resolution.

To estimate the PSFs of the confocal and high-resolution measurements, the ESF data is differentiated along the x-axis. Fig. 5.17e,f show the computed confocal and AMI PSFs, respectively. The PSFs are fitted using a Gaussian function, and the calculated FWHMs are 555.68 ±26nm and 245.01 ±16.8nm for confocal and AMI, respectively. This means that a resolution enhancement factor of 2.27 is achieved which is consistent with the result obtained from the gold nanoparticle.

5.3.3 Sample Stability

In a long run, the coated samples used for AMI in reflection microscopy must be stable. In general, we have realised that the AML is stable i.e., its reversibly switchable nature is reproducible and the sample can be used for months without re-coating the measurement surface. However, in some regions of the AML, the BTE-1 molecules show irreversible behaviour.

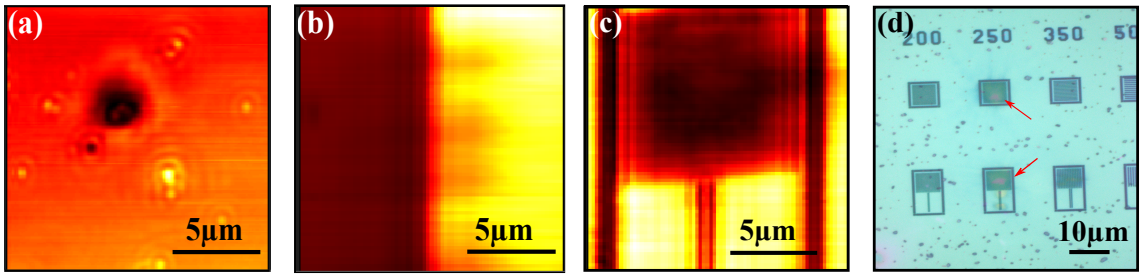

Figure 5.18: 2D scanned images of the samples used in various experiments are shown. (a) 80 nm GB sample, (b) and (c) shows the calibration sample with a FOV of the edge and a grating structure of period 500 nm, respectively. The image of the calibration sample measured using the reflected light microscope is shown in (d).

In Fig. 5.18, 2D scanned images of the samples used in various experiments are shown, (a) is a 80 nm GB sample, (b) and (c) shows calibration sample, with the edge

and a grating structure of period 500 nm, respectively. The image of the calibration sample measured using the reflected light microscope is shown in Fig. 5.18d. The dark regions in (b) and (c) are the degraded regions of the AML, where the AML does not switch anymore. Fig. 5.18a,d also show impurities in the layer, (d) also shows the degraded AML regions under a reflected light microscope, shown by red arrows.

5.3.4 Imaging a Grating

The motivation of the project is to develop an optical technique that can be used for structural and morphological analysis of real-world materials. Therefore, to demonstrate the practicality of the proposed scheme for the application in the analysis of nanostructures, a 1D reflective grating structure is imaged via AMI in reflection.
The calibration sample coated with a 1200 nm thick AML (see Fig. 5.1), contains multiple patterns on the nanometer scale. A grating with a linewidth of 250 nm and a grating period of 500 nm is used for the measurement.

Grating measurement: First, a 2D confocal image over a FOV of $15 \times 7\mu m^2$ of the selected grating is recorded at power $P_{633} = 100\,\mu W$. A pixel dwell time of 10 ms and pixel size of 200 nm is used.
For the 1D measurements, the pixel size is changed to 30 nm. As previously done for the edge measurement, lower power of UV light and longer pixel dwell time are used. First a 1D confocal image is measured along a line that is perpendicular to the grid lines using the measurement PSF at power $P_{633} = 100\,\mu W$ with pixel dwell time of 50 ms. Subsequently, a 1D AMI line profile is recorded using the 1D-Pattern and measurement PSF sequentially, at power $P_{325} = 1\,\mu W$ and $P_{633} = 100\,\mu W$, respectively, along the same scan line with an illumination time of $T_1 = T_2 = 50$ ms. The results of the 1D measurements are shown in Fig. 5.19.
Fig. 5.19a shows the 2D confocal image of the grating area. The 1D confocal image recorded along the selected black dashed line in the 2D confocal image. The reflected signal at 633 nm for each scan position over the measurement time is shown in Fig. 5.19b. Though the signal shows some spatial modulation, no agreement with the underlying grid structure is visible and no structural information can be inferred. For the 1D AMI measurement, the grating is again scanned along the black dashed line in Fig. 5.19a, using the illumination sequence implemented before for imaging the gold nanoparticles and edge-structure. The raw measurement data of AMI is shown in Fig. 5.19c, where the grating structure is clearly visible for the initial time points. The data for comparing the line profiles of both the measurements is extracted from the black and green rectangular box, shown in the measurement windows of (b) confocal and (c) AMI measurement, respectively. The data is averaged

over a time period of 400 µs. Fig. 5.19d shows the comparison of the normalised line profiles obtained via confocal and AMI in red and green, respectively. The confocal line profile does not show any resolvable structural information, whereas, the AMI profile provides an increased resolution and the adjacent lines in the grating can be readily discerned. The distance between the measured peaks in Fig. 5.19d agrees well with the grating period of the measured structure. However, the relative peak distance slightly varies over the x-range. A variation in the height of the peaks is also observed which can both be caused by the significant sidelobes in the AMI PSF in combination with coherent effects, discussed in Sect. 5.3.1.

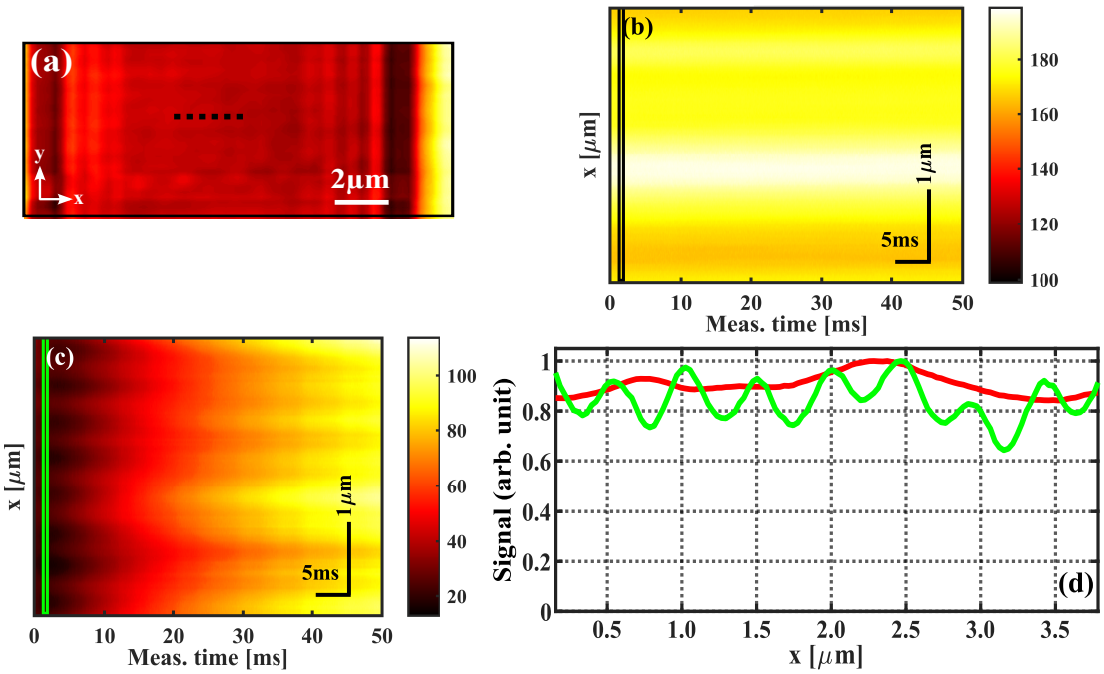

Figure 5.19: Demonstration of AMI in reflection microscope to image a 1D periodic structure. (a) A FOV of $15 \times 7\mu m^2$ of the 1D grating structure in the calibration sample scanned through the measurement PSF. (b) Raw measurement data acquired via 1D confocal scan through the measurement PSF. (c) Raw measurement data acquired via 1D AMI scan through sequential illumination of the 1D-Pattern and measurement PSF. The horizontal-axis shows the measurement time in ms and the vertical-axis shows the scan positions in µm in (b) and (c). (d) The line profiles obtained via confocal imaging and AMI are shown with red and green solid lines, respectively. The data for the red and green curves are extracted from the region, marked by the black and green rectangle in (b) and (c), respectively.

Chapter 6
Summary and Outlook

Absorbance modulation is an expansion of the fundamental principle used in super-resolution fluorescence microscopy, in which instead of using fluorophores, reversibly switchable photochromic molecules are utilised to achieve high resolution. Application of this technique in the field of optical lithography (AMOL) [3] and transmission microscopy (AMI) [4] has shown resolution enhancement down to a tenth of a wavelength (in AMOL). In the theoretical study published by Kowarsch *et al.*, this idea is extended to reflection microscopy where they show that imaging beyond the diffraction limit via AMI in reflection microscopy is indeed achievable. The main aim of the present work was to experimentally demonstrate high-resolution reflection microscopy via absorbance modulation.
To accomplish the goal of the thesis, we categorised the experiments performed during the course of the work as three small milestones:

- Construction of a suitable confocal reflection microscope for AMI.
- Characterisation of the AML and estimation of the optimal imaging parameters for AMI.
- Optimisation of the experimental conditions, implementation of AMI in reflection and showing an improved resolution with respect to confocal reflection microscopy by imaging gold nanoparticles.

To achieve the first milestone, a standard confocal reflection microscope was constructed. A laser of wavelength $\lambda_2 = 633\,\text{nm}$, the measurement laser, was implemented. The resolution of the microscope was characterised by imaging gold nanoparticles and estimating the FWHM of the measurement PSF. The microscope was then adapted for high-resolution AMI by adding the confinement laser of wavelength $\lambda_1 = 325\,\text{nm}$. The light at this wavelength was generated by a TiSa laser together with a frequency tripling unit. The temporal pulse length of the generated pulses at 325 nm was stretched using a self-built pulse stretcher. Since the wavelength of the confinement and measurement beams are from two distinct regions of the EM spectrum, a reflective objective lens based on the Schwarzschild design

(SO) was used in the microscope to prevent any chromatic aberrations. In our microscope, the focal intensity distribution of the confinement beam can be realised as either Gaussian, 1D-Pattern or 2D doughnut-shaped pattern. The setup was properly aligned before using it for any measurements. The details of the design and construction of the microscope were provided in Chap. 4.

To accomplish the second milestone (Sect. 5.1), we characterised the AML in terms of its temporal and behavioural response to various powers of the confinement and measurement beam. At first, the initial concentration $C_0 = 1157.65\text{mol}\,\text{m}^{-3}$ of the BTE molecules in the AML was calculated using the parameters of the AML computed at the *IPC* and *IOC, TU-Clausthal*. Then, we determined the damage threshold of the AML at the confinement and measurement wavelength to find a suitable range of powers that can be used for further experiments. In order to do so, we probed the AML at various powers of the confinement and measurement beams. We found that at powers $P_{325} \geq 40\,\mu\text{W}$ (intensity of $3\,\text{kW}\,\text{cm}^{-2}$) and $P_{633} \geq 5\,\text{mW}$ (intensity of $130\,\text{kW}\,\text{cm}^{-2}$) of the confinement and measurement beam, respectively, the AML behaves unexpectedly (see Fig. 5.5 and 5.4). Then, to investigate the temporal response, an AML-coated mirror sample was illuminated with Gaussian-shaped foci of the confinement and measurement beam. Characteristic decay and recovery curves (see Fig. 5.6 and 5.7) were obtained by monitoring the change in transmitted signal of the light of wavelength λ_2 upon illumination at various powers of the confinement and the measurement beam, respectively. The results of these measurements revealed that (i) the conversion rates of the open form increase linearly with the increasing illumination power, (ii) for the powers of confinement and measurement beam, well below the threshold, the conversion rates of the open and closed form are of the same order of magnitude (iii) the absorbance of the 400 nm thick AML is limited due to low concentration of the BTE-1 molecules in the layer.

Fatigue resistance or stability of the AML was also examined as it is an important parameter that limits the scan resolution that can be used for AMI. To evaluate the stability of the AML, we switched the layer several hundred times between open and closed states using the same experimental conditions that were used for measuring the decay and recovery curves (Sect. 5.1.3). The results of this investigation show that the AML has a limited number of switching cycles, which is about 200 cycles. This is due to the parasitic side reactions in the layer that decrease the concentration of switchable molecules after each cycle, resulting in the degradation of the AML. The measurements were repeated at different powers of the confinement and the measurement beam. Comparing the change in the modulation depth (contrast) at different powers showed that the degradation of the AML occurs even at relatively low powers of the irradiated confinement and measurement beam (see Fig. 5.9).

Based on the results of the second milestone, the thickness of the AML was increased

to 1200 nm to achieve better absorption in the layer. To optimally use the AML for AMI with the existing low fatigue resistance, we restricted AMI to one dimension. Additionally, we implemented a sequential illumination of the confinement and measurement PSFs to reduce the number of switching cycles required to generate the aperture. The timeline of the sequential illumination and data acquisition is discussed in Sect. 5.2. We experimentally demonstrated a 2.43-fold 1D resolution enhancement via AMI in reflection microscopy by imaging gold nanoparticles of diameter 80 nm. In comparison to the confocal PSF of FWHM = 412.29 ± 1.53nm, an effective PSF of FWHM = 169.58 ± 0.72nm was measured (see Fig. 5.12).
We used the reflection microscope to also image extended 1D objects. For this, we imaged an edge structure and a grating structure. In the case of the edge structure, compared with the diffraction-limited confocal resolution, AMI in reflection microscopy resulted in a 2.27-fold resolution enhancement (see Fig. 5.17). The periodic grating structure with a linewidth of 250 nm was successfully resolved as opposed to confocal imaging (see Fig. 5.19). This reflects the capability of the imaging modality to image extended structures with sub-diffraction resolution.

With the implemented imaging scheme we were able to show approximately 2.4-fold improvement in resolution. However, the extent of this improvement is limited in the current implementation due to several issues. The achievable resolution via AMI strongly depends on the quality of the aperture generated in the AML, which in turn depends on the photo-chemical properties of the AML and the spatial and temporal distribution of the illuminated PSFs. The analysis of the switching of the AML indicates that the absorbance of a 400 nm thick layer at the measurement wavelength is insufficient. This is mainly due to the low concentration of BTE-1 molecules in the layer. At present, we have increased the layer thickness to improve the overall absorption of the AML. To get around the low fatigue of the layer, we have restricted the scan range during AMI to 1D and used sequential illumination of the confinement and the measurement PSFs in the experiments. Although on one hand, the sequential illumination helps in reducing the required number of switching cycles to generate the aperture, the acquired resolution was limited in our experimental implementation due to the transient behaviour of the generated aperture. As mentioned before, the collected signal from the earliest time points during an AMI measurement is low compared to the constant background on the detector which necessitated to average over a time window of $\approx 200 - 250$µs in order to achieve a desired SNR. However, simultaneously, the aperture in the AML broadens within this time window because of the absorption of light at the measurement wavelength. Consequently, due to limited SNR and transient aperture, resolution was lost. This problem of SNR can be omitted with a simultaneous illumination of the confinement

and measurement PSFs. Since in this case, the aperture is stable because the AML is in a photostationary state, the signal can be collected for a longer time i.e., the integration time of the detector can be increased until the desired SNR is achieved without broadening the aperture itself.

To increase the resolution enhancement achieved by AMI in reflection microscopy the photochromic properties of the AML must be improved. For an ideal AML, it should exhibit high fatigue resistance, such that the number of switching cycles is increased at least by an order of magnitude for 1D AMI and two orders of magnitude for AMI in 2D, without any visible degradation of the layer. This would enable us to implement a simultaneous illumination sequence to achieve higher resolution with better SNR. Furthermore, a higher concentration of the BTE-1 molecules in the layer is required to achieve better absorbance without increasing the thickness of the AML. For thick AML, diffraction produces high losses which results in low SNR. Furthermore, for an objective lens with high NA for e.g., NA = 0.9, the layer thickness of 1200 nm would be larger than the axial width of the PSF, especially for the confinement wavelength of 325 nm, which is not desirable for aperture generation. According to Kowarsch *et al.*, an ideal case would be to have an AML of thickness 100 nm with at least six times higher concentration (if the absorption cross sections are the same) of the BTE-1 molecules than the current concentration to achieve 5-fold resolution enhancement.

To make AMI more compatible and easy to incorporate with existing microscopes, a longer confinement wavelength would be more favourable as for wavelengths in the UV range, special optics are needed. In our microscope, we found a way to incorporate both the wavelengths, from UV and VIS spectrum, by using a SO. While it provides a way to eliminate chromatic aberrations, it also introduces significant sidelobes (see Fig. 5.14). Due to the coherent nature of the reflection microscope, these sidelobes complicate the imaging of extended objects. In our microscope, other than the limitation of the AML, the acquisition time is restricted to a minimum of 7 ms, due to a mechanical shutter placed in the UV beam path to block any residual light at the confinement wavelength on the sample plane. However, by replacing the mechanical shutter with another AOM, this limitation can be easily overcome.

The work presented in this thesis can be interpreted as a first proof of AMI in reflection microscopy that can achieve super-resolution and can be used for investigations on surfaces of composite materials with a resolution of a few tens of nanometers in the future. Further research is required to develop an AML with improved properties, in order to achieve better experimental conditions and higher resolution enhancement. The behaviour of the AML at high intensities of the confinement and measurement beams should also be investigated, which will help in the development of an efficient illumination sequence and fast image acquisition.

References

[1] E. Abbe, "Beiträge zur Theorie des Mikroskops und der mikroskopischen Wahrnehmung," *Archiv f. mikrosk. Anatomie*, vol. 9, pp. 413–468, 1873.

[2] S. W. Hell and J. Wichmann, "Breaking the diffraction resolution limit by stimulated emission: Stimulated-emission-depletion fluorescence microscopy.," eng, *Opt. Lett.*, vol. 19, no. 11, pp. 780–782, 1994.

[3] R. Menon and H. I. Smith, "Absorbance-modulation optical lithography," *Journal of the Optical Society of America A, Optics and Image Science*, vol. 23, no. 9, pp. 2290–2294, Sep. 2006.

[4] R. Menon and H. I. Smith, "Nanoscale imaging via absorption modulation," US 8143601 B2, 2009.

[5] R. Kowarsch, C. Geisler, A. Egner, and C. Rembe, "Superresolution reflection microscopy via absorbance modulation: A theoretical study," *Opt. Express*, vol. 26, no. 5, pp. 5327–5341, Feb. 2018.

[6] P. A. Heimann and R. Urstadt, "Deep ultraviolet microscope," *Appl. Opt.*, vol. 29, no. 4, pp. 495–501, Feb. 1990.

[7] E. H. Synge, "A suggested method for extending microscopic resolution into the ultra-microscopic region," *Lond. Edinb. Dublin philos. mag. and J. Sci.*, vol. 6, no. 35, pp. 356–362, Aug. 1928.

[8] A. Lereu, A. Passian, and P. Dumas, "Near field optical microscopy: A brief review," *Int. J Nanotechnol.*, vol. 9, pp. 3–7, Feb. 2012.

[9] T. A. Klar and S. W. Hell, "Subdiffraction resolution in far-field fluorescence microscopy," *Opt. Lett.*, vol. 24, no. 14, pp. 954–956, 1999.

[10] R. Menon, H.-Y. Tsai, and S. W. Thomas, "Far-Field Generation of Localized Light Fields using Absorbance Modulation," *Phys. Rev. Lett.*, vol. 98, no. 4, Jan. 2007.

[11] T. L. Andrew, H.-Y. Tsai, and R. Menon, "Confining Light to Deep Subwavelength Dimensions to Enable Optical Nanopatterning," *Science*, vol. 324, no. 5929, pp. 917–921, Apr. 2009.

[12] H.-Y. Tsai, S. W. Thomas, and R. Menon, "Parallel scanning-optical nanoscopy with optically confined probes," *Opt. Express*, vol. 18, no. 15, pp. 16 014–16 024, Jul. 2010.

[13] M. Minsky, "Microscopy apparatus," US3013467 A, 1961.

[14] R. H. Webb, "Confocal optical microscopy," *Rep. Progr. Phys.*, vol. 59, no. 3, pp. 427–471, Mar. 1996.

[15] S. W. Hell, M. Schrader, K. Bahlmann, F. Meinecke, J. R. Lakowicz, and I. Gryczynski, "Stimulated emission on microscopic scale: Light quenching of Pyridine 2 using a Ti:sapphire laser," *J. Microsc.*, vol. 180, no. 2, RP1–RP2, Nov. 1995.

[16] R. R. E. E. Wilson and M. W. Davidson. "Basic Microscopy." (2022.07.07), [Online]. Available: `www.zeiss.com/microscopy/int/solutions/reference/basic-microscopy`.

[17] B. E. A. Saleh and M. C. Teich, *Fundamentals of Photonics*. John Wiley & Sons, Inc., Aug. 1991.

[18] J. W. Goodman, *Introduction to Fourier Optics*, 2nd. MaGraw-Hill, 1996.

[19] T. Wilson and C. Sheppard, *Theory And Practice Of Scanning Optical Microscopy*. Academic Press, London, 1984, Oct. 1984, vol. -1.

[20] G. B. Airy, "On the Diffraction of an Object-glass with Circular Aperture," *Trans. Cambridge Philos. Soc.*, vol. 5, pp. 283–91, 1835.

[21] F. Zernike, "How I Discovered Phase Contrast," *Science*, vol. 121, no. 3141, pp. 345–349, Mar. 1955.

[22] C. Sheppard, "The use of lenses with annular aperture in scanning optical microscopy," *Opt. - Int. J. Light Electron Opt.*, Mar. 1977.

[23] Y. Horikawa, "Resolution of annular-pupil optical systems," *J. Opt. Soc. Am. A*, vol. 11, no. 7, pp. 1985–1992, Jul. 1994.

[24] J. Liu, "Elliptical Mirrors: Applications in microscopy," in IOP Publishing, 2018.

[25] G. Lan and M. D. Twa, "Theory and design of Schwarzschild scan objective for Optical Coherence Tomography," *Opt. Express*, vol. 27, no. 4, p. 5048, Feb. 2019.

[26] C. J. R. Sheppard and A. Choudhury, "Annular pupils, radial polarization, and superresolution," *Appl. Opt.*, vol. 43, no. 22, pp. 4322–4327, Aug. 2004.

[27] M. Born and E. Wolf, *Principles of Optics*, 7th. Cambridge University Press, 1999.

[28] S. Perrin and P. Montgomery, “Fourier optics: basic concepts,” Working paper or preprint, Dec. 2019.

[29] C. J. R. Sheppard and A. Choudhury, “Image Formation in the Scanning Microscope,” *Opt. Acta (Lond.)*, vol. 24, no. 10, pp. 1051–1073, Oct. 1977.

[30] S. V. Aert, D. V. Dyck, and A. J. den Dekker, “Resolution of coherent and incoherent imaging systems reconsidered - Classical criteria and a statistical alternative,” *Opt. Express*, vol. 14, no. 9, pp. 3830–3839, May 2006.

[31] J. Demmerle, E. Wegel, L. Schermelleh, and I. M. Dobbie, “Assessing resolution in super-resolution imaging,” *Methods*, vol. 88, pp. 3–10, 2015, Super-resolution Light Microscopy.

[32] S. Lord Rayleigh Sec. R., “On the theory of optical images, with special reference to the microscope,” *Philos. Mag. Series 5*, vol. 42, no. 255, pp. 167–195, 1896.

[33] V. Sacek. “Notes on AMATEUR TELESCOPE OPTICS.” (2006), [Online]. Available: `www.telescope-optics.net/index.htm`.

[34] G. S. Kino and T. R. Corle, *Confocal Scanning Optical Microscopy and Related Imaging Systems*. Elsevier, 1996.

[35] P. S. Considine, “Effects of Coherence on Imaging Systems∗,” *J. Opt. Soc. Am.*, vol. 56, no. 8, pp. 1001–1009, Aug. 1966.

[36] R. W. Cole, T. Jinadasa, and C. M. Brown, “Measuring and interpreting point spread functions to determine confocal microscope resolution and ensure quality control,” *Nat. Protocols*, vol. 6, no. 12, pp. 1929–1941, Nov. 2011.

[37] J. Vangindertael, R. Camacho, W. Sempels, H. Mizuno, P. Dedecker, and K. P. F. Janssen, “An introduction to optical super-resolution microscopy for the adventurous biologist,” *Methods Appl. Fluoresc.*, vol. 6, no. 2, Mar. 2018.

[38] W. Lukosz, “Optical Systems with Resolving Powers Exceeding the Classical Limit∗,” *J. Opt. Soc. Am.*, vol. 56, no. 11, pp. 1463–1471, Nov. 1966.

[39] C. W. McCutchen, “Superresolution in Microscopy and the Abbe Resolution Limit,” *J. Opt. Soc. Am.*, vol. 57, no. 10, pp. 1190–1192, Oct. 1967.

[40] A. S. H. E.A. and G. NICHOLLS, “Super-resolution Aperture Scanning Microscope,” *Nature*, vol. 237, no. 5357, pp. 510–512, Jun. 1972.

[41] C. Sheppard and C. Cogswell, “Reflection and transmission confocal microscopy,” in Elsevier, Jan. 1993, pp. 310–315.

[42] A. D. Elliott, “Confocal Microscopy: Principles and Modern Practices,” *Curr. Protoc. Cytom.*, vol. 92, no. 1, Dec. 2019.

[43] C. J. R. Sheppard, "Super-resolution in confocal imaging," *Optik*, vol. 80, no. 2, pp. 53–54, 1988.

[44] S. W. Hell, "Nobel Lecture: Nanoscopy with freely propagating light," *Rev Mod Phys*, vol. 87, no. 4, pp. 1169–1181, Oct. 2015.

[45] J. Keller, A. Schönle, and S. W. Hell, "Efficient fluorescence inhibition patterns for RESOLFT microscopy," *Opt. Express*, vol. 15, pp. 3361–3371, 6 2007.

[46] M. A. Schwentker *et al.*, "Wide-field subdiffraction RESOLFT microscopy using fluorescent protein photoswitching," *Microsc. Res. Tech.*, vol. 70, no. 3, pp. 269–280, 2007.

[47] G. Vicidomini *et al.*, "STED Nanoscopy with Time-Gated Detection: Theoretical and Experimental Aspects," *PLoS One*, vol. 8, no. 1, G. Chirico, Ed., e54421, Jan. 2013.

[48] E. Betzig *et al.*, "Imaging Intracellular Fluorescent Proteins at Nanometer Resolution," *Science*, vol. 313, no. 5793, pp. 1642–1645, 2006.

[49] T. A. Klar, R. Wollhofen, and J. Jacak, "Sub-Abbe resolution: From STED microscopy to STED lithography," *Physica Scripta*, vol. 2014, no. T162, p. 014 049, 2014.

[50] J. Farahani, M. Schibler, and L. Bentolila, "Stimulated Emission Depletion STED Microscopy: From Theory to Practice," *Microscopy: Sci. Tech. Appl. and Edu.*, vol. 2, Jan. 2010.

[51] S. W. Hell, "Far-Field Optical Nanoscopy," *Science*, vol. 316, no. 5828, pp. 1153–1158, 2007.

[52] M. Reuss, "Simpler STED setups," Ph.D. dissertation, 2011.

[53] E. Rittweger, K. Y. Han, S. E. Irvine, C. Eggeling, and S. W. Hell, "STED microscopy reveals crystal colour centres with nanometric resolution," *Nature Photonics*, vol. 3, no. 3, pp. 144–147, Feb. 2009.

[54] G. Moneron and S. W. Hell, "Two-photon excitation STED microscopy," *Opt. Express*, vol. 17, no. 17, p. 14 567, 2009.

[55] J. K. Pape *et al.*, "Multicolor 3D MINFLUX nanoscopy of mitochondrial MICOS proteins," *Proc. Natl. Acad. Sci.*, vol. 117, no. 34, pp. 20 607–20 614, Aug. 2020.

[56] H. Dürr and H. Bouas-Laurent, *Photochromism: Molecules and Systems*. Elsevier Science, 2003.

[57] H. Jean-Ruel *et al.*, "Ring-Closing Reaction in Diarylethene Captured by Femtosecond Electron Crystallography," *J. Phys. Chem. B*, vol. 117, no. 49, pp. 15 894–15 902, Oct. 2013.

[58] S. Kobatake, S. Takami, H. Muto, T. Ishikawa, and M. Irie, "Rapid and reversible shape changes of molecular crystals on photoirradiation," *Nature*, vol. 446, no. 7137, pp. 778–781, Apr. 2007.

[59] S. Kawata and Y. Kawata, "Three-Dimensional Optical Data Storage Using Photochromic Materials," *Chem. Rev.*, vol. 100, no. 5, pp. 1777–1788, Apr. 2000.

[60] K. Nakatani, J. Piard, P. Yu, and R. Métivier, "Introduction: Organic Photochromic Molecules," in *Photochromic Materials: Preparation, Properties and Applications*, Wiley-VCH Verlag GmbH & Co. KGaA, Jun. 2016, pp. 1–45.

[61] G. Pariani, R. Castagna, R. Menon, C. Bertarelli, and A. Bianco, "Modeling absorbance-modulation optical lithography in photochromic films," *Opt. Lett.*, vol. 38, no. 16, p. 3024, Aug. 2013.

[62] J. E. Foulkes, "Absorbance Modulation Optical Lithography: Simulating the Performance of an Adaptable Absorbance Mask in the Near-Field.," en, Ph.D. dissertation, 2010.

[63] A. Majumder, "Super-Resolution Optical Nanopatterning Beyond the Far-Field Diffraction Limit Using Photochromic Molecules and Absorbance Modulation Optical Lithography," Ph.D. dissertation, University of Utah, Jan. 2018.

[64] H.-Y. S. Tsai, "Overcoming the far-field diffraction limit via absobance modulation," Ph.D. dissertation, 2011.

[65] D. R. Paschotta. "Acousto-optic Modulators in the RP Photonics Encyclopedia." (2022.08.09), [Online]. Available: `www.rp-photonics.com/acousto_optic_modulators.html`.

[66] "PGL Technical Note." (2022.07.07), [Online]. Available: `www.plymouthgrating.com/guidance/technical-notes`.

[67] F. Görlitz *et al.*, "easySLM-STED: Stimulated emission depletion microscopy with aberration correction, extended field of view and multiple beam scanning," *J Biophotonics*, vol. 11, no. 11, e201800087, Jul. 2018.

[68] F. Curdt *et al.*, "isoSTED nanoscopy with intrinsic beam alignment," *Opt. Express*, vol. 23, no. 24, p. 30 891, Nov. 2015.

[69] N. Bokor, Y. Iketaki, T. Watanabe, and M. Fujii, "Investigation of polarization effects for high-numerical-aperture first-order Laguerre-Gaussian beams by 2D scanning with a single fluorescent microbead," *Opt. Express*, vol. 13, no. 26, pp. 10 440–10 447, Dec. 2005.

[70] "BOS Reflecting Objective User Guide v2." (2015-01-22), [Online]. Available: `www.beckoptronic.com`.

[71] G. Pariani *et al.*, "New Insight into the Fatigue Resistance of Photochromic 1,2-Diarylethenes," *J. Phys. Chem. C*, vol. 121, no. 42, pp. 23 592–23 598, Oct. 2017.

[72] M. Herder, B. M. Schmidt, L. Grubert, M. PÃ¤tzel, J. Schwarz, and S. Hecht, "Improving the Fatigue Resistance of Diarylethene Switches," *J. Am. Chem. Soc.*, vol. 137, no. 7, pp. 2738–2747, Feb. 2015.

[73] U. Wiedemann, W. Alt, and D. Meschede, "Switching photochromic molecules adsorbed on optical microfibres," *Opt. Express*, vol. 20, no. 12, p. 12 710, May 2012.

[74] G. Pariani, A. Bianco, R. Castagna, and C. Bertarelli, "Kinetics of Photochromic Conversion at the Solid State: Quantum Yield of Dithienylethene-Based Films," *J. Phys. Chem. A*, vol. 115, no. 44, pp. 12 184–12 193, Nov. 2011.

[75] H. Horvath, "Gustav Mie and the scattering and absorption of light by particles: Historic developments and basics," *J Quant. Spectrosc. Radiat. Transf.*, vol. 110, no. 11, pp. 787–799, Jul. 2009.

[76] T. Li, H. Feng, Z. Xu, X. Li, Z. Cen, and Q. Li, "Comparison of different analytical edge spread function models for MTF calculation using curve-fitting," in *SPIE Proceedings*, SPIE, Oct. 2009.

List of publications

Parts of this thesis have been published as follows:

- P. Jain, C. Geisler, A. Egner: "High-resolution reflection microscopy via absorbance modulation", submitted.

Talks on conferences:

- P. Jain, V. Udachin, S. Nagorny, C. Geisler, J. Adams, A.Schmidt, C. Rembe, A. Egner, "High-resolution reflection microscopy via absorbance modulation", Microscience Microscopy Congress 2021, virtual,(07.2021)

Acknowledgments

This endeavour would never have been possible without the guidance and generous support of several individuals. I would like to take this opportunity to thank all those who have made this journey possible.

First and foremost, I would like to express my sincere gratitude to my supervisor Prof. Dr. Alexander Egner for providing me with the opportunity to work on this project. I want to thank him for his patience, guidance, encouragement and dedicated involvement in every step of my PhD study. His guidance has helped me in all the time of research and writing of this thesis. His knowledge, enthusiasm and dedication to work have been inspirational.

I would also like to thank my thesis and examination committee members, Prof. Dr. Claus Ropers and Prof. Dr.-Ing. Christian Rembe, Prof. Dr. Jörg Enderlein, Prof. Dr. Michael Seibt and Prof. Dr. Sarah Köster, who have generously provided their time and expertise and helped me get through the final step of my thesis.

Words cannot express my gratitude to Dr. Claudia Geisler. I am extremely grateful for her exceptional mentoring, patience and feedback during my PhD thesis. From the first day of developing the setup to the last day until I submitted my thesis, she has consistently helped and guided me. In particular, I want to thank her for her time and dedication, especially during my thesis correction. Her guidance and support in every aspect have been invaluable.

I would also like to thank Sven Nagorny for synthesising the BTE-1 molecules, and Viktor Udachin and Thea Weingartz for preparing the AML-coated samples. I also want to thank them and Dennis Leitz for helpful discussions about the experiments related to photochromic molecules.

Special thanks go to all the current and former members of the Optical Nanoscopy group for creating a positive and friendly work environment. I especially want to thank:
Dr. René Siegmund, who has always been there for constructive discussions about work-related topics or otherwise. I especially want to thank him for helping me with the TiSa laser and proofreading my thesis. Through his, sometimes difficult-to-understand, puns and happy personality, he has always made the group meetings and work environment more fun.
Dr. Julia Kratz for her support and friendship during my PhD work as well as for

proofreading parts of my thesis.
Debadrita, for being there as a colleague and a friend and for helping me with the office work, especially during the home office period.

I would like to express many thanks to all other colleagues at the IFNANO and the administration, especially Mrs. Jutta Steckel and the purchasing department, Mr. Uwe Lampe, who have patiently helped me to get through all the bureaucratic requirements. Additionally, I would like to thank Mr. Andreas Spata for realising all the adapters and mounting constructions and the optical workshop at MPI, Faßberg for customising the substrates.

I want to express my profound gratitude to my parents for their unconditional love and support throughout my PhD journey. Without their efforts, encouragement and belief in me, I would have never been able to reach this far in my life. I would also like to thank my sisters for providing me with unfailing support and continuous encouragement. I want to thank all my friends for their constant support.

I owe a very special thanks to Pawan for his care and support throughout my PhD thesis. From the simulations to the endless late-night discussions and thesis correction, he has always been there and encouraged me, especially during the writing of my thesis.

Eidesstattliche Erklärung

Hiermit erkläre ich, dass ich die vorliegende Arbeit selbständig angefertigt, nicht anderweitig zu Prüfungszwecken vorgelegt und keine anderen als die angegebenen Hilfsmittel verwendet habe. Sämtliche wissentlich verwendeten Textausschnitte, Zitate oder Inhalte anderer Verfasser wurden ausdrücklich als solche gekennzeichnet.

_____ _____

Ort, Datum